Ministry of Higher Education and Scientific Research
Hassiba Benbouali University of Chlef
Faculty of Science and Technology
Department of Process Engineering

THESIS

Presented for the attainment of the degree of

DOCTORATE

Field of Study: Process Engineering

Specialty: Process Engineering

By

Hytef TOUATI

Theme:

Modelised elimination of a persistent organic molecule using the electro-photocatalysis technique: industrial application

Defended on **26/04/2025**, In front of a jury composed of:

Chahinez FARES	Professor	U.H.B- Chlef	President
Abdelaziz SAHMI	Lecturer/A	U.M.B-Boumerdes	Supervisor
Abdelkader KHADRAOUI	Professor	U.D.B- Khemis Miliana	Co-Supervisor
Abdellah LABBACI	Professor	U.H.B-Chlef	Examiner
Hicham LAHMAR	Professor	U.M.S.B.Y-Jijel	Examiner
Hammouche AKSAS	Professor	U. M.B-Boumerdes	Examiner
Mohamed TRARI	Professor	U.S.T.H.B-Algeries	Invited guest

Dedication

I DEDICATE THIS MODEST WORK:

To my very dear Mother and Father, in testimony and gratitude for Their devotion, their constant support throughout my years of study, Their unlimited sacrifice, Their moral comfort, They who have put so much effort into my education and training to see me achieve this goal, for all this and for what cannot be said, My boundless affections.

My very dear twin sister Chaza, who is far away from me but always present in my soul, my mind and my heart, May God heal her.

My dear sister Feriel Lina.

My dear brother Mohamed El Amine.

All those who are dear to me.

As a token of my affection

Acknowledgments

The work presented in this manuscript was carried out at the Valorisation des Substances Naturelles laboratory under the supervision of Professor ***K.HACHAMA*** *of the University Djilali Bounaama Khemis Miliana (U.D.B.K.M).*

This thesis was written under the supervision of Professor ***A. SAHMI*** *and under the co-direction of* ***A.KHADRAOUI,*** *I would like to express my deep gratitude to them for their guidance, for the encouragement they have always given me, but also for the autonomy they have granted me during my research work.*

I would like to thank ***Madame Ch.Fares*** *Professor at U.H.B.C. for agreeing to do us the honour of chairing the jury for this thesis, we are very grateful to him and offer him our warmest thanks.*

I would like to thank ***M.TRARI*** *Professor at U.S.T.H.B,* ***H.AKSAS*** *Professor at the University of Boumerdes,* ***H.LAHMAR*** *professor at the University of Jijel and to* ***A.LABBACI*** *Professor at the University of Chlef who have honoured me by agreeing to take part in this jury, may they find here the expression of my deepest gratitude.*

Finally, I would like to thank all the people I have met along the way for their sympathy, generosity, and good humour. They have all contributed in their own way, in one way or another, to the success of this thesis.

Résumé

La présence de colorants dans les rejets industriels constitue un danger pour l'environnement en raison de leurs effets néfastes sur la faune et la flore. Pour répondre à cette problématique, de nombreuses recherches se concentrent sur le procédé d'oxydation anodique, une technique faisant partie des Procédés d'Oxydation Avancée (POA). Ce procédé repose sur la formation d'entités chimiques très réactives, qui dégradent les molécules persistantes en composés biologiquement dégradables.

Pour évaluer l'efficacité de ce procédé, nous avons étudié l'effet de divers paramètres, notamment les nouveaux matériaux constituant les électrodes, l'intensité du courant, la distance inter-électrodes, la nature et la concentration des électrolytes, la concentration du polluant méthylorange, le pH du milieu, et l'oxygénation par barbotage. Après optimisation des conditions, nous avons appliqué un plan d'expérience « Box-Behnken » à trois facteurs, aboutissant à une modélisation représentative.

Pour tester l'efficacité du procédé, un rejet réel d'une industrie textile algérienne a été caractérisé et traité par cette méthode, ce qui a permis d'obtenir une élimination de 93% de la turbidité, 34,5% de la DBO_5, 61% des MES, et 44% de la DCO, toutes ces valeurs étant inférieures aux normes de rejet en vigueur.

La vérification de notre procédé par le test microbien a été une preuve supplémentaire de l'efficacité du procédé, puisque la croissance des trois types de bactéries utilisées (Escherichia coli, Pseudomonas et Staphylococcus aureus) n'a pas été inhibée après le traitement par électro-photocatalyse.

Le processus d'électro-photocatalyse peut donc être appliqué à l'échelle industrielle pour le traitement des polluants organiques persistants. Notre étude nous permet de déduire que 24 kwh est l'énergie nécessaire pour produire 1 m^3 d'eau ultra-pure à usage pharmaceutique ou électronique.

Mots-clés : Colorants, processus d'électrophotocatalyse, processus d'oxydation avancés, électrodes, orange de méthyle, rhodamine B, conception expérimentale, modélisation, normes, toxicité.

Abstract

The presence of dyes in industrial effluents poses a significant threat to the environment due to their harmful effects on flora and fauna. To address this issue, numerous studies focus on anodic oxidation, a technique that is part of Advanced Oxidation Processes (AOPs). This method relies on the formation of highly reactive chemical species, which break down persistent molecules into biologically degradable compounds.

To assess the efficiency of this process, we investigated the effect of various parameters, including new electrode materials, current intensity, inter-electrode distance, the nature and concentration of electrolytes, the concentration of the pollutant methyl orange, the pH of the medium, and oxygen bubbling. After optimizing the conditions, we applied a Box-Behnken design with three factors, resulting in a representative model.

To test the effectiveness of the process, a real effluent from an Algerian textile industry was characterized and treated using this method. This treatment achieved removals of 93% for turbidity, 34.5% for BOD_5, 61% for TSS, and 44% for COD, all of which meet discharge standards.

Verification of our process by the microbial test was further proof of the process's effectiveness, as the growth of the three types of bacteria used (Escherichia coli and Pseudomonas and Staphylococcus aureus) was not inhibited after treatment by electro-photo-catalysis.

The electro-photocatalysis process can therefore be applied on an industrial scale for the treatment of persistent organic pollutants. From our study we can deduce that 24 kwh is the energy required to produce 1 m^3 of ultra-pure water for pharmaceutical or electronic use

Keywords: Dyes, Electrophotocatalysis process, Advanced oxidation processes, Electrodes, Methyl orange, , Rhodamine B, Experimental design, Modeling, Standards, Toxicity.

ملخص

يشكل وجود الأصباغ في النفايات الصناعية خطرا على البيئة بسبب آثارها الضارة على النباتات والحيوانات. ولمعالجة هذه المشكلة، تركز الكثير من الأبحاث على عملية الأكسدة الأنودية، وهي تقنية تشكل جزءًا من عمليات الأكسدة المتقدمة . تعتمد هذه العملية على تكوين كيانات كيميائية شديدة التفاعل، والتي تعمل على تحلل الجزيئات الثابتة إلى مركبات قابلة للتحلل البيولوجي.

لتقييم فعالية هذه العملية، قمنا بدراسة تأثير العديد من المعلمات، بما في ذلك المواد الجديدة التي تشكل الأقطاب الكهربائية، وشدة التيار، والمسافة بين الأقطاب الكهربائية، وطبيعة وتركيز الإلكتروليتات، وتركيز ملوث البرتقالي الميثيلي، ودرجة حموضة الوسط والأكسدة عن طريق الفقاعات. بعد تحسين الظروف، قمنا بتطبيق تصميم تجريبي ثلاثي العوامل مما أدى إلى الحصول على نموذج تمثيلي "Box-Behnken"،

لاختبار فعالية العملية، تم توصيف ومعالجة تصريف حقيقي من صناعة النسيج الجزائرية باستخدام هذه الطريقة، مما أدى إلى إزالة93% من العكارة، و 34.5٪ من الطلب البيولوجي البيوكيميائي، و 61٪ من المواد الصلبة العالقة، و 44٪ من الطلب الكيميائي الكيميائي ، وكلها كانت أقل من معايير التصريف المعمول بها

وكان التحقق من صحة عمليتنا من خلال الاختبار الميكروبي دليلاً إضافياً على فعالية العملية، حيث لم يتم تثبيط نمو الأنواع الثلاثة من البكتيريا المستخدمة (الإشريكية القولونية، والزائفة الزنجارية، والمكورات العنقودية الذهبية) بعد العلاج بالتحفيز الضوئي الكهربائي.

وبناءً على ذلك، يمكن تطبيق عملية التحفيز الضوئي الكهربائي على نطاق صناعي لمعالجة الملوثات العضوية الثابتة. وتسمح لنا دراستنا باستنتاج أن 24 كيلووات ساعة هي الطاقة المطلوبة لإنتاج 1 متر مكعب من المياه النقية للغاية للاستخدام الصيدلاني أو الإلكتروني.

الكلمات المفتاحية: الأصباغ، عمليات التحفيز الضوئي الكهربائي، عمليات الأكسدة المتقدمة، الأقطاب الكهربائية، البرتقالي الميثيل، رودامين ب، التصميم التجريبي، النمذجة، المعايير، السمية.

Table of contents

Table of contents

List of figures

List of tables

Introduction

Protecting our environment means controlling the reduction of pollutants generated by human activitý particularly industrial activity. Today, in the face of global awareness, and more particularly within the framework of EU policy, discharges are closely controlled, subject to quotas and increasingly stringent regulations. As a result, industrial decision-makers are called upon to select appropriate analysis and pollution control techniques.

We often find substances that largely escape conventional wastewater treatment. Their presence in water and their accumulation in the aliphatic chain represent a serious threat to human and environmental health. This is the case of certain cyclic organic molecules < phenolics > stabilized by the +M/-M (donor/attractor) mesomer effect, which make up a large number of pharmaceutical substances, pesticides, dyes and other recalcitrant compounds.

Pollution of dye wastewater is receiving increasing attention due to increased production in the textile industry. Synthetic dyes play a crucial role in the industry, offering a wide range of bright, stable colors. Among these, xanthene dyes, such as rhodamine B, and azo dyes are particularly noteworthy.

Rhodamine B, a xanthene dye, is highly valued for its vibrant fluorescence and intense coloration. However, its application in textile dyeing poses significant environmental challenges, as improper disposal can lead to harmful contamination. Similarly, azo dyes, distinguished by their azo group (-N=N-), are extensively utilized in various industries due to their wide range of colors and chemical stability. Like Rhodamine B, these dyes are synthetically produced, and stringent control of their discharge into wastewater is crucial to reduce their environmental impact [1].

Azo colorants are among the most widely used synthetic dyes but remain difficult to eliminate effectively due to their high chemical stability and are considered major pollutants in textile wastewater. For example, methyl orange (MO) is one of the most widely used dyes in textile manufacturing in Algeria. This substance remains in the environment for very long periods, and its aromatic cyclic structure presents a great danger to aquatic and human life.

To prevent the accumulation of MO in the environment, various treatment methods for persistent organic pollutants have been developed. These include processes such as photocatalysis, sonochemistry, electro-Fenton and ozonolysis.

In recent years, advanced oxidation processes have received increasing attention for their effectiveness in treating wastewater contaminated with phenol and its by-products. These processes offer several significant advantages such as environmental sustainability, adaptability, energy efficiency, safety, selectivity, and the ability to be automated.

In this context, we took an interest in the electrophotocatalysis process, which is one of the most recent of them, and used new materials as electrodes to see their effects on the degradation of methylorange. The aim of this study was to gain a comprehensive understanding of the process's efficiency, performance characteristics, and its viability for industrial implementation.

To this effect, the present manuscript is presented in four chapters. The first chapter examines water pollution by the textile industry and its environmental impacts. It includes a general introduction on industrial discharges, followed by a literature review on dye pollution in water: their sources, toxicity, and available treatment methods. The chapter also discusses the different types of dyes used, as well as electro-photocatalysis techniques and the properties of synthesized semiconductors.

The second chapter provides an overview of semiconductor theory. The first part deals with material conductivity, semiconductor conduction mechanisms and their behavior under light. The second part deals with contact phenomena at the semiconductor/electrolyte interface.

The third chapter deals with the methods used to synthesize materials for electro-photocatalytic water purification, in particular the degradation of Methyl Orange and Rhodamine B. It also describes the various characterization techniques required for this study. The parameters influencing photo-activity have been optimized. In addition, an experimental set-up has been designed and a procedure developed to enable electro-photo-catalytic depollution.

The final chapter presents results and discussions on the physical and electrochemical characteristics of the synthesized materials. It also examines the application of these materials in photo-activity, detailing the results obtained and corresponding discussions.

The thesis concludes with an overview of the results obtained and their impact on the elimination of emerging pollutants from water.

Reference :

[1] : Saidi F. Z. and Mokhtari M., Central Composite Design To Optimize The Degradation Of Methylene Blue By Fenton Process, Chemistry Select. 4 (2019) 11288-11293.

Chapter I
Bibliographic study

I- Bibliographic study

I-A. Part I

I-A.1.The textile dye industry

The textile industry uses vast amounts of water and a wide variety of chemicals in the wet processing of textiles. These chemical reagents vary greatly in composition, encompassing everything from inorganic compounds to polymers and organic substances [1].

The dyestuffs industry is one of the most important areas of chemistry today. Dyes are used for printing and dyeing textile fibers, paper, leather, fur, wood, plastics, and elastomers. They are also used to prepare paints, printing inks and varnishes and, as additives, to colour food and pharmaceutical products. They are used in the cosmetics industry, metal colouring (anodised aluminium), photography (sensitisers), biology (colouring of microscopic preparations), colour indicators, and some of them are used in therapeutics (antiseptics, antimalarials, etc.) [2].

I-A.2.History of dyes

Dyes have been in use since ancient times, dating back to the era of the Pharaohs and even earlier. Initially, they were primarily used for wall paintings and various everyday objects. Up until the mid-19th century, dyes were predominantly derived from natural sources. These included plant-based dyes like alizarin and indigo, commonly used in textiles, as well as minerals such as manganese oxide, hematite, and ink, which were found on tiles, canvas, and kitchen utensils [3].

There are approximately 8,000 distinct synthetic dyes, registered in the Colour Index under 40,000 different trade names. These dyes are categorized by a code that specifies their class, shade, and order number, based on their application (shade, uses, fastness), chemical structure (such as azo, anthraquinone, triazine, methane, indigoid dyes), and brand names [4].

I-A.3.Classification of dryes

All aromatic compounds can absorb electromagnetic energy, but only those that absorb light within the visible spectrum (380 to 750 nm) exhibit color. Dyes are formed by chromophoric groups - conjugated aromatic groups containing nonbonding electrons (n-electrons) or transition metal complexes - together with auxochromes and conjugated aromatic structures such as benzene rings, anthracene, and perylene [5].

As the number of aromatic rings increases, the conjugation of double bonds also grows, leading to an expanded conjugated system. The most common chromophores and auxochromes are outlined in Table I-1 [6].

Table I-A-1. Main chromophore and auxochrome groups, arranged in order of increasing intensity [6].

Chromophore groups	Auxochrome groups
Azo (-N=N-)	**Amino($-NH_2$)**
Nitroso(-NO or –N-OH)	**Méthylamino($-NHCH_3$)**
Carbonyl(=C=O)	**Diméthyamino($-N(CH_{3)2}$)**
Vinyl(-C=C-)	**Hydroxyl(-OH)**
Nitro($-NO_2$ or =NO-OH)	**Alkoxyl(-OR)**
Sulfur(>C=S)	**Electron donor groups**

Dyes can be categorized based on their chemical composition, such as azo dyes, anthraquinone dyes, and indigo dyes, or according to their specific applications.

I-A.4. Physicochemical properties

The term "azo" refers to compounds featuring an azo (-N=N-) functional group that connects two identical or different alkyl or aryl groups, resulting in symmetrical or asymmetrical azo structures. Typically built on an azobenzene framework, these compounds are aromatic or pseudo-aromatic systems joined by the azo (-N=N-) chromophore.

The introduction of azo groups between two aromatic rings shifts the absorption spectrum of benzene towards longer wavelengths so that the color appears (bathochrome effect). The simplest azo, azobenzene, is yellow orange. The introduction of amine or phenol groups also has a bathochromic effect, as does the multiplication of azo groups (example of a diazo dye in Figure I.2), so it is possible to obtain almost any shade in the spectrum. The presence in such a structure of sulphonated, nitrated or halogenated substituents, electron donors on one of the aromatic rings and acceptors on the second rings, increases the resonance phenomenon. This is how we can influence color and dyeing qualities. In general, the more conjugated the p-system of the molecule, the greater the wavelength it will absorb. However, the complexity of the molecules reduces the vividness of the shades [7].

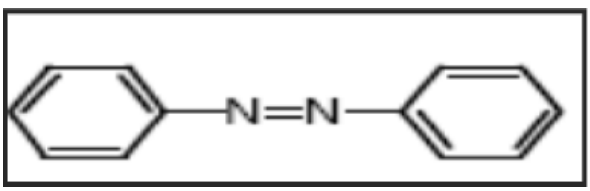

Figure I-A-1. Structure of azo dyes [8]

The substituents attached to the aromatic rings significantly influence hydroxyl radical attacks. The acetamide ($-NCOCH_3$) and hydroxyl (-OH) groups, through their inductive (-I) and mesomeric

(+M) effects, interact with the aromatic ring by delocalizing the π-electrons and the lone pairs of electrons on the heteroatoms. This delocalization enriches the phenyl ring with electrons, making it more susceptible to electrophilic attacks [7].

I-A.5. Toxicity of dyes

A study that cross-referenced LD50 values with chemical and dye classifications revealed that diazo and cationic dyes are among the most toxic synthetic organic dyes. The electron-withdrawing properties of azo groups create electron deficiencies, which render azo dyes resistant to oxidative degradation under aerobic environmental conditions [8].

The toxicity of azo dyes and their metabolites is well-documented, particularly concerning occupational exposure. A rise in bladder cancer cases among textile workers has been linked to prolonged exposure to these dyes. Subsequent research has confirmed the carcinogenic potential of azo dyes in both humans and animals. The azobenzene used in this study is recognized as a genotoxic compound, similar to amaranth, tartrazine, and cochineal red—some of the most hazardous azo dyes for human health, which have been removed from the list of approved food dyes in most countries.

The carcinogenic effects of azo compounds manifest indirectly through their amine derivatives. The azo bond, the most unstable part of these molecules, can be readily cleaved by enzymatic action (specifically by the azoreductase enzyme) in mammals, including humans, resulting in the formation of carcinogenic amine compounds. The toxicity of azo compounds is further heightened by the presence of substituents on the aromatic ring, especially nitro (-NO_2) and halogen (notably chlorine) groups.

I-A.6.Environmental impact

Many dyes remain visible in water even at concentrations below 1 mg/L, contributing significantly to pollution when large volumes of wastewater containing residual dyes are generated. The release of this wastewater into the environment poses serious threats, including pollution, eutrophication, and disruption of aquatic ecosystems. Additionally, it raises the risk of bioaccumulation, which can ultimately impact human health as these contaminants travel through the food chain.

I-A.6.1. Obvious dangers

• **Eutrophication:** occurs when dyes release nitrates into the environment through microbial activity. When introduced in large amounts, these mineral ions can become toxic to aquatic life and compromise drinking water quality. The excessive uptake of nitrates by aquatic plants promotes uncontrolled growth, which depletes oxygen levels by inhibiting photosynthesis in the deeper layers of rivers and stagnant waters. This process can severely disrupt aquatic ecosystems and harm fish populations. [9].

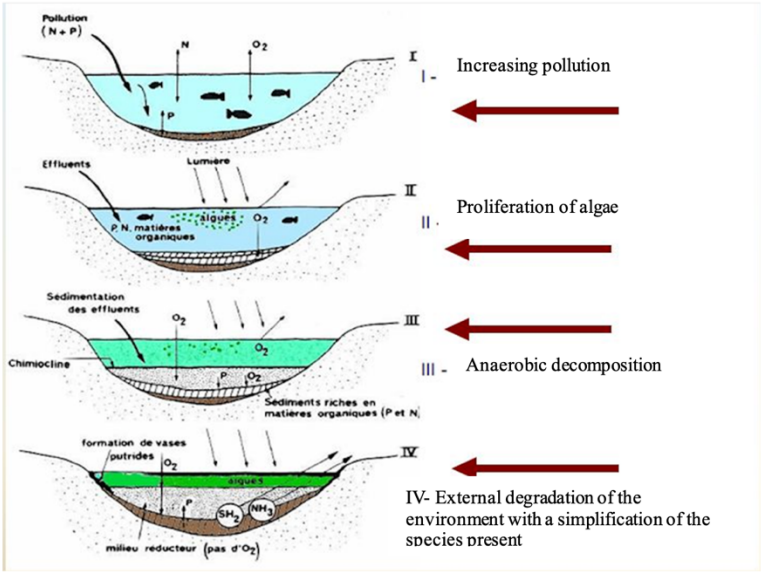

Figure I-A-2. Diagram of the main phases of the eutrophication [9]

• **Under-oxygenation:** occurs when excessive amounts of organic matter are released into the environment, overwhelming the natural processes that regulate oxygen levels. According to Manahan [10], the breakdown of just 7 to 8 mg of organic matter by microorganisms can deplete the oxygen in one liter of water. This oxygen depletion disrupts aquatic ecosystems, threatening the survival of aquatic life.

• **Color, turbidity, odor:** issues arise from the accumulation of organic matter in water bodies, leading to unpleasant tastes, bacterial growth, foul odors, and abnormal discoloration. Willmott et al. [11] estimated that the human eye can detect discoloration at concentrations as low as 5 µg/L. Beyond the unattractive appearance, these coloring agents can obstruct light transmission in water, hindering photosynthesis in aquatic plants.

I-A.7. Long-term dangers

- **Persistence:** Synthetic organic dyes are resistant to natural biological degradation, making them difficult to remove through conventional purification methods [12]. Their persistence is closely linked to their chemical properties:
  - Unsaturated compounds are generally less persistent than saturated ones.
  - Alkanes are less persistent compared to aromatic compounds.
  - The persistence of aromatic compounds increases with the number of substituents.
  - Halogen substituents enhance dye persistence more than alkyl groups.

• **Bioaccumulation**: When an organism lacks mechanisms to either prevent the absorption or eliminate a substance once it has been ingested, the substance tends to accumulate in its tissues. Species higher up the food chain, including humans, can be exposed to concentrations of toxic substances that are up to one hundred thousand times greater than the original levels in the water. This phenomenon of dye bioaccumulation is illustrated in Figure I-3.

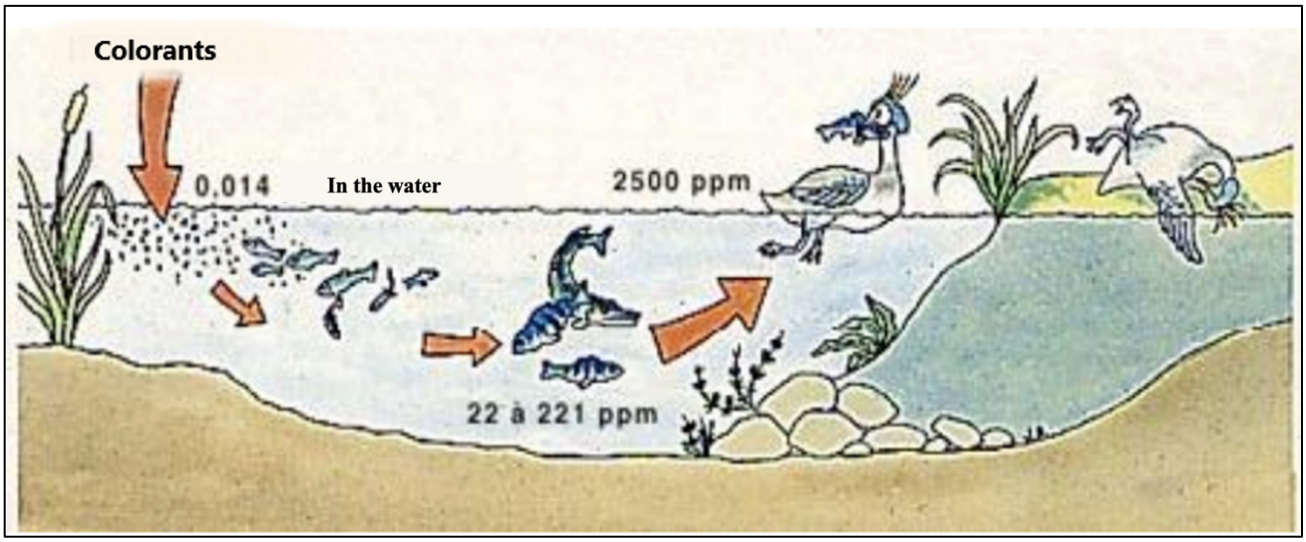

Figure I-A-3. Consequences of bioaccumulation following the discharge of toxic substances (dyes) into a watercourse **[13].**

- **Cancer:** Although most dyes are not directly toxic, a significant proportion of their metabolites are [14]. Their mutagenic, teratogenic or carcinogenic effects appear after the initial molecule has been broken down into oxidation by-products: carcinogenic amines for azo dyes, and leuco derivatives for triphenylmethanes [15]. According to the EPA (1998), to assess the risk of cancer, a concentration limit of 3.1 mg. l^{-1} of azo dye should be set for drinking water.

- **Chlorination by-products:** The chlorine used to eliminate pathogenic micro-organisms reacts with organic matter to form trihalomethanes (THMs) [16], which can reach several hundred mg/L. They are responsible for the development of liver, lung, kidney, and skin cancer in humans.

I-A.8. The polluants used

I-A.8.1. Methyl Orange

Methyl orange's clear and noticeable color change makes it a popular pH indicator for use in titrations. Its usage in acid titrations is often due to its color shift at the pH of a mid-range acid. Methyl orange has a sharper end point than a universal indicator, but it does not change color fully. Methyl orange turns from red to orange and then yellow in a decreasingly acidic solution; the converse happens in an increasingly acidic solution. The complete hue change occurs in an acidic atmosphere. In an alkaline solution, it is yellow, while in an acidic solution, scarlet. Methyl orange (MO), one of the well-known acid/amino dyes, is widely used in labs and the paper, printing, textile, and pharmaceutical sectors. An anionic dye that is a member of the azo dye family is methyl orange. There is nitrogen in the azo dye group of the molecule. Environmental scientists are concerned about MO because of its limited biodegradability and the presence of an azo group (N = N) on it [**17]**.

Figure I-A-4. Methyl Orange

Table I-A-2. Physico-chemical properties of methyl orange [17].

Nomenclature	Methyl Orange
Formule chimique	$C_{14}H_{14}N_3NaO_3S$
Structure	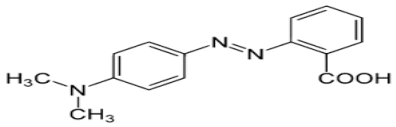
Molecular weight	327,34 g/mol
pKa	3,4
Solubility	5,2g.L^{-1} in water at 20 °C 1g. L^{-1} in ethanol at 20°C
Colour	Orange-red to pH<3,2 and Yellow to pH>4,4
Purity	95%
λ_{max}	465 nm
IUPAC name	Sodium4-[(4-dimethylamino) phenyldiazenyl] benzenesulphonate.

I-A.8.2. Rhodamine B

Rhodamine B is part of the xanthene dye family and is a cationic dye with high solubility in water, methanol, and ethanol. In a 30% acetic acid aqueous solution, its solubility reaches approximately 400 g/L. Glassware is recommended for handling, as Rh-B tends to adsorb onto plastic surfaces. The physicochemical characteristics of Rh-B are detailed in Table I.3.

Table I-A-3. Physoco-chemical properties of rhodamine B

structure	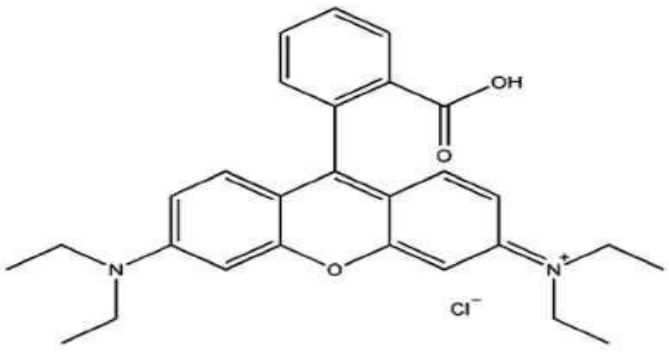
Nomenclature	Chlorure de [9-(2-carboxyphenyl)-6-diethylamino-3-xanthenylidene]-diethylammonium
Gross formula	**$C_{28}H_{31}ClN_2O_3$**

Molar mass	479,01 ± 0,028 g/mol
T Melting	210-211°C decompositions
Solubility	50 g.L $^{-1}$ à 20 °C in water
Mass density	0,79 g.cm^{-3}

Rhodamine B is harmful when ingested by humans and animals, causing irritation to the skin, eyes, and respiratory system. Due to its health risks, some countries have banned its use. In the United States, it is classified as an illegal dye because of its dangerous properties. Rhodamine B also tends to bioaccumulate, meaning that organisms lacking mechanisms to block its absorption or expel it may build up the substance in their bodies. This leads to species at the top of the food chain, including humans, being exposed to toxic concentrations up to 100,000 times higher than the original levels in the water [18].

I-B. Part II : Liquid waste treatment processes

The amount of dyes released into the environment varies depending on how strongly they adhere to cellulose fibers.

Azo dyes, which constitute the largest category of dyes in the Color Index (60-70%) and include acid, reactive, and direct dyes, are among the most significant pollutants found in textile wastewater. Various technologies for removing these organic pollutants are well-established both in laboratory settings and on an industrial scale. These methods include physical treatments such as adsorption, membrane technologies, and solid-liquid separation processes (e.g., precipitation, electrocoagulation), as well as chemical treatments like ion exchange, oxidation with oxygen, ozone, and oxidants (e.g., NaOCl, H_2O_2), and reduction (e.g., $Na_2S_2O_4$). The following sections provide an overview of these techniques for treating wastewater contaminated with major dyes [19].

I-B.1. Water treatment techniques

I-B.1.1. Physical methods

I-B.1.1.1. Adsorption (on activated carbon)

Activated carbon and similar adsorbent materials are commonly employed to remove a variety of dyes from wastewater. Despite their effectiveness, these adsorbents are not universally effective, as some dyes are non-ionic and may not be captured by all types of adsorbents. Activated carbon, renowned for its high adsorption capacity, is particularly effective at adsorbing many dyes [20-21]. However, this method merely transfers the pollutants from the liquid phase to the solid phase, without destroying them. Additionally, the regeneration of activated carbon and the handling of the resulting solid waste involve significant costs and additional post-treatment processes [22].

I-B.1.1.2. Membranes techniques

Membrane filtration controlled by hydraulic pressure can be divided into microfiltration, ultrafiltration, nano-filtration, and reverse osmosis. There are four types of processes: **nano-filtration** and reverse osmosis are best suited to the partial reduction of color and small organic molecules [23]. However, reverse osmosis is still the most widely used [24].

Nano-filtration is primarily used for treating reactive dye baths, functioning as a molecular filter to separate specific contaminants. Microfiltration, on the other hand, targets colloidal materials, including dispersed or vat dyes, using a "screen membrane" to filter out these particles [25]. Ultrafiltration is generally employed to reduce Chemical Oxygen Demand (COD) and suspended solids [26], but it is most effective when combined with coagulation and flocculation processes.

I-B.1.2. Chemical oxidation methods

I-B.1.2.1. Electrocoagulation and chemical coagulation

Chemical coagulation and electrocoagulation are often compared to determine the most suitable method for a given application. Both processes aim to aggregate colloidal particles by reducing their static surface charge or enhancing inter-particle bonding, which leads to particle bridging. Chemical coagulation involves adding chemical agents to achieve this aggregation. In contrast, electrocoagulation relies on the in-situ generation of metal cations through the dissolution of electrodes under an electric current. Although both methods ultimately aggregate particles, their mechanisms of action are distinct.

Chemical coagulation-flocculation therefore involves adding trivalent metal salts or other chemical substances to aqueous dispersions to assemble the particles dispersed in the effluent into larger aggregates. These aggregates can then be removed by settling, filtration or sedimentation. A wide range of coagulants are used:

- Mineral coagulants such as $Al_2(SO_4)_3$, $AlCl_3$, $FeSO_4$, $CaCO_3$, MgO.
- Organic coagulants such as polyacrylamides, which form polymers that drag all the suspended particles into the water to form flocs [27].

Chemical oxidation techniques are typically used when biological processes are insufficient for treating wastewater. These techniques can serve as a pre-treatment step to make subsequent biological treatment more effective. Chemical oxidation is particularly useful for addressing wastewater with high concentrations of non-biodegradable or toxic pollutants that other methods cannot adequately treat or convert into biodegradable and non-toxic forms. As a result, chemical oxidation is a valuable and effective approach in wastewater treatment.

A distinction is made between:

- conventional chemical oxidation processes.
- advanced oxidation processes.

Traditional chemical oxidation processes involve introducing an oxidizing agent into the treated solution. The primary oxidizing agents used in these processes include :

- **Chlorine Cl_2**: This moderately strong oxidizing agent is employed in wastewater treatment and disinfection, similar to ozone. However, chlorine can produce halogenated by-products that are potentially carcinogenic to humans.
- **Oxygen O_2:** Oxygen is often selected as a moderate oxidizing agent due to its relatively low cost. Its use is prevalent in various oxidation processes, despite its less aggressive oxidation capability compared to stronger agents.
- **Hydrogen Peroxide H_2O_2:** This is regarded as one of the most versatile and recommended oxidants for various processes, usable with or without a catalyst. However, its effectiveness is often limited when used alone for treating many organic compounds.
- **Ozone O_3**: This is a very strong oxidizing agent with advantages similar to those of oxygen and hydrogen peroxide. However, ozone's instability presents a significant challenge, necessitating on-site generation for its use. It has been noted that while ozone can be effective, chemical oxidation with this agent alone may not always sufficiently address persistent organic pollutants. In such cases, advanced oxidation processes are employed to achieve more thorough treatment.

- **Hydroxil radicals •OH:** are extremely reactive and non-selective, rapidly interacting with a wide range of organic compounds, which is advantageous for treating heterogeneous wastewater. Due to their high reactivity, they have a short lifespan and low instantaneous concentration. They are especially effective against alkenes and aromatic compounds and can oxidize or mineralize stubborn organic contaminants in minutes to hours. Continuous production of hydroxyl radicals is achieved using various methods, as illustrated in Figure I.B.1.

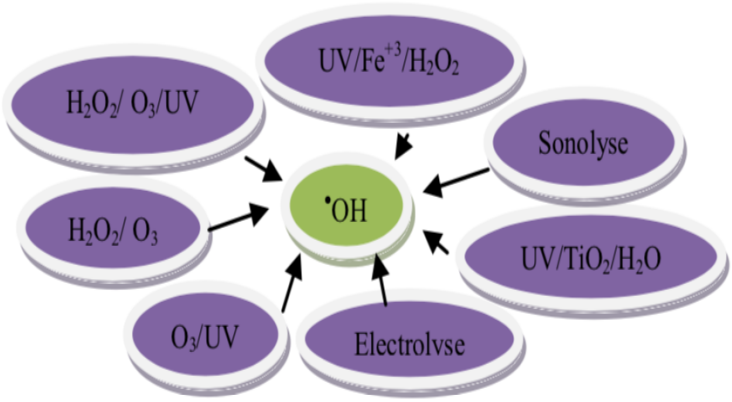

Figure I-B-1. Main processes for producing hydroxyl radicals. **[28].**

I-B.1.3. Advanced Oxidation Processes (AOPs)

AOPs can be categorized based on their phase—homogeneous or heterogeneous—or by the method employed to generate hydroxyl radicals. These methods include chemical, photochemical, electrochemical, and sonochemical techniques [29].

The effectiveness of Advanced Oxidation Processes (AOPs) is influenced by several factors including oxidant concentration, UV light intensity, pH and temperature. In addition, the composition of the medium plays a critical role; the presence of organic and inorganic substances can reduce oxidation efficiency by consuming hydroxyl radicals. For example, carbonates and bicarbonates react with hydroxyl radicals with rate constants of 1.5×10^7 L/mol.s and 4.2×10^8 L/mol.s, respectively, which can reduce the overall efficiency of the process [30].

While many reactions and variables influencing Advanced Oxidation Processes (AOPs) share similarities, understanding the fundamental differences between these processes is crucial, as they impact treatment efficiency and cost. Therefore, this chapter will explore both homogeneous and heterogeneous photochemical and electrochemical AOPs, specifically emphasizing the electro-Fenton process.

I-B.1.4. Hetergenous photocatalysis (semiconductor)

Heterogeneous photocatalysis relies on the excitation of a semiconductor catalyst. Semiconductors have a distinct electronic structure with a filled valence band and an empty conduction band. When exposed to UV radiation with photon energy equal to or exceeding the energy gap between these bands, electrons are excited from the valence band to the conduction band (denoted as e^-_CB). This transition creates an electron-hole pair, with the remaining hole in the valence band (denoted as h^+_VB) [30].

I-B.1.5. Sonolysis

Sonolysis is a technique that uses ultrasound to degrade pollutants in aqueous media. Sonolysis is increasingly used in industrial environments to accelerate reaction mechanisms. The advantage of ultrasound is that it is non-polluting and easy to automate. In aqueous media, ultrasound can act in two ways [31].

- Physical action (direct), with micro-mixing of the solution and improved matter transfer.
- Chemical action (indirect), with the appearance of high temperature and pressure when the bubbles are compressed, and the consequent generation of oxidizing radical species -OH and HO2-
- $H_2O + \text{Ultrasons} \rightarrow {}^{\bullet}OH + H^{\bullet}$ **(I.1)**

I-B.1.6. Electrochemical Processes

Electrochemical advanced oxidation processes make it possible to eliminate or reduce the quantities of chemical reagents by producing the oxidants directly in the medium using electrochemistry. There are two categories of electrochemical processes for producing hydroxyl radicals, either directly (anodic oxidation) or indirectly via the Fenton reagent. In the second case, the Fenton reaction is coupled to electrochemistry [32].

I-B.1.6.1. Direct electrochemistry (Anodic oxidation – Cathodic reduction)

The most widely used traditional electrochemical method for degrading organic pollutants is anodic oxidation. This technique involves generating adsorbed hydroxyl radicals (•OH) on the surface of a high oxygen overvoltage anode through the oxidation of water.

$$H_2O \rightarrow {}^{\bullet}OH_{ads} + H^+ + e^- \quad \textbf{(I.2)}$$

The oxidation of various organic compounds in aqueous solutions is facilitated by hydroxyl radicals generated at the anode. Selecting the appropriate electrode material is crucial for effective pollution control. Over the past fifteen years, extensive research has focused on optimizing wastewater treatment for organic pollutants. The most effective electrode materials are those with high oxygen evolution overpotentials, such as metal oxides like tin dioxide [33,34], lead dioxide [34], doped lead dioxide [34], and platinum (Pt) [35].

The Ti/Pt electrode proves to be an excellent material for generating hydroxyl radicals. Its use facilitates the production of potent oxidants, making it highly effective for the complete mineralization of various organic compounds.

The Ti/Pt electrode proves to be an excellent material for generating hydroxyl radicals. Its use facilitates the production of potent oxidants, making it highly effective for the complete mineralization of various organic compounds.

The continuous generation of H_2O_2 in an aqueous medium is achieved through the two-electron reduction of molecular oxygen at a suitable cathode. Selecting a cathode with a high hydrogen evolution overvoltage is essential for optimal performance [30]. Brillas et al. [36] demonstrated that oxygen diffusion electrodes can also be employed to reduce O_2 to H_2O_2 in acidic environments.

I-B.1.6.2. Electrophotocatalysis

Photoelectrocatalysis is a promising method for the photocatalytic degradation of organic pollutants. It is based on the application of an anodic potential to the working electrode, resulting in the photogeneration of electron-hole pairs (eh +) in various directions. This approach reduces the rate of recombination of the electron-hole pairs and thus accelerates the oxidation of organic compounds.

Photoelectrocatalysis is mainly influenced by the potential applied, the pH and the initial concentration of the pollutant. To obtain good photoelectrocatalytic activity, it is essential to work under the following conditions: apply as high a potential as possible, as this reduces the recombination of electron-hole pairs (e-/h+), maintain an acidic or basic pH so that the TiO_2 has a surface charge, and minimize the concentration of the pollutant [37].

References chap I:

[1] A. Aouni, C. Fersi, B. Cuartas-Uribe, A. Bes-Pia, M. I. Alcaina-Miranda, M. Dhahbi, Reactive dyes rejection and textile effluent treatment study using ultrafiltration and nanofiltration processes, Desalination, 297, (2012), 87-96.

[2] H. B. Mansour, O. Boughzala, D. Dridi, D. Barillier, L. Chekir-Ghedira , R .Mosrati, Textile dyes as sources of water contamination: CRIBLAGE of toxicity and treatment methods, Journal of water sciences / Journal of Water Science, 24(3), (2011), 209–238,

[3] W. Ouari, (Oxidation of dyes by POAs on catalysts based on modified commercial clay K10). Doctorate in Science, University of Tlemcen, (2017).

[4] Cattoor, T., 1 - European legislation relating to textile dyeing A2 - Christie, R.M. In Environmental Aspects of Textile Dyeing, Woodhead Publishing: (2007); pp 1-29.

[5] L. Zhenwang, C. Zhenlu, L. Jianyan, The PT dye molecular structure and its chromophoric luminescences mechanism. 15th World Conference on Non- Destructive Testing, 15-21 October 2000, Rome.

[6] E. Guivarch, Treatment of organic pollutants in aqueous media using the 'Electro-Fenton' advanced electrochemical oxidation process, Application to the mineralisation of synthetic dyes, Doctoral thesis from the University of Marne-la-Vallee., 2004.

[7] N. BOUANIMBA, Modelling and optimisation of the kinetics of photocatalytic degradation of organic pollutants in aqueous solution, Magister in Chemistry, Mentouri-Constantine University, (2009).

[8] Pagga U., Brown D. The degradation of dyestuffs part II: behaviour of dyestuffs in aerobic biodegradation tests. Chemosphere, (1986), 15, 4, 479-491.

[9] Zollinger H., Color chemistry, Synthese, properties and applications of organic dyes and pigments. VCH, (1987).

[10] L. NAIDJA, ELIMINATION OF ORANGE II COLOURANT IN AQUEOUS SOLUTION, BY PHOTOCHIMIC WAY AND BY ADSORPTION, Master's thesis in chemistry, University of Constanta, (2010)

[11] S.E. MANAHAN Environmental chemistry, 6e Ed, U.S.A. : Lewis publisher, 1994.

[12] NJ. WILLMOTT, JT. GUTHRIE, G.NELSON «The biotechnology approach to colour removal from textile effluent» JSDC, 1998, 114, 38-41

[13] U. PAGGA, D. BROWN « The degradation of dyestuffs part II: behaviour of dyestuffs in aerobic biodegradation tests » Chemosphere, 15, 4,1986, 479-491

[14] Servais P. Organic matter in natural environments. Press of the Ecole Nationale des Ponts et Chausses, October 1999, 49.

[15] R. GANESH «Fate of azo dye in sludges» Th : Chim.: Virginia polytechnic institute and state university : 1992, p: 193 .

[16] S.J.CULP, F.A.BELAND, R.H.HEFLICH «Mutagenicity and carcinogenicity in relation to DNA adduct formation in rats fed leucomolachite green» Mutation research, 506-507, 2002,55-63.

[17] Zollinger H., Color chemistry, Synthese, properties and applications of organic dyes and pigments. VCH, (1987).

[18] J. Shi, L. Chen, Determination of rhodamine B in lipsticks by high performance liquid chromatography after extraction with AOT reversed micelles. Analytical Methods 6 (2014) 8627.

[19] S. Hammami, Study of the degradation of textile dyes by advanced oxidation processes, Application to the decontamination of industrial effluents, Environmental sciences. University of Marne la Vallee, (2008).
[20] Lambert S.D., Graham N.J.D., Sollars C.J., Fowler G.D., Evaluation of inorganic adsorbents for the removal of problematic textile dyes and pesticides, Water Sci. Technol. 36 (1997) 173-180.
[21] Ramakrishna K.R., Viraraghavan T., Dye removal using low cost adsorbents, Water Sci. Technol.36 (1997) 189-196.
[22] McKay G., Ramprasad G., Mowli P., Desorption and regeneration of dye colours from low-cost materials. Water Res. 21 (1987) 375-377.
[23] Taylor J.S., Jacobs E.P. Water treatment membrane processes, New York, McGraw-Hill, 1996, pp. 9.1-9.70.
[24] Calabro V., Pantano G., Kang R., Molinari R., Drioli E., Experimental study on integrated membrane processes in the treatment of solutions simulating textile effluents. Energy and exergy analysis, Desalination 78 (1990) 257-277.
[25] Van Der Bruggen B., Lejon L., Vandecasteele C., Reuse, treatment and discharge of the concentrate of pressure-driven membrane processes. Environ. Sci. Techn. 37 (2003) 3733-3738.
[26] R.Feng Chen,W. Lang ,H.Tao Zhong, L.ChaoZiang, Q.Wei, W.ChunHai, Evaluation of electrocoagulation process for high-strength swine wastewater pretreatment, Separation and Purification Technology,(Volume 272), (2021).
[27] Dirany A, Sirés I, Oturan N, Özcan A, Oturan MA (2012) *Science & Technology* 46:4074-4082.
[28] Kim I, Yamashita N, Tanaka H (2009) *Chemosphere* 77:518-525.
[29] Jacobs LE, Fimmen RL, Chin Y, Mash HE, Weavers LK (2011) *Weavers water research* 45:4449-4458.
[30] Bian ZY, Zhu YQ, Zhang JX, Ding AZ, Wang H (2014) Chemosphere 117:527–531.
[31] Glaze W, Chapin D (1987) *Ozone Science Engineering* 9:335-342
[32] Huchon R (2006) Doctoral thesis, University of Lyon *I* pp 235
[33] Millet M (1992) L'oxygène et les radicaux libres (Part 2), *Bios* 23:45-50.
[34] Schulte-Oehlmann U, Markert B, Oehlmann J, Development of a biotest with 2007 Marisa cornuarietis (Gastropoda: Prosobranchia) for the assessment of environmental chemicals with sex hormone-mimicking effets. Final report for R&D project 297 65 001/04, *Federal Environmental Agency*, Berlin
[36] Pulgarin C, Adler N, Peringer P, Comninellis C (1994) *Water Research* 28:887-893.
[37] Hadjlarbi, K., *Comparative study of a direct and pulsed electroplating method for TiO_2 and its effect on the photoelectrocatalytic degradation of methylorange (MO)*. 2021.

Chapter II
Theory of semiconductors

Introduction

In order to provide a deeper understanding of the mechanisms involved in the electro-photocatalytic processes discussed in the previous chapter, the present chapter focuses on the theoretical foundations of semiconductors, particularly their electrical behavior under illumination and their interfacial interactions with electrolytes.

II-Theory of semiconductors

II-A. Introduction

Semiconductors play an important role in many modern technological applications, ranging from electronic devices and energy conversion systems to environmental applications such as photocatalysis. To fully exploit their potential, it is essential to master both their synthesis and their characterization. This second chapter is devoted to presenting the semiconductor materials synthesized, their properties and performance, and the synthesis methods used.

We will establish the theoretical bases and methods for synthesizing semiconductors, using the sol-gel technique and chemical synthesis methods, as well as their use in electro-photocatalysis.

II-B. Semiconductors

Semiconductors are a unique group of elements and compounds characterized by specific electrical properties. Unlike good conductors such as metals and metal alloys, which have weakly bonded valence electrons, allowing them to efficiently conduct electricity and heat with a resistivity around 10^{-8} Ω·m (where the band gap is zero), or electrical insulators like ceramics and polymers, which have tightly bound valence electrons, leading to an empty conduction band, a large band gap (up to 10 eV), and a resistivity greater than 10^{8} Ω·cm, semiconductors occupy a middle ground. They have moderate electrical conductivity and generally cannot be classified purely based on atomic bonds. The band gap in semiconductors (typically $E_{gap} > 4$ eV) correlates with bond strength and can result in resistivity reaching up to 10^{12} Ω·cm [1, 2].

The resistivity (ρ) of semiconductors typically ranges from 10^{-3} to 10^{4} Ω·cm, reflecting a lower energy gap compared to insulators, approximately 1 eV. Electrical conductivity in semiconductors is primarily due to free electrons and mobile holes, which serve as charge carriers. Semiconductors are distinguished by having a conduction band (CB) that is partially filled with electrons and a valence band (VB) that is partially empty. These two energy bands are separated by a region devoid of electrons, known as the "gap" or band gap (IB). The valence band represents the highest occupied energy level, while the conduction band represents the lowest unoccupied energy level.

All three types of materials—conductors, insulators, and semiconductors—possess a valence band and a conduction band. What differentiates them is the energy gap between the valence band (VB), which is the highest energy band occupied by electrons, and the conduction band (CB), which represents the lowest unoccupied energy level. This energy difference, known as the band gap, indicates the amount of energy required for an electron to transition from the valence band to the conduction band (Eg = E_CB - E_VB) [3].

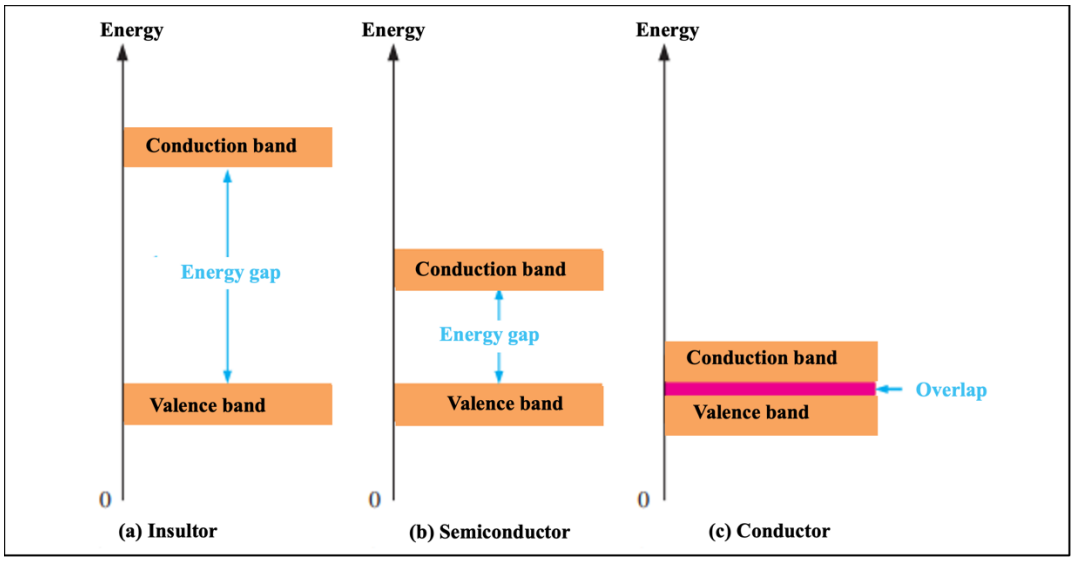

Figure II-B-1. Energy diagrams for the three types of materials [4].

The simple semiconducting elements are those belonging to column 14 of the periodic table, as shown in Figure I.3. Carbon, in the form of diamond, is more appropriately classified as an insulator, since its band gap is of the order of 5.5 eV. Silicon and germanium, which crystallize in the diamond structure, are the two most important fundamental semiconductors.

The elements in columns III and V of the periodic table exhibit minimal ionic character, with most forming structures typical of covalent crystals. These elements tend to behave as semiconductors rather than insulators, reflecting their weak ionic nature. There are nine binary compounds formed from the combination of elements such as In, Ga, and Al with Sb, As, and P: InSb, InAs, GaSb, InP, GaAs, AlSb, AlAs, GaP, and AlP, as listed in the table below. Compounds in the II-VI group, such as PbS, PbSe, and PbTe, share similar structures. The interatomic bonds in these compounds are a mix of covalent and ionic characteristics [5].

Table II-B-1 Semiconductor materials

Column	Semiconductor

IV		Ge, Si
III-V	Binary	GaAs,GaP,GaSb,InAs,InP,InSb
	Trinary	$Al_xGa_{1-x}As$
	Quaternary	$Al_xGa_{1-x}As_yP_{1-y}$
II-VI	binary	CdS, HgTe
	Trinary	$Cd_xHg_{1-x}Te$

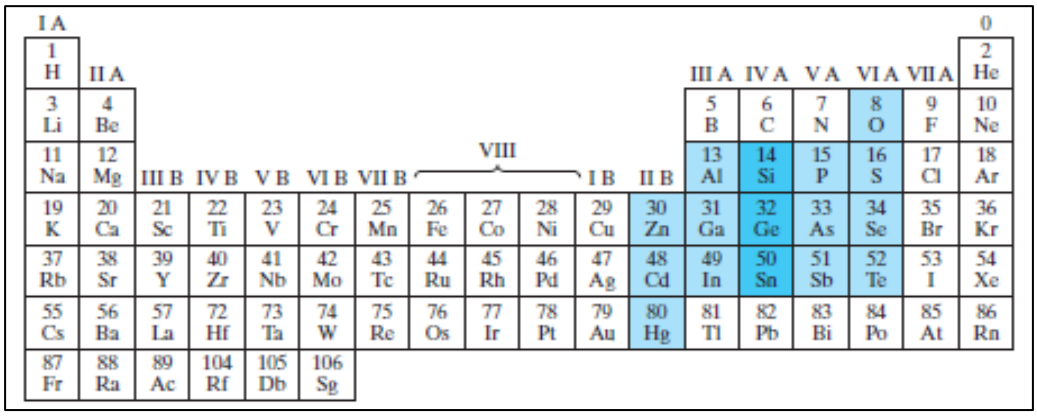

Figure II-B-2. Periodic table with elemental semiconductors in a dark color, and elements that form compound semiconductors in a light color [5]

II-B.1.Types of semiconductors

A semiconductor can be either intrinsic or extrinsic

- Intrinsics can also be referred to as pure elements (Si, Ge) [6, 7].

Extrinsic semiconductors are modified by the deliberate addition of other materials (impurities) and may be N-type or P-type. [5].

II-B.1.1. Intrinsic semiconductor

Intrinsic semiconductors have a low impurity content, generally less than 1 impurity atom per 1013 atoms of semiconductor material. At very low temperatures, they exhibit insulating behavior, but their conductivity increases as the temperature rises **(Figure I.4)**.

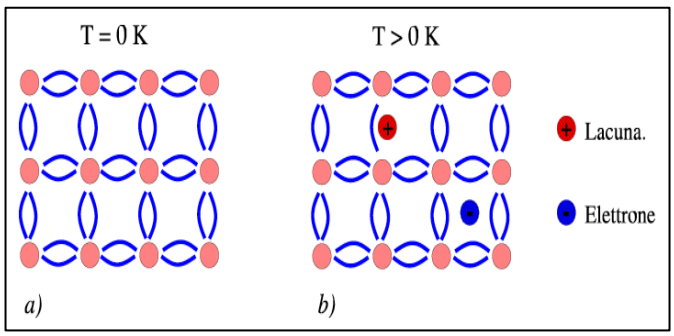

Figure II-B-3. Intrinsic semiconductor

A semiconductor is classified as intrinsic when the number of electrons (n) in the conduction band is equal to the number of holes (p) in the valence band, meaning that the electron and hole concentrations are balanced [8].

Extrinsic semiconductors are created by adding impurity atoms to pure "intrinsic semiconductor" materials, one atom for every 105 atoms of a semiconductor element. Depending on the nature of the impurities. There are two types of external semiconductors Figure I.5.

A semiconductor is classified as n-type when the number of electrons significantly exceeds the number of holes. Conversely, it is considered p-type when the number of holes greatly outnumbers the electrons. Table II.B.2 provides a classification of semiconductors based on their doping type, whether n-type or p-type.

Table II-B-2. Types of external semiconductors.

Type n	In n-type semiconductors, electrons are the majority carriers, with their concentration (n) being much greater than that of holes (p). The dopants used to create n-type semiconductors, known as donors, are elements or compounds that have five or more valence electrons. These dopants release one additional electron after the other four have formed covalent bonds with the intrinsic material into which they are introduced [9].
Type p	A p-type semiconductor operates in contrast to an n-type semiconductor, with holes as the majority carriers (p >> n) and electrons as the minority. P-type semiconductors are created by introducing acceptor dopants, typically elements or compounds with three valence electrons that can readily accept electrons. As a result, electrical conduction in p-type materials is primarily driven by the movement of holes. [9]

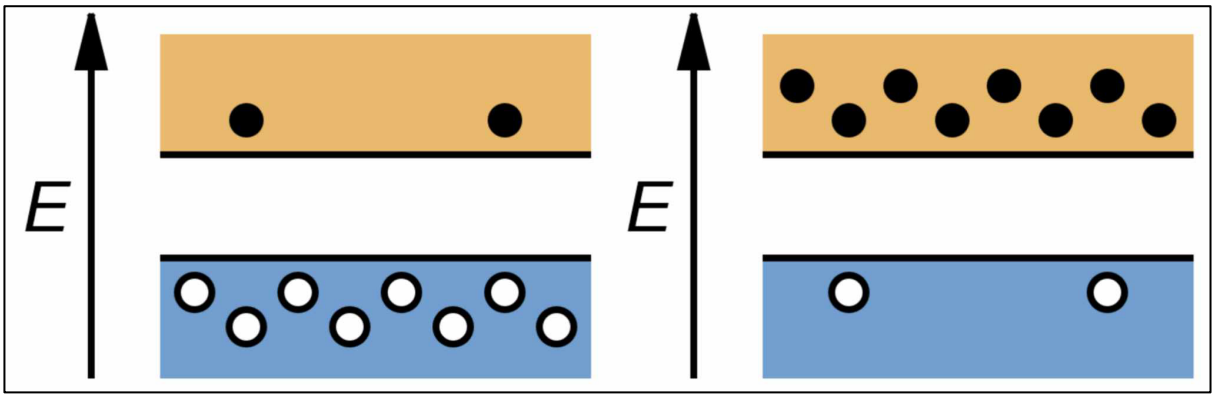

Figure II-B-4. p-type (a) and n-type (b) extrinsic semiconductors [10].

II-C. Electronic exchange at semiconductor/electrolyte interface

II-C.1.The semiconductor/electrolyte junction protected from light

The electronic exchange between the electrode and the electrolyte in the dark is a faster phenomenon than the rearrangement of the atomic layer of the solvent surrounding the ions in the solution. By the Franck-Condon principle [11], this exchange takes place without any change in the chemical configuration of the ions and is isoenergetic, i.e. it can only take place between states of the same energy, to within kT [12].

In the electrolyte, the Gurney model provides a detailed description of the density of both empty and occupied states [13] (Figure II. 9). The empty levels (acceptors) correspond to the oxidized species of the redox couple, the full levels (donors) correspond to the reduced species. The energy difference between the most probable empty and full levels corresponds to the difference in solvation energy of the oxidized and reduced species. The densities of states are given in [14, 15].

$$D_{ox}(E) = n_{ox}(4\pi\lambda kT)^{-0.5} \exp\left[\frac{-(E - E_{ox}^{0})^{2}}{4\lambda kT}\right] \qquad (II.1)$$

$$D_{red}(E) = n_{red}(4\pi\lambda kT)^{-0.5} \exp\left[\frac{-(E - E_{red}^{0})^{2}}{4\lambda kT}\right] \qquad (II.2)$$

Where E_{ox} and E_{red} are the energies of the most probable states, NOx, and need the concentration of oxidized and reduced species. represents the rearrangement energy of the solvated layer between the EF, redox equilibrium level, and the most probable state.

Figure I.5a illustrates the energy band positions of an n-type semiconductor about the density of states in the electrolyte. Exchanges primarily occur with the conduction band, where the majority of carriers are located. However, the transfer of minority carriers happens either through strong band bending, as shown in Figure II.5b, or via localized states at the semiconductor's surface, depicted in Figure II.C.1

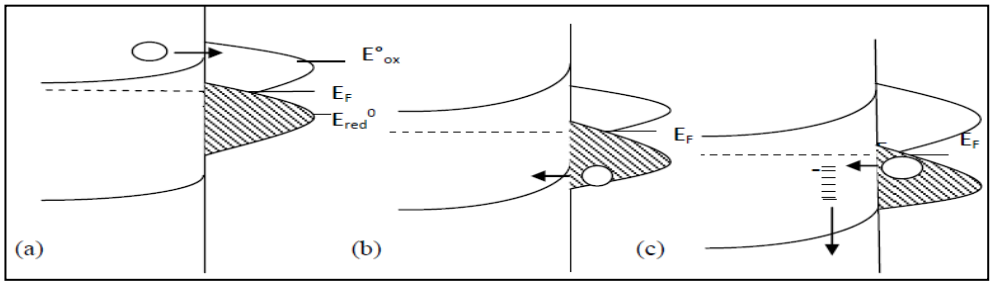

Figure II-C-1. Density of empty and occupied states in an electrolyte and electronic exchange processes at the semiconductor interface: a) low band curvature (exchange with majority carriers); b) high band curvature; c) exchange through surface states.

II-C.2.The semiconductor/electrolyte junction under illumination

When the surface of a semiconductor is exposed to light with energy greater than the band gap Eg (i.e., hν >Eg), the absorbed photons create electron-hole pairs (e−/h+). These pairs are separated by the junction electric field at the interface and exist in the depletion region (space charge region). This process generates a photocurrent (ΔJph) and leads to a reduction in the band curvature at the semiconductor surface.

If the semiconductor electrode is connected to an inert counter-electrode via an external circuit, a photocurrent flows through the external circuit. The minority charge carriers reach the semiconductor/electrolyte interface where they undergo electrochemical reactions with the ions in solution.

Figure I.6 illustrates the typical current-voltage (I-V) curve for a semiconductor/electrolyte junction. In the dark, the junction functions like a chemical diode. The current due to majority carriers (cathodic for a p-type semiconductor and anodic for an n-type semiconductor) is similar to that of a metal electrode, while the current from minority carriers is nearly negligible. However, under high reverse bias (anodic for p-type and cathodic for n-type), a current can emerge, which may be attributed to either tunneling effects of majority carriers or avalanche breakdown phenomena.

When a semiconductor electrode is illuminated, a current is observed in reverse polarization, which starts at a potential close to the potential of the flat band, and which reaches a saturation value, the latter being a function of the luminous flux (φ_0) whose photo potential (U_{ph}) is given by the relation:

$$U_{ph} = kT/e \times \ln \varphi_0 \qquad \text{(II.3)}$$

A straightforward model, based on Gartner's theory **[16]**, describes the emergence of these characteristics under illumination. According to this model, the current density (J) is expressed by the following relation **[17]**:

$$J = e\varphi_0[1 - \exp(-\alpha w)(1 + \alpha L_p) \qquad \text{(II. 4)}$$

α being the optical absorption coefficient:

$$W = (2\varepsilon\varepsilon_0 eN)^{0.5}\left(V - V_{fb} + \frac{kT}{e}\right)^{0.5} \qquad \text{(II. 5)}$$

W : the width of the space charge region and L, the diffusion length of minority charge carriers.

In some cases, αL_p can be neglected in front of unity. This has been verified for compounds used in photoelectrochemistry [18-19]. We then have:

$$J = e\varphi_0\left[1 - \exp\left[-\alpha\left(\varepsilon\varepsilon_0\frac{kT}{eN}\right)^{0.5} - \left(V - V_{bp}\right)^{0.5}\right]\right] \qquad \text{(II. 6)}$$

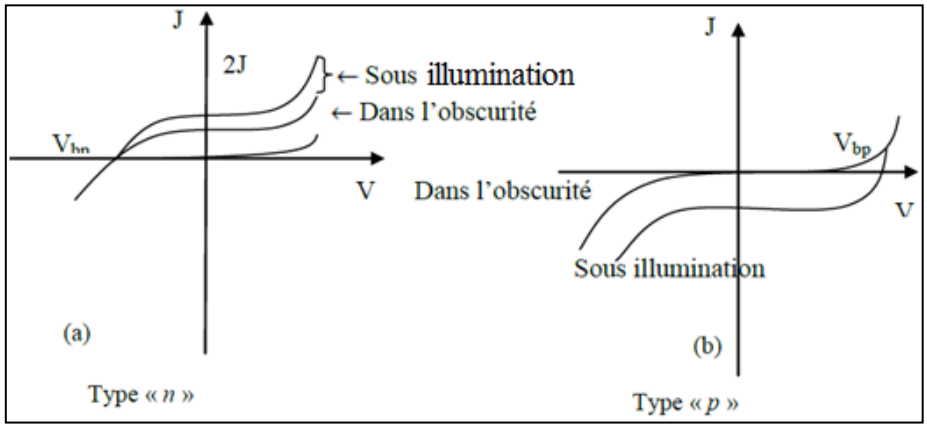

Figure II-C-2. Variation in the current-potential density of a semiconductor/electrolyte junction, in the dark and under illumination a) type (n), b) type (p).

The relationship (II.6) describes the characteristics under illumination in Figure I.10 quite well. The photo-current appears for a potential V greater than the potential Vbp (for a type n); curvature of the bands then appears likely to focus the minority carriers towards the semiconductor/electrolyte interface.

Saturation current is achieved when αW > 1, indicating that all carriers generated within the space charge region contribute to electronic conduction. At this point, the quantum efficiency $\eta = \frac{J}{e\varphi}$, representing the ratio of effective carriers to incident photons, equals 1. This efficiency is significantly lower compared to thin films, where it can reach up to 20%.

References:

[1] Shackelford, J.F., Introduction to Materials Science for Engineers.

[2] GUELIL, W. and S.E. Douafer, Synthesis and characterization of a nickel-based semiconductor material. 2021, University of jijel.

[3] Nada, A. and B. Hocine, Photocatalytic and photoelectrochemical study of some semiconductors. 2020, university of jijel.

[4] Callister, W.D. and D.G. Rethwisch, *Materials Science and Engineering*. 2014: Wiley.

[5] Souici, A. and G.J.U.B. de Cristallographie, *Physique des Semi-conducteurs.* 2013.

[6] Laouici, R., *Development of semiconductor materials and study of their environmental applications*. 2023.

[7] BOUBLENZA, D.E. and A. ZAOUI, *Modelling new semiconductors using a first-principles method*. 2022.

[8] Toupin, J., *Water splitting: study of p-type semiconducting materials as photocathode for protons reduction into H2Photoelectrolysis of water: study of p-type semiconductor materials as photocathodes for the reduction of protons to H2. 2016, Pierre and Marie Curie University - Paris VI.*

[9] Moradi, Z., Jahromi, S. Z., & Ghaedi, M. Moradi, Z., Jahromi, S. Z., & Ghaedi, M. , *Design of active photocatalysts and visible light photocatalysis. In Interface science and technology.* Elsevier, 2021. **Vol. 32**: p. pp. 557-623.

[10] Kittel C (1983) Solid State Physics. 5th Edition, Paris.

[11] Biemont E (2008) Molecular Spectroscopy: Molecular Structures and Analysis. 1st edition De Boeck, Brussels.

[12] Gerischer H (1970) Physical Chemistry, Vol. IX A, Eyring, H., Henderson, D. et Jost, W., Ed. (Academic Press), New York, p. 463.

[13] Gurney RW (1931) Proc. Roy. Soc. A 134:137.

[14] Gerischer H (1969) Surf. Sci. 18:97.

15] Van Den Berghe RAL, Cardon F, Gomes WP (1973) Surf. Sci. 39:368.

[16] Gärtner WW (1959) Phys. Rev. 116:84.

[17] Butler MA (1977) J. Appl. Phys. 48:1914.

[18] Belabed C, Rekhila G, Doulache M, Zitouni B, Trari M (2013) Sol. Energy Mater. Sol. Cells, 114:199.

[19] Zidi N, Omeiri S, Hadjarab B, Bouguelia A, Akroun A, Trari M (2010) Physica B: Condens.

Chapter III
Synthesis methods and Analysis techniques

III- Synthesis methods and analysis techniques

In this chapter we will describe the experimental work which will be divided into 2 successive parts, the first consists of synthesising $CuFe_2O_4$ and Ba_2SnO_4 semiconductors. The second part of this chapter will be devoted to their characterisation using various optical, radiocrystallographic, electrical, physical and photo-electrochemical microscopic analysis methods.

III-A. Synthesis methodology and electrode preparation

Solid-state chemistry offers various ways of preparing mixed oxide catalysts (scheelite, perovskite, spinel, delafossite). The electro-catalytic properties of these catalysts depend on the preparation method and conditions, as well as the synthesis temperature. The aim is also to increase their specific surface areas, which gives them higher catalytic activity through a geometric effect. The various known methods for synthesising mixed oxides are wet synthesis, dry "solid state" synthesis, sol-gel synthesis, hydrothermal synthesis, etc....

Wet synthesis can be defined as a method of preparing fine particles of material in an open system. This type of preparation includes: co-precipitation, co-decomposition, ice vaporisation, sol-gel process, spraying and pyrolysis etc., the wet method allows precise control of the physical and chemical properties of the powders and procurers with other advantages:

- Homogeneity
- Uniformity of particle shape

In this chapter we focus on the sol gel synthesis and chemical synthesis of our $CuFe_2O_4$ and Ba_2SnO_4 semiconductors. We also describe the various methods adopted to characterise their properties: structural, optical, electrical and photoelectrochemical.

III-B. Presentation of reagents

For this study, we use various chemical reagents, two of which will be used in particular to prepare our samples:

III-B.1. Hydrated copper-nitrate

The copper nitrate used in our study: Cu $(NO_3)_2 3H_2O$ powder manufactured by BIOCHEM chemopharma (France), with a purity of 98%

Table III-B-1. Properties of copper nitrate [1]

Chemical formula	$Cu(NO_3)_2 \cdot 3H_2O$
Melting point	114 °C
Density	2.05 g/cm3 (20 °C)
Molar mass	241.60
Solubility in water	2670 g/l

Figure III-B-1. Copper nitrate

III-B.2. Iron nitrate hydrate

Iron nitrate hydrate is manufactured by BIOCHEM chemopharma (France) and has the formula Fe $(NO_3)_3$-$9H_2O$ with a purity of 98%. The table below shows its properties.

Table III-B-2. Properties of iron nitrate hydrate [2]

Chemical formula	**Fe $(NO_3)_3 \cdot 9H_2O$**
Masse molaire	403.99
Melting point	47.2 °
Density	1,68 g/cm³
Solubility in water	at 20ºC: 1,68 g/cm3

Figure III-B-2Iron nitrate hydrate

III-C. Synthesis of $CuFe_2O_4$ by the sol gel method

$CuFe_2O_4$ was synthesized by sol gel method, by dissolving $Cu(NO_3)_3(H_2O)_6$ (99%) and $Fe(NO_3)_3(H_2O)_9$ (99%) in water, with molar ratio (1/2). Agar-Agar was used as gelling agent (1 g/1000 mL); the mixture was treated at ~ 70 °C under stirring until the formation of a dense gel which was dehydrated at 100 °C and denitrified ~ 300 °C. Finely,

the amorphous powder was crushed and fired at 800 °C for 16 h in a programmed tubular furnace (10 °C mn $^{-1}$). The powder was compacted (3 tons/cm ^{2}) (Æ = 13 mm) and annealed at 800 °C.

III-D. Synthesis of Ba_2SnO_4 by the chemical synthesis method

The perovskite Ba_2SnO_4 was elaborated by chemical route. Stochiometric amounts of $BaCO_3$ (Merck, 99%) and SnO_2 (Riede-de Haen, 99.5%) were dissolved in HNO_3 (65%), evaporated on a hot plate and denitrified at 400 °C in a ventilated place. The amorphous powder was ground in an agate mortar and heated at 900 °C in air. The powder was reground, pressed into pellets and sintered at 1050 °C, the compactness averages 90%. The reduction was carried out by heating $Ba_2 SnO_4$ pellets in glass tube at 600 °C under dynamic vacuum (1 mbar).

III-E. Preparation of pellets

The characterisation of transport, electrochemical and photoelectrochemical properties requires the use of compact pellets with high mechanical properties. To achieve this, the oxide powder was compressed under a single axial pressure of 5 Kbar using a mechanical press (pelletiser), Figure III.E.1

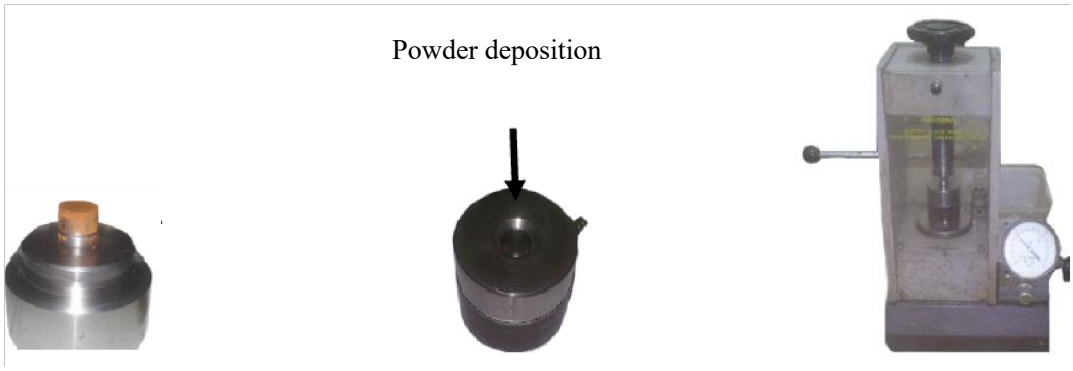

Figure III-E-1. Device used to produce the pellet

III-E.1. Preparation of the working electrode

Electrochemical studies and electro-photocatalysis require the use of a working electrode. To produce the latter, silver lacquer is spread on one of the surfaces of the pellet to minimise contact resistance, Electrical contact is then made with the pellet using a copper wire soldered to the surface of the pellet using tin, and the assembly is insulated with epoxy resin using a glass tube so that only the rear surface of the pellet is in contact with the electrolyte (Figure III.E.2).

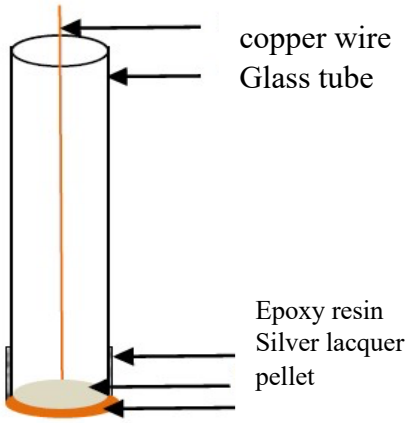

Figure III-E-2. Working electrode

Figure III-E-3. experimental set-up for electrophotocatalysis of methyl orange under solar irradiation

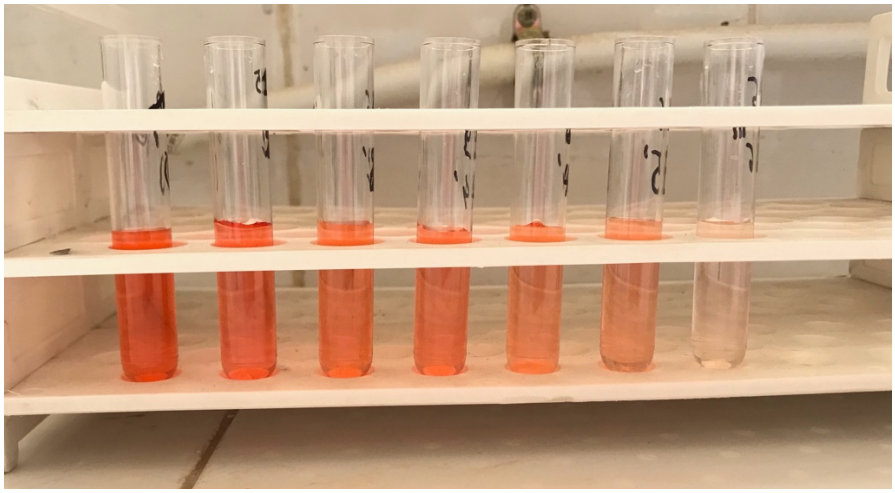

Figure III-E-4. Samples of 3ml every 20 min for 2h of methyl orange lectrophotocatalysis.

III-F. CHARACTERISATION TECHNIQUES

III-F.1.1. X-ray diffraction - XRD

The purity of the synthesised oxides was checked by X-ray diffraction spectroscopy (BRÜKER D5005) using Kα radiation from a copper anticathode (λ= 0.154178 nm). X-ray crystallographic analysis was carried out in order to identify the phases formed, index the peaks by comparing them with those in the American Society for Testing and Materials

(ASTM) data sheets taken from the X-Powder software. The crystallite size (D) was estimated using Scherrer's empirical relationship.

The Scherrer method is used to estimate the average size of crystallites in the 2-1000 nm range. In many cases, this approximate method is sufficient to characterise catalysts.

Scherrer's formula is written :

$$D = \frac{K.\ \lambda}{\beta\ .\cos(\theta)} \qquad \text{(III. 1)}$$

D : the average size of the crystallites.

K : Constant = 0.94.

$\boldsymbol{\lambda}$: Monochromatic wavelength = 1,5406 nm.

$\boldsymbol{\beta}$: Width at half-height in radians of most intense peak.

$\boldsymbol{\theta}$: Bragg diffraction angle at the peak of the strongest line.

The density is given by the following formula:

$$S = \frac{6}{\rho^{exp} \times D} \qquad \text{(III. 2)}$$

Where:

M: molar mass.

N: Avogadro number.

a, c: cubic mesh parameters.

The Specific surface area is deduced from the relationship:

$$S = \frac{6}{\rho exp/23\ \times D} \qquad \text{(III. 3)}$$

where ρ^{exp} is the experimental density.

III-G. Scanning electron microscopy

The SEM is used to acquire high-resolution images of the surface of a solid sample.

SEM works by using a beam of electrons to travel across the surface of the sample. When these electrons interact with the sample material, they can give up energy and produce secondary electrons, backscattered electrons and X-rays. These signals are then detected and used to create an image of the sample surface [3].

In our study, we used a scanning optical microscope of the thermoscientific brand Axia

III-H. Fourier Transform Infrared Spectroscopy

Fourier Transform Infrared Spectroscopy is a chemical analysis technique that uses infrared to study molecular vibrations and obtain information about the composition and structure of samples. The FTIR technique is based on the absorption of infrared radiation by molecules, which occurs when the energy of the infrared beam coincides with that of molecular vibrations. The wavelengths used in FTIR range from 4000 cm^{-1} to 400 cm^{-1}, corresponding to 2.5 - 25 µm, and are in the so-called mid-infrared, the region where the majority of molecules vibrate.

However, some molecules, notably homonuclear diatomic molecules such as nitrogen (N_2) and oxygen (O_2), do not show absorption in this spectrum due to the absence of dipole moment[4].

There are two main types of vibration:

- Stretching along the axis of the link
- Bending, which causes a change in the angle between two adjacent links, in or out of the plane. These elongations and deformations can be symmetrical or asymmetrical.

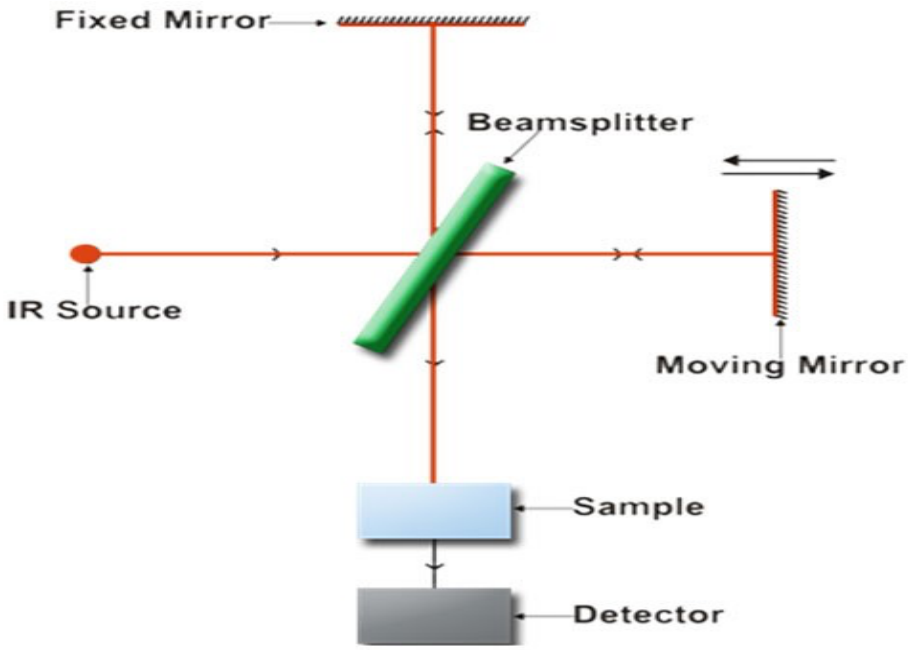

Figure III-H-1. Principle of Fourier transform infrared spectroscopy (FTIR)

III-I. Electrochemical characterisation

III-I.1.1. Electrochemical assembly

The electrochemical tests were carried out using an electrochemical workstation (VOLTALABmaster PGZ301), controlled by Volta Master 4 software. Figure III.I.1 shows the experimental set-up used.

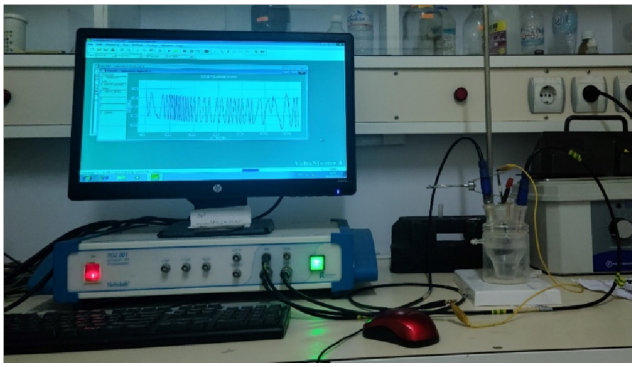

Figure III-I-1. Apparatus for electrochemical measurements

III-I.2. Electrochemical cell

A three-electrode electrochemical cell was used; a reference electrode (ECS); the potential of the ECS at 25°C relative to the normal hydrogen electrode (ENH) is E = 0.241 2 V at 25°C, and a chemically inert counter-electrode (Auxiliary Electrode), made of platinum, which allows the flow of electric current to balance the redox reactions occurring at the working electrode; it is not directly involved in the electrochemical reaction of interest, but serves to complete the electrical circuit. The counter electrode is usually made from an inert conductive material, such as platinum or other inert metals. This material must be electrochemically stable, as it must with stand the conditions of the electrochemical cell without degrading or reacting chemically.

The working electrode ($CuFe_2O_4$ elaborated), is connected by a copper wire at the back and installed in the cell where only one face is in contact with the electrolyte. All the experiments were carried out in aerated solutions without stirring.

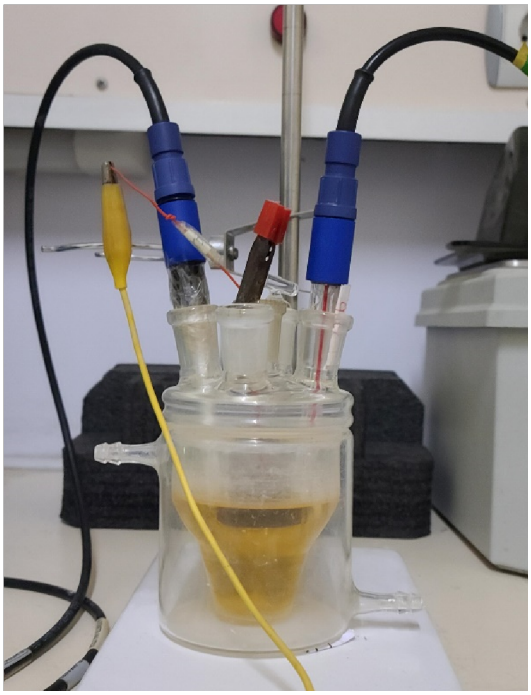

Figure III-I-2. Electrochemical cell

Coating of working electrodes

The working electrodes to be examined, measuring 16 to 17 mm in diameter, were connected to a conductive copper wire. Before proceeding with the experiment, it was necessary to use a conventional coating process using a synthetic resin resistant to acids and bases, leaving only one bare face of the sample in contact with the working medium.

Polishing electrodes

The preparation procedure used to treat the surface of samples in contact with the medium is described below:

The electrodes were presented in the form of discs with a diameter of 16.17 mm; mechanical polishing was carried out by a 'Le Cube' polishing machine, with two speeds of 150 and 300 rpm and two directions of rotation, using Sic metallographic paper (600-1200).

Experimental techniques

The choice of working environment consists of using a solution of (Na_2SO_4 (3.5g/l), textile (20mg/l)) which simulates the conditions generally encountered in industrial environments.

Open circuit potential (OCP): This was measured for at least 120 minutes for all samples.

Cyclic volta: The tests were carried out in a potential range varying between -1200 mV and 1200 mV with a scanning speed of 10mV/s.

The same thing was done for the electrode (Ba_2Sno_4 Elaborated)

III-J. Analysis by UV-visible spechtrometry

Spectrophotometry is a quantitative analytical method that involves measuring the absorbance or optical density of a given chemical substance in solution. When a substance absorbs light in the ultraviolet and visible range, the energy absorbed causes disturbances in the electronic structure of atoms, ions or molecules. One or more electrons use this energy to jump from a low energy level to a higher energy level. These electronic transitions take place in the visible range, from 350 to 800 nm, and in the ultra-violet range, from 200 to 350 nm.

- A homogeneous medium through which light passes absorbs some of it; the different radiations making up the incident beam are absorbed differently depending on their wavelength, and the radiations transmitted are therefore characteristic of the medium.
- A monochromatic ray of light of wavelength λ passes through a homogeneous medium of thickness l. The rate of decay of the light intensity as a function of the thickness of the absorbing medium is given by Lambert's law:

- $A = \log\left(\frac{I_0}{I}\right)$ **(III.1)**

I_0: initial intensity of the light.
I : intensity of transmitted light.
A : absorbance.

The optical density of the solutions is determined using a spectrophotometer that has been calibrated to the adsorption wavelength of the chemical species..

- If the homogeneous medium is a solution of a compound with a molar concentration C (expressed in $mol.L^{-1}$), absorbent in a transparent solvent then:

$$k = \varepsilon.c \qquad \textbf{(III.2)}$$

- k is the absorption coefficient, the ratio I_0/I is the transmission,

$$A_\lambda = \varepsilon_\lambda I.C \qquad \textbf{(III.3)}$$

$\boldsymbol{A_\lambda}$: is the absorbance of the solution at the wavelength.

C : ($mol.L^{-1}$) is the concentration of the absorbing species.

l : (cm) is the optical path.

ε_λ :($mol^{-1}.L.cm^{-1}$) is the molar extinction coefficient, an intrinsic quantity of a compound under given conditions. ε depends on the wavelength used, the temperature and also the nature of the solvent (l being expressed in cm) **[5]**.

Measurements were carried out using a Thermo GENESYS 10uv spectrophotometer (Figure III.J.1). Absorbance measurements were applied to solutions sampled under well-defined operating conditions.

Figure III-J-1. UV-visible spectrophotometer Thermo-GENESYS 10 uv

III-K. Energy consumption

The energy consumed is another important parameter in determining the cost of an electrochemical process. **[6]**.

E $_{Abat}$ (Wh/ppm) is the amount of energy required to achieve a particular methylorange removal (III.4). In other words, it is the amount of energy consumed (Wh) to remove one ppm of methylorange. This parameter is based on time (t) in hours, voltage (U) in volts, intensity (I) in A, and abatement (ppm).

$$E_{Abat} = \frac{U.I.t}{Abat} \qquad \textbf{(III.4)}$$

References chap 3:

[1] Corporation, M. *Copper(II) nitrate trihydrate CAS 10031-43-3 | 102753. (s. d.)*. Available from: https://www.merckmillipore.com/INTL/en/product/CopperII-nitrate-trihydrate,MDA_CHEM-102753?ReferrerURL=https%3A%2F%2Fwww.google.com%2F. (cited 2024)

[2] millipore, m. *Iron(III) nitrate nonahydrate CAS 7782-61-8 | 103883. (s. d.)*. [cited 2024 12/05/2024];Available from: https://www.merckmillipore.com/INTL/en/product/IronIII-nitratenonahydrate,MDA_CHEM-103883?ReferrerURL=https%3A%2F%2Fwww.google.com%2F.

[3] *Scanning electron microscopy - Materials Research and Analysis Platform (PRAM) - University of Sherbrooke.*

[4] Servant, L., G. Le Bourdon, and T.J.P. Buffeteau, *Understanding infrared spectroscopy: principles and application.* 2011(53): p. 68-73.

[5] G.W. Ewing, Instrumental Methods of Chemical Analysis, NY: MacGraw-Hill. 1975

[6] A. Khennoussi, A. Chaouch, M. & Chahlaoui, (Treatment of red meat slaughterhouse effluents by electrocoagulation-flotation with iron electrodes)/ Journal of Water Science, (2013) 26 (2), 135–150.

Chapter IV
Results and discussion

IV- Results and discussion

IV-A. Characterisation of perovskite and spinel semiconductors Ba2SO4 and CuFe2O4

IV-A.1. X-ray diffraction analysis

All XRD lines (**Fig IV.A. 1A**) belong to $CuFe_2O_4$ are indexed in a tetragonal system (SG: I41/amd N° 141); the diffractogram is free from lines of secondary phases like the delafossite $CuFeO_2$ **[1]**. The lattice parameters, a = 0.584 nm and c = 0.863, agree with the JCPDS Card N° 34–0425; the distortion

The diffractogram shows medium lines, characteristic of small particles. The latter (D = 47 nm), estimated from the broadening (β) at mid-height of the strongest XRD line {(211, $D = 0.94\lambda/\beta \cos\theta$)} **[2]**, is different from that determined by the particle size analyzer (444 nm), and this indicates an agglomeration of particles where each grain is formed of approximately ten crystallites.

All XRD peaks (**Fig.IV.A. 1B**) belong to the double perovskite Ba_2SnO_4, it is indexed in a monoclinic unit cell with a tolerance factor (1.01: considering Shannon ionic radii) and lattice constants: a = 0.414 nm and c = 1.330, in good agreement with the JCPDS Card N° 43-0010. It is characteristic of a single phase with a perovskite structure. The pattern is indexed in a tetragonal symmetry (SG: I4/mmm) The peaks are not broadened, indicating a well-crystallized oxide with a large crystallite size. The experimental density (6.04 g cm^{-3}) is close to that calculated on the basis of two formula weights by unit cell (6.60 g cm^{-3}). The quasi twodimensional lattice Ba_2SnO_4 consists of perovskite-like corner linked SnO_6 layers connected by the rock salt-like BaO sheets. The structure is a rotationally distorted perovskite, and the SnO_6 octahedra around the [001] direction decrease the symmetry from cubic to quadratic, thus tripling the parameter ($a_q \sim 3a_c$) **[3]**. After heating under dynamic vacuum at 600 °C, $Ba_2SnO_{4-\delta}$ acquired *n* type conduction with oxygen vacancies due to mixed valences $Sn^{4+/2+}$ generated by a charge compensation mechanism. The XRD pattern exhibits slightly broadened peaks, indicating smaller crystallites. The crystallite size (50 nm), evaluated from the broadening (β) of the most intense XRD peak (110, $\beta = 0.94\lambda/\beta\cos\theta$), is very different from that obtained by Zetasizer (659 nm) (**Fig.IV.A.2B**), indicating clearly an agglomeration process where each grain is formed by about ten crystallites.

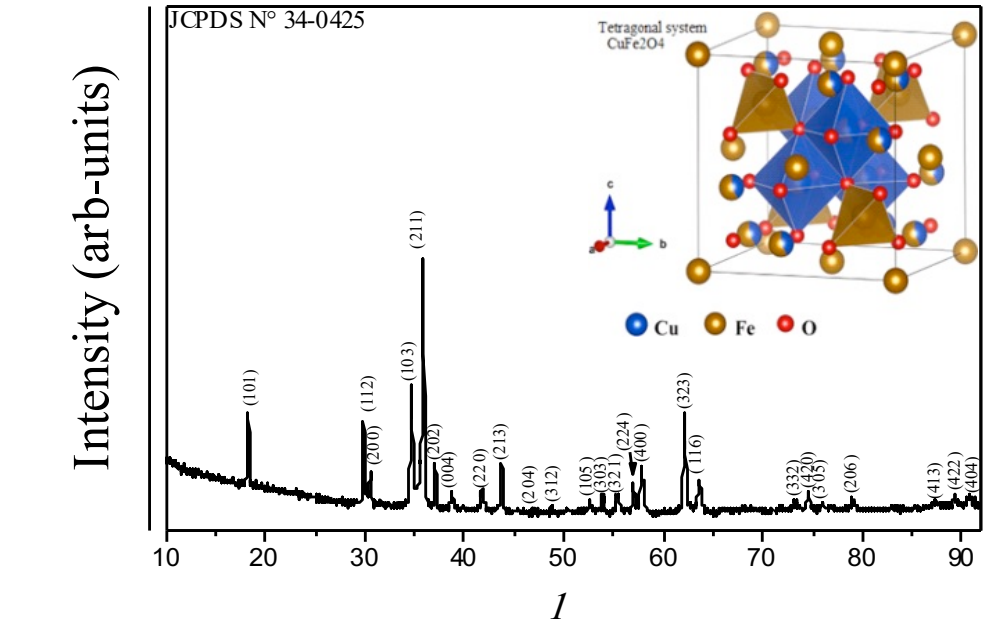

1

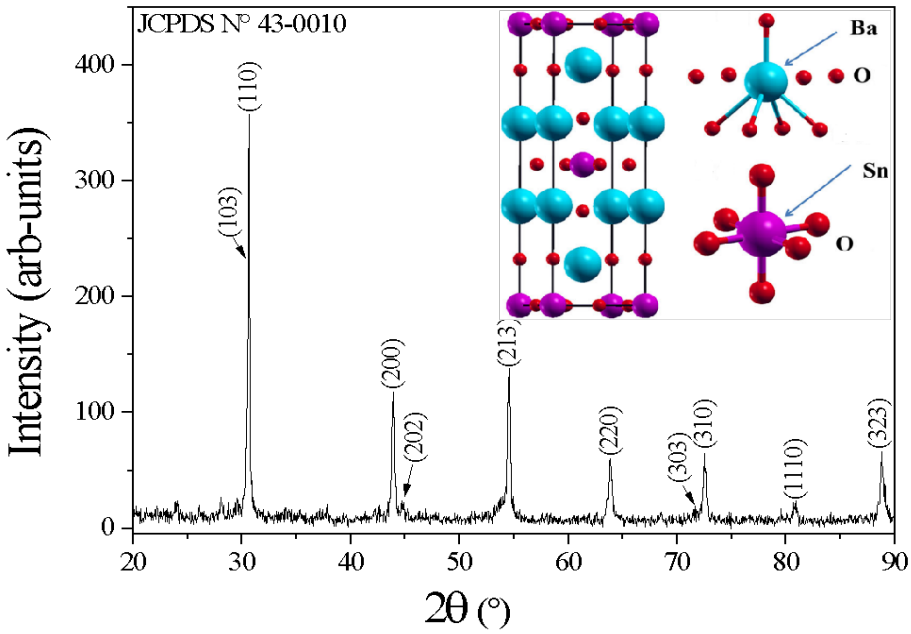

Figure IV-A-1. X-ray difraction pattern of solides (A) $CuFe_2O_4$ (B) Ba_2SnO_4

IV-A.2.Scanning electron microscopy (SEM) and zetasizer of $CuFe_2O_4$ and Ba_2SnO_4

The morphology of $CuFe_2O_4$ shows a compact structure with a rough surface and medium porosity (Fig.IV.A. 2A) with a zeta potential of − 35 mV (Fig.IV.A. 3B) . Such a negative value indicates that OH− species are preferentially adsorbed on the interface.

The SEM micrograph of Ba_2SnO_4 (Fig.IV.A. 2B) indicates a compact structure with a rough surface and a small porosity. Assuming spherical and non-porous crystallites, the image shows regular grains formed by crystallites with a mean dimension of ~ 3 µm, a narrow size distribution (500–900 nm) and a zeta potential of -20 mV (Fig.IV.A. 3D) **[4, 5]**.

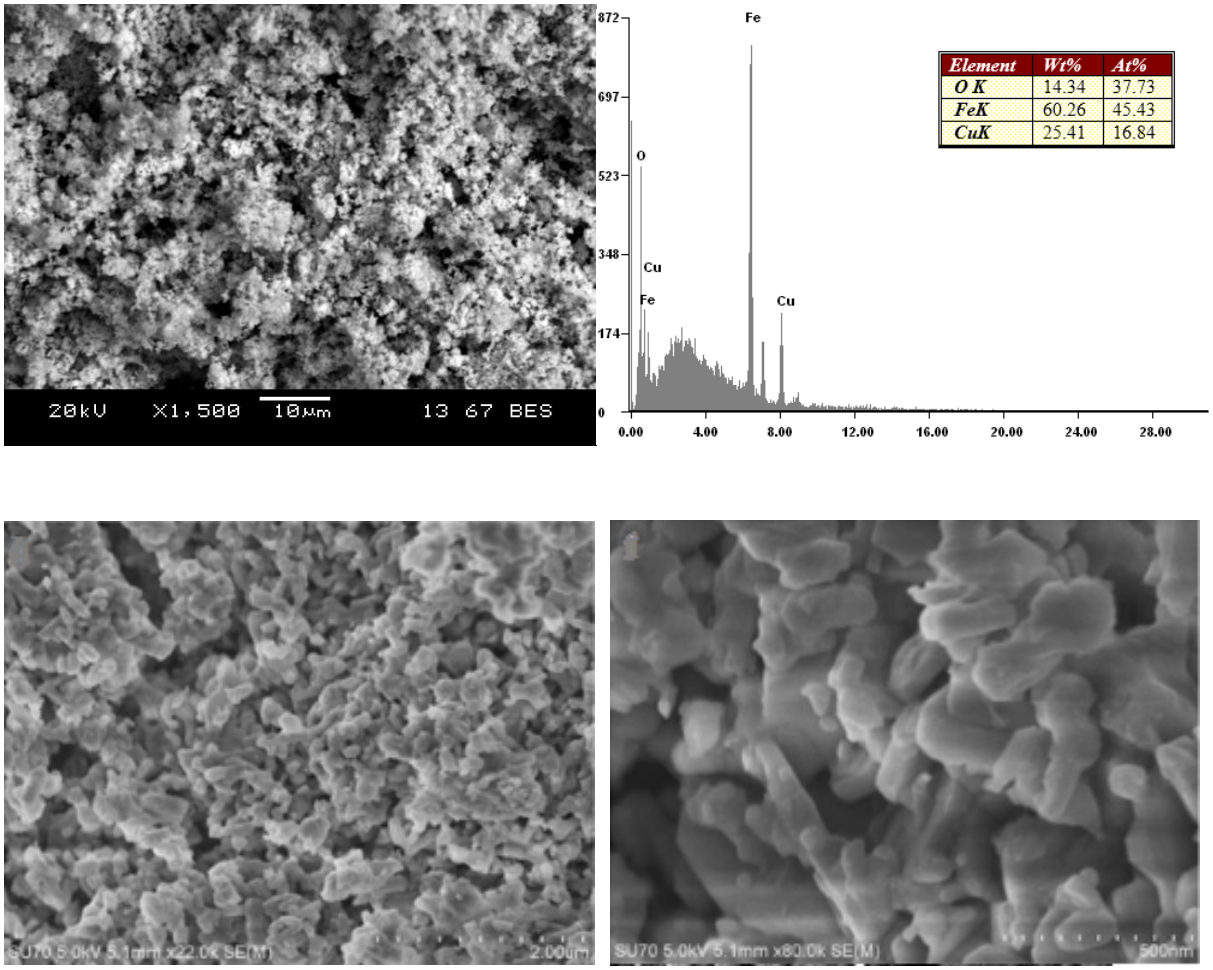

Figure IV-A-2.(A) SEM image and EDX of $CuFe_2O_4$ powder, (B) Low magnification FE-SEM image of rice-like Ba_2SnO_4 nanocrystals.

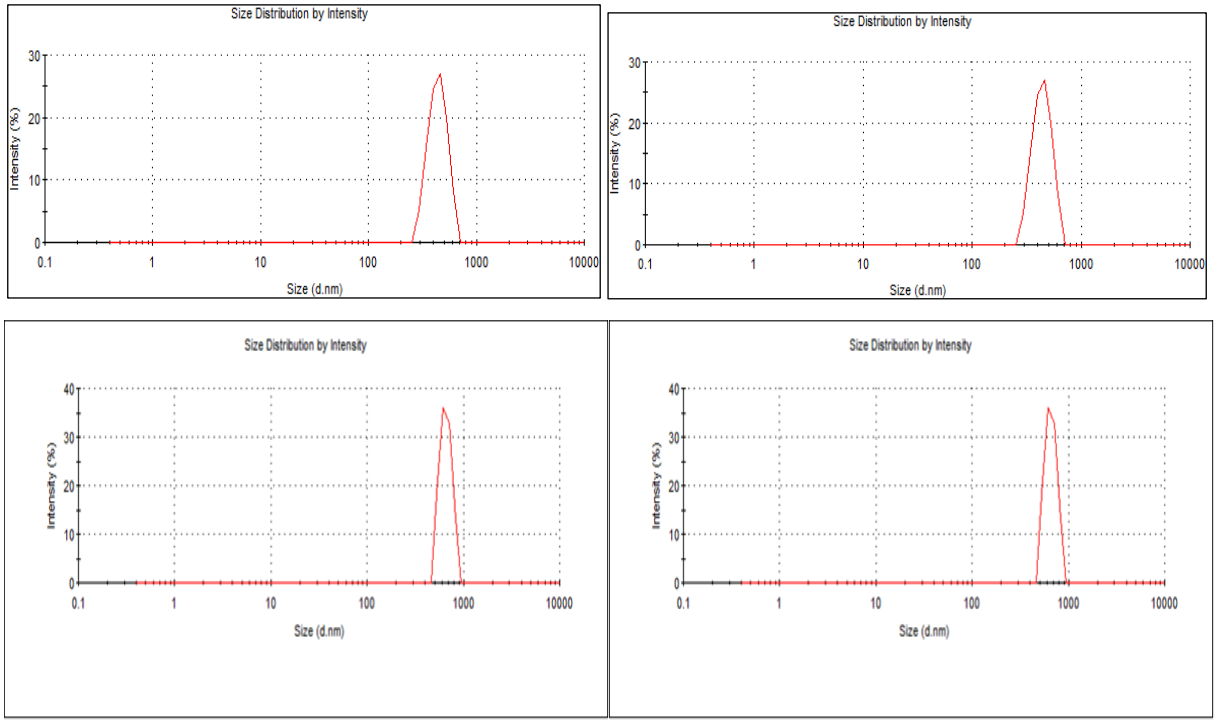

Figure IV-A-3. Sice d istribution by intensity of $CuFe_2O_4$ powder (445 nm), (B) Zeta potential distribution of $CuFe_2O_4$ (-35 mV). (C) Size distribution of Ba_2SnO_4 (659 nm), (D) Zeta potential distribution of Ba_2SnO_4 (- 20 mV).

IV-A.3. FTIR analysis of $CuFe_2O_4$ and Ba_2SnO_4

The FT-IR spectrum of $CuFe_2O_4$ exhibits a stretching vibration band at 3650 cm^{-1} characteristic of O–H, belonging to sorbed H_2O molecules on the catalyst surface, indicating a certain hygroscopy of the spinel supported by the weak peak at 1675 cm^{-1} is due to O–H vibration (Fig. IV.A.4A) **[6, 7]**. The peaks at 475 and 790 cm^{-1}, below 1000 cm^{-1} for inorganic bonds, are assigned to Cu–O and Fe–O, respectively, in octahedral and tetrahedral sites in the normal spinel $Cu[Fe_2]O_4$ **[8, 9]**.

The FT-IR spectrum of Ba_2SnO_4 is essentially featureless down to 1500 cm^{-1} while the absorptions over the range (400– 1000 cm^{-1}) are associated with stannate bulk skeletal. The high intensity peak at 636 cm^{-1} is assigned to Sn–O stretching vibration of SnO_6 regular octahedra while the peak at 505 cm^{-1} is due to Ba–O bond **[10]**. Besides these characteristic bands, a few more peaks having weak intensity are observed at 900 cm^{-1}, 1050 cm^{-1}, 1430 cm^{-1}, 3400 cm^{-1}. The absorption bands at 900 and 1050 cm^{-1} are the characteristic bands of CO_3^{2-}, probably due to adsorbed carbonates by physisorption **[11]**. The peak at 1430 cm^{-1} corresponds to stretching modes of O–H bond; the wide band at ~3400 cm^{-1} is also due to water adsorbed by physisorption at the surface of (Fig. IV.A.4B) **[12]**. Due to lower particle size (50 ± 2) nm, the surfaces are found to be more reactive which may be a possible reason for the adsorption of–CO_2 and –OH on the surface of materials.

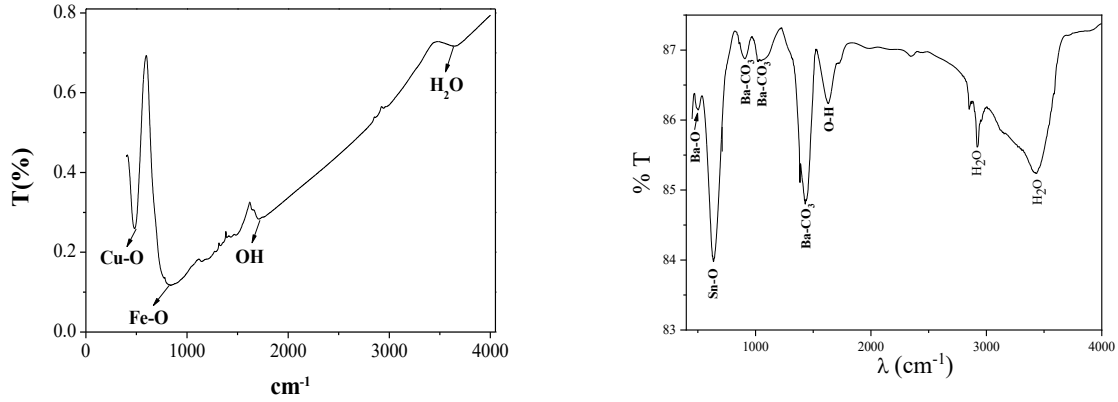

Figure IV-A-4. (A) Infrared spectrum of $CuFe_2O_4$ obtained by Sol Gel method, (B) Ba_2SnO_4 prepared at 1050 °C

Physical and electrochemical measurements were carried out to position the two prepared materials' electronic band levels and predict the oxidation-reduction and photocatalytic reactions at the SC/electrolyte interface.

IV-A.4. Optical properties of $CuFe_2O_4$ and Ba_2SnO_4

The optical absorption coefficients (α) and the forbidden band (E_g) are related by the Tauc relation **[13]** :

$$(\alpha h\nu)^k = \text{Constant} \times (h\nu - E_g) \qquad \text{(IV.A.1)}$$

The exponent ***k*** is equal to 2 or 0.5 respectively for direct or indirect transitions. The derivative of the reflectance with respect to wavelength allows us to determine the transition (Fig.IV.A.5A), closest to the extremum (λ_{max}) of the curve $dR/d\lambda$. The extrapolation of the line $(\alpha h\nu)^2$ to the energy axis gives a direct gap of 1.55 eV (Fig. IV.A.5B) similar to that reported elsewhere **[14, 15]**, and corresponds to transition $Fe_{oc}^{3+}: t_{2g} \rightarrow Fe_{oc}^{4+} : e_g$, associated to the lift of degeneracy in the crystal field splitting of Fe^{3+}:*3d* level in 6-fold coordination ($^6S_{5/2}$) with a theoretical magnetic moment of 5.9 μ_B. Such gap enables a high absorption of solar radiation, precluding energy losses, further transition indirect allowed is also observed at 1.72 eV. The exchange of electrons in $CuFe_2O_4$ takes place between FeO_6 octahedra, a transition in the UV region occurs from occupied O^{2-}: *2p* levels to empty Fe^{3+}: *3d* upper state **[16]** but not observed in our case.

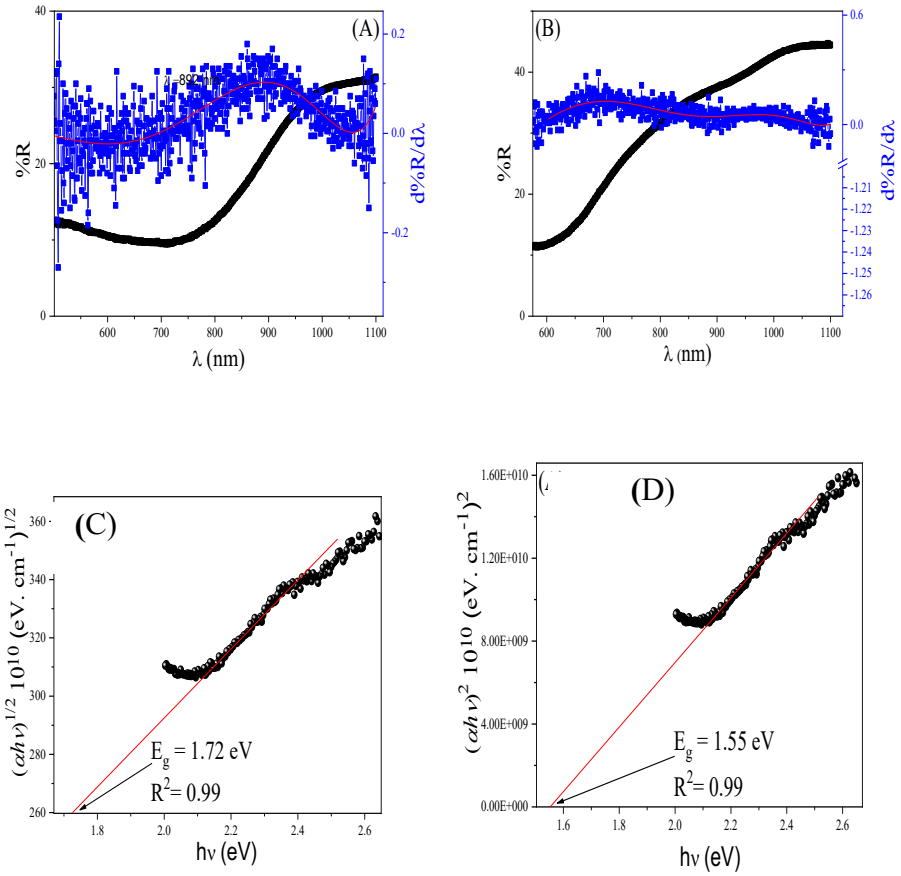

Figure IV-A-5. (A) The direct and (B) derivative of diffuse reflectance of $CuFe_2O_4$ (C) The direct and indirect (D) optical transitions of $CuFe_2O_4$.

For Ba_2SnO_4 the extrapolation of the linear part $(\alpha h\nu)^2$ to the energy axis gives an direct gap of 3.18 eV (Fig .IV.A. 6A) corresponds to the charge transfer O^{2-} : *2p*→Sn^{4+}: *5s*. It is due to the small electron affinity of barium which decreases the covalency of the valence band (Sn–O) π and simultaneously increases the energy of the antibonding conduction band energy. The large difference between the Sn^{4+}: *5s* and O^{2-} : *2p* makes the overlapping weak, leading to a narrowing of the band width. Further indirect transition is observed at 2.72 eV (Fig. IV.A. 6B) **[17, 18]**. The system is electrically neutral and the formation of oxygen vacancies, generated by heating under vacuum, is achieved concomitantly with reduction of Sn^{4+} (Fig. IV.A.6A. Inset) :

$$Ba_2SnO_4 \rightarrow Ba_2SnO_{4-\delta} + 2\ \delta[e^-(CB)] + \delta/2\ O_2 \quad (IV.A.2)$$

The conduction occurs by electron hopping between mixed valences $Sn^{4+/2+}$ accommodated in edge sharing octahedra. Ba_2SnO_4 is chemically stable over the whole pH range, even in strong acid solutions.

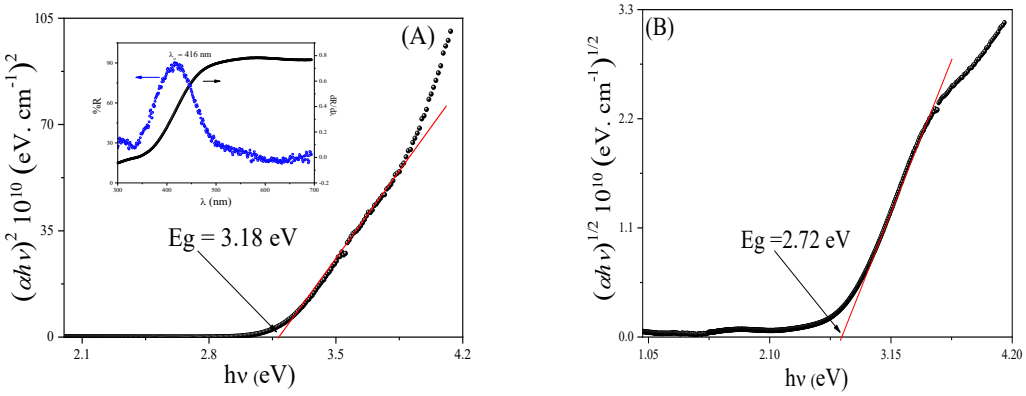

Figure IV-A-6. (A) The direct (A) and indirect (B) optical transitions of Ba_2SnO_4. Inset: Derivative of diffuse reflectance.

IV-A.5.Transport properties

The key parameter in photocatalysis is the semiconductivity of the material, and we have undertaken a study on the transport properties of our ferrite and barium stannate. The logarithm of the conductivity (log σ) varies linearly with the reciprocal temperature; a sign of semiconducting behavior (Fig. IV.A.7),

$$log\sigma = log\sigma_0 - \frac{E_a}{RT} \qquad \text{(IV.A.3)}$$

The least squares method for $CuFe_2O_4$ and Ba_2SnO_4 yields activation energies (Ea) of 0.20 eV and 0.018 eV, respectively, with a correlation factor of 0.99

E_a = 0.20 eV is the energy required for the electron jump between FeO_6 octahedra sharing corners: $Fe_{oc}^{3+} \leftrightarrow Fe_{oc}^{4+}$ (see the structure). The ***p*** type semi conductivity is also assigned to the metal insertion with a weak hole mobility ($\mu = 8.91\times10^{-13}$ $cm^2\ V^{-1}\ s^{-1}$) in a narrow valence band deriving from t_{2g} band (~ 2 eV) **[19, 20]**.

While E_a = 0.018 eV characterizes a classical semiconductor where the electron hopping occurs between mixed valences of $Sn^{4+/2+}$in octahedra sharing common corners in the perovskite structure.

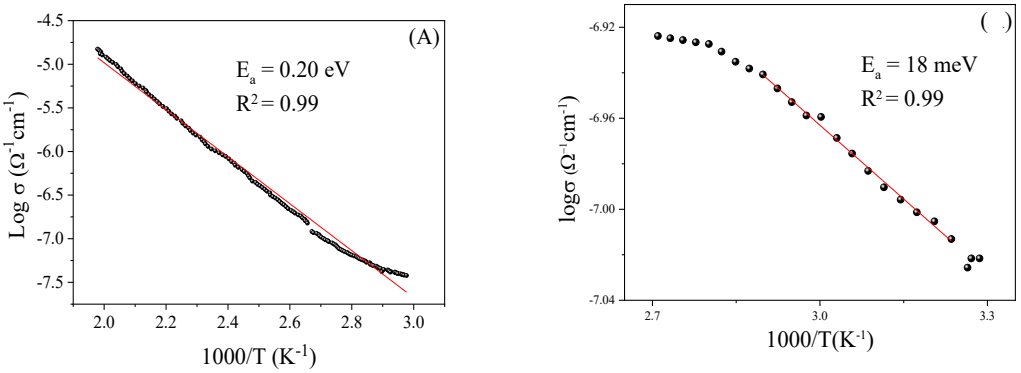

Figure IV-A-7. (A) Variation of electrical conductivity Log σ as a function of 1000/T for $CuFe_2O_4$.

(B) Variation of electrical conductivity Log σ as a function of 1000/T for Ba_2SnO_4.

IV-A.6.Electrochemical properties

IV-A.6.1. Determining the Von potential of $CuFe_2O_4$ and Ba_2SnO_4

The photo-electrochemistry analysis is crucial to elaborate a potential diagram of the interface $CuFe_2O_4$/solution and has not been investigated in detail. The cyclic voltammetry (Fig. IV.A.8A) reveals a reduction peak $Fe^{3+/2+}$ at ~ -0.4 V, while in, a cathodic peak oxidation $Fe^{2+/3+}$ (0.71 V) is observed in the back scan. The anodic and cathodic areas ratio is different from unity, indicating an irreversible internal process, confirmed by the large difference (~ 1V) of potential compared to (0.06/n), *n* is the number of exchanged electrons. Beyond ~ -1.3 V, the increased current in the cathodic branch with a low over-voltage is assigned to H_2 release and this shows that $CuFe_2O_4$ can be used ad H_2-electrode under visible light irradiation. On the other hand, the peak of H_2O oxidation does not appear, due to the high O_2 over voltage. The semi-logarithmic graph (Fig. 6B Insert) provides a potential (-375 mV), a polarization resistance (1.18 kΩ cm^2), and a small exchange current density (17 µA cm^{-2}), indicating an electro-stability of $CuFe_2O_4$ in the working solution (Table IV.A.1) **[21, 22]**.

Table IV-A-1. Electro kinetic parameters of $CuFe_2O_4$ in Rh B solution (pH ~ 6; 20 mg/L).

Corrosion potential (mV)	**Polarization resistance (kΩ cm^2)**	**J (µA/cm^2)**	**Beta a (mV)**	**Beta c (mV)**	**Corrosion rate (µm/Year)**	**Correlation coefficient R^2**
511	-1.18	16.95	124.1	-121.6	198.2	0.999

The intensity-potential J(V) characteristic (Fig. IV.A.8B) shows a good electrochemical stability with a small current (< 0.2 mA cm^{-2}) and a large O_2 overvoltage. The current is due to the

thermal excitation across the activation energy in conformity with a wide space charge region. The electrochemical stability is supported by the electrokinetic parameters deduced from the semilogarithmic plot log J-V (Fig. IV.A.8B. Inset). Further support of the electron localization is brought by the anodic peak at −0.24 V corresponding to the electrochemical couple $Sn^{4+/2+}$, a value close to the standard potential of the $Sn^{4+/2+}$ couple (~ −0.1 V) **[23]**. On the reverse scan, the cathodic peak at −0.92 V is attributed to reduction of Sn^{4+}. The separation peak at ~0.7 V is large compared to the internal redox process (0.06/*n*), *n* being the number of exchanged electrons. In addition, the ratio of anodic and cathodic current areas (~5) is different from unity indicating an irreversible internal process. Below ~ −1 V, the current shoots up considerably due to hydrogen evolution and this shows that Ba_2SnO_4 can be used ad H_2-electrode upon UV irradiation. The semi logarithmic plot (Fig. IV.A.8B. Inset), give the electro-kinetic parameters: a polarization resistance of 2.1 kΩ cm^2, a corrosion potential of -780 mV and a small exchange current density (105 µA cm^{-2}) are good signs of Ba_2SnO_4 stability (Table IV.A.2).

Table IV-A-2. Electro kinetic parameters of corrosion behavior of Ba_2SnO_4 in Rhodamine B solution (pH ~ 6, 20 mg/L).

Corrosion potential (mV/ECS)	**Polarization resistance (KΩ/Cm²)**	**J (µA/cm²)**	**β_a (mV/dec)**	**β_c (mV/dec)**	**Corrosion rate(µm/Year)**	**Coefficient**
-785 mV	2.1	105	1202	-1202	55.27	1

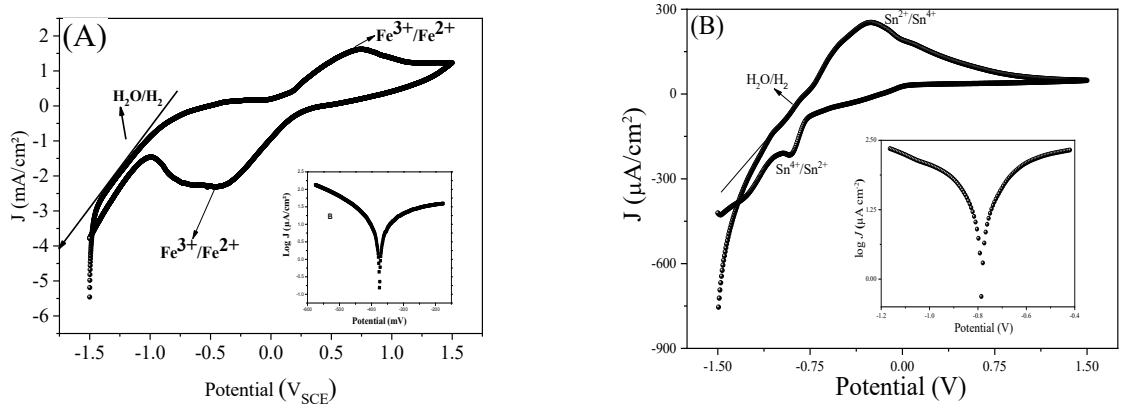

Figure IV-A-8. (A) Cyclic voltammetry J(E) curve of $CuFe_2O_4$ electrode in Rh B solution (C_o = 20 mg/L) + Na_2SO_4 as supporting electrolyte Scan rate 10 mV s^{-1}. Inset: the semi-logarithmic plot. (B) Cyclic voltammetry J(E) curve of Ba_2SnO_4 electrode in Rh B solution (C_o = 20 mg/L) + NaCl as supporting electrolyte Scan rate 10 mV s^{-1}. Inset: the semi-logarithmic plot.

IV-A.6.2. Capacitance measurements of $CuFe_2O_4$ and Ba_2SnO_4

Figure IV.A.9 shows semiconductor capacitance measurements (CSC) carried out in an acidic environment (pH ~ 5.5) on $CuFe_2O_4$ and Ba_2SnO_4. The plot of C^{-2} versus potential (Figure IV.A.9) allows the flat-band potential (Ebp= -0.56 and -0.84 V respectively) to be deduced from the extrapolation of the linear part. The flat-band potential (Ebp) is related to the capacitance (C) by the Mott-Schottky relation:

$$\frac{1}{C_{SC}^2} = \pm\left[\frac{2}{e\varepsilon\varepsilon_o N_D S^2}\right]\left(E - E_{bp} - k\frac{T}{e}\right) \qquad (IV.A.4)$$

C_{SC} is the capacitance; N_D the density of majority carriers; ε et ε_o the permittivities of the material and vacuum respectively; S electrode surface and kT thermal energy (~ 0.025 eV at 25 °C).

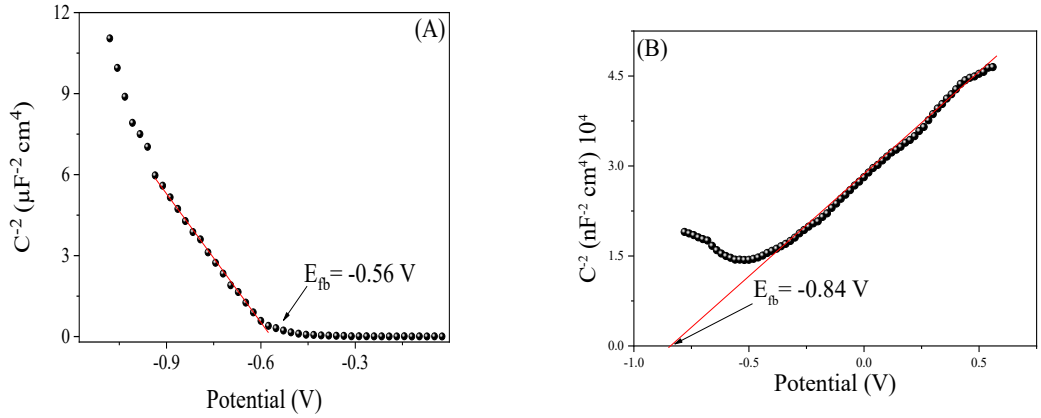

Figure IV-A-9. The Mott-Schottky characteristic curve (C^{-2} –E) of (A) $CuFe_2O_4$ (B) Ba_2SnO_4 at a frequency of 10 kHz.

The positive slope observed in the graph (C^{-2} - E) (Fig. IV.A.9B) indicates n-type conduction for Ba_2SnO_4, with the negative sign confirming that electrons are the majority carriers. Conversely, the negative slope seen for $CuFe_2O_4$ (Fig. IV.A.9A) is characteristic of p-type conduction.

IV-A.6.3. Energy diagram of $CuFe_2O_4$ and Ba_2SnO_4

Determination of the optical, electrical and photoelectrochemical characteristics enables the valence band BV and the conduction band BC of the semiconductors to be located on an energy diagram (Figure. IV.A.10) in relation to the saturated calomel electrode (ECS) and thus to predict the photo-catalytic reactions likely to occur at the interface:

$$E_{BC}(V) = V_{fb} - E_\sigma \qquad (IV.A.5)$$

$$E_{BV}(V) = V_{fb} - E_\sigma + E_g \qquad (IV.A.6)$$

ΔE_{σ} is the activation energy calculated from the conductivity measurement (σ) and corresponds to the separation between the Fermi level and the conduction band. The conduction (BC) and valence (BV) bands are calculated from equations A-7 and A-8 (Figure IV-12).

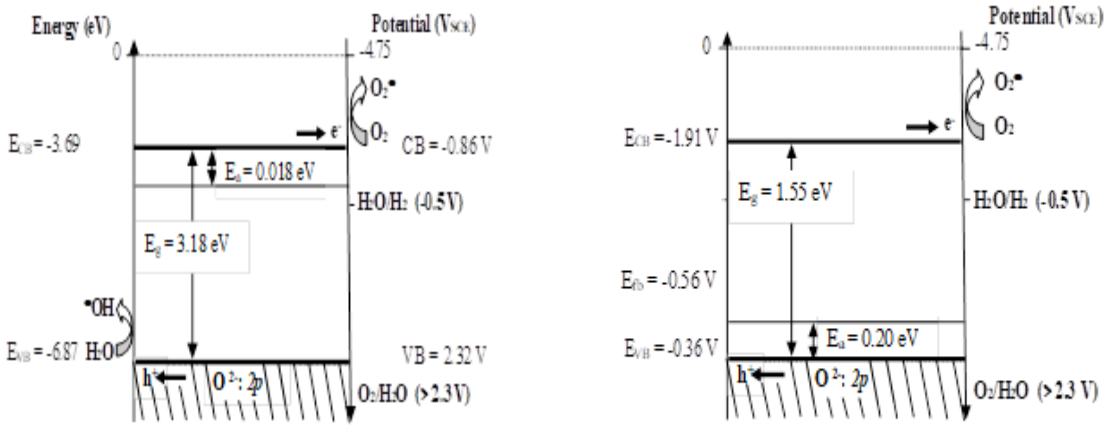

Figure IV-A-10. (A) The energy diagram of $CuFe_2O_4$ in Rhodamine B / Na_2SO_4 solution/ (B) The energy diagram of Ba_2SnO_4 in Rhodamine B solution.

IV-B. Electro-catalysis and photocatalysis of Rh B by CuFe2O4 and Ba2SnO4

In this section we will present the main results of our experiments for the degradation and mineralisation of Rhodamine B. To demonstrate the efficiency of our semiconductors, the abatement was monitored by UV-Visible spectroscopy, COD

IV-B.1. Electro-catalysis of Rh B by $CuFe_2O_4$ and Ba_2SnO_4

Three materials (Ti/Pt, $CuFe_2O_4$ and Ba_2SnO_4), arranged in different anode/cathode pairs, were tested to determine the electrode pair giving the best performance for the process used. The solution to be treated consisted of 20 mg/L rhodamine B and 3.5 g/L NaCl and Na_2SO_4; the current was set at 150 mA, the initial pH at 5.5 (natural pH of the solution) and the treatment time at 3 h **[24]**. The experimental set-up is shown in (Figure IV.B.1)

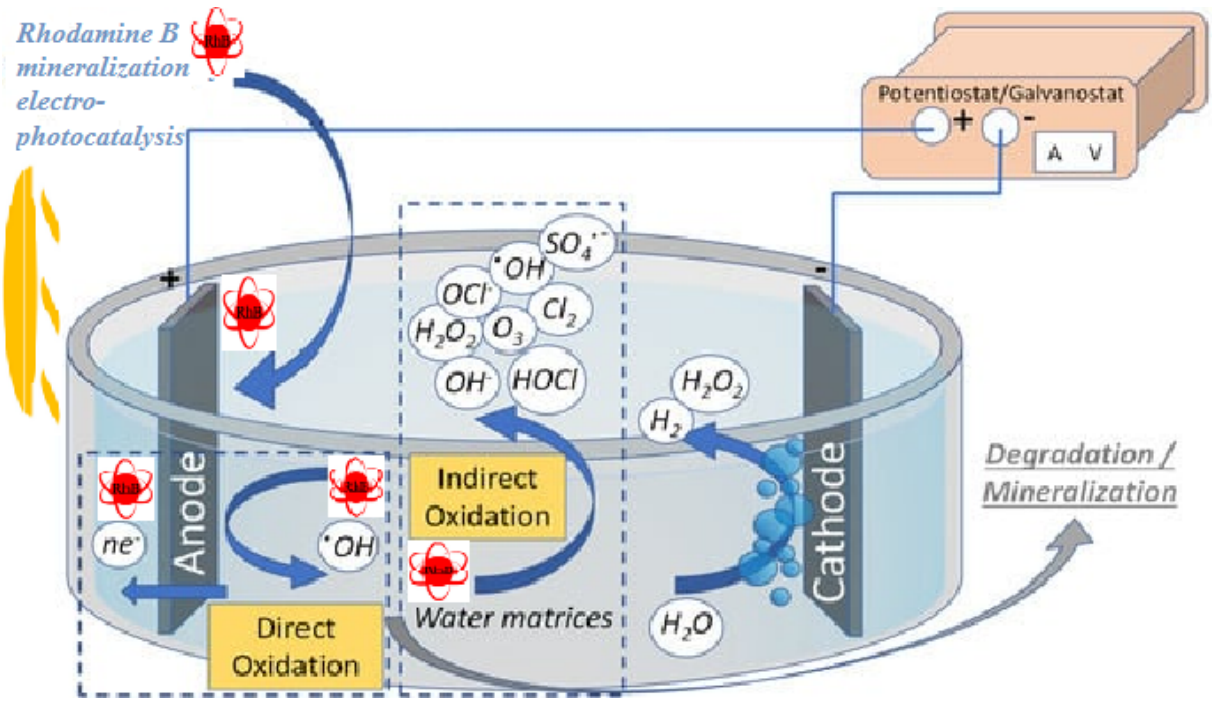

Figure IV-B-1 ; Experimental device of direct and indirect oxidation process for the degradation of Rhodamine B by electrophotocatalysis under solar light in NaCl and Na_2SO_4solutions (3.5 g/L), [RhB]= 20 mg/L, I= 150 mA (Ba_2SnO_4/Ti-Pt) and (Cu_2FeO_4/Ti-Pt).

Due to the high O_2 over-potential on the oxides, oxidation of the organic dye occurs by free radicals on anodically polarized Ba_2SnO_4 and $CuFe_2O_4$ **[25, 26]**:

$$M + H_2O \xrightarrow{electric\ current} M\,(OH^{\bullet})_{ads} + h^+ + e^- \qquad (IV.B.1)$$

Rh B is a very stable molecule with low photolysis under sunlight, not exceeding 3%, due to its mesomeric structure; therefore, it requires powerful radicals for degradation. In this context, electro-generated radicals M (•OH) adsorbed on Ba_2SnO4 and $CuFe_2O_4$ can lead to high mineralization, with conversion rates of 66% and 56%, respectively, under a current of 150 mA (Fig. IV.B.1), **[27].**

IV-B.2. Electro-photocatalysis of Rh B by $CuFe_2O_4$ and Ba_2SnO_4 under solar light

Photo-electrochemical conversion requires moderate conductivity with expansion of the depletion layer, receiving more incident photons **[28]**. The electrons come from two sources namely the exciting photons and electric current, the latter accelerates the electro-activity of the perovskite and the spinel.

The electrons in Ba_2SnO_4-$_{CB}$ and in $CuFe_2O_4$-$_{CB}$ reduce O_2 and H_2O respectively to $O_2^{\bullet-}$ and H_2O_2. The latter acts as an electron acceptor, to generate one of the most powerful radicals, namely $^{\bullet}OH$, for the oxidation of Rh B, covalently linked to Ba_2SnO_4 according to the following sequences **[29,30]**:

$$O_{2\,ads} + e^- \rightarrow O_2^{\bullet-} \quad \text{(IV.B.2)}$$

$$2\,O_{2\,ads} + 2\,H_3O^+ + 2\,e^- \rightarrow H_2O_2 + O_2 + 2\,H_2O \quad \text{(IV.B.3)}$$

$$H_2O_2 + e^- \rightarrow {}^{\bullet}OH + OH^- \quad \text{(IV.B.4)}$$

$$2\,H_2O + 2\,e^- \rightarrow H_2 + 2\,OH^- \quad \text{(IV.B.5)}$$

$$\text{Rh B} + O_2^{\bullet-} \rightarrow \text{Mineralization} \quad \text{(IV.B.6)}$$

And covalently linked to $CuFe_2O_4$ according to the following sequences **[31, 32]**:

$$O_{2\,ads} + e^- \xrightarrow{electric\ current + h\nu} O_2^{\bullet-} \quad \text{(IV.B.7)}$$

$$2\,O_{2\,ads} + 2\,H_3O^+ + 2\,e^- \rightarrow H_2O_2 + O_2 + 2\,H_2O \quad \text{(IV.B.8)}$$

$$H_2O_2 + e^- \rightarrow {}^{\bullet}OH + OH^- \quad \text{(IV.B.9)}$$

$$2\,H_2O + 2\,e^- \rightarrow H_2 + 2\,OH^- \quad \text{(IV.B.10)}$$

$$\text{Rh B} + O_2^{\bullet-} + {}^{\bullet}OH \rightarrow \text{Mineralization} \quad \text{(IV.B.11)}$$

The kinetics of Rh B oxidation by $CuFe_2O_4$ follows a pseudo-first-order model with a rate constant of 1.2×10^{-2} min^{-1} ($t_{1/2}$ = 57 min), which is approximately 1.4 times greater than the rate constant obtained by electrocatalysis (9×10^{-3} min^{-1}, $t_{1/2}$ = 111 min; Fig. IV.B.2C) **[33, 34]**. In contrast,

the kinetics of Rh B oxidation by Ba_2SnO_4 also follows a pseudo-first-order model with a rate constant of 1.96×10^{-2} min^{-1} ($t_{1/2}$ = 35 min), which is about 1.5 times greater than the rate constant obtained by electrocatalysis (1.31×10^{-2} min^{-1}, $t_{1/2}$ = 52 min ;Fig. IV.B.3C) **[35]**. These results show that Ba_2SnO_4 degrades Rh B more effectively than $CuFe_2O_4$ in electrophotocatalysis.

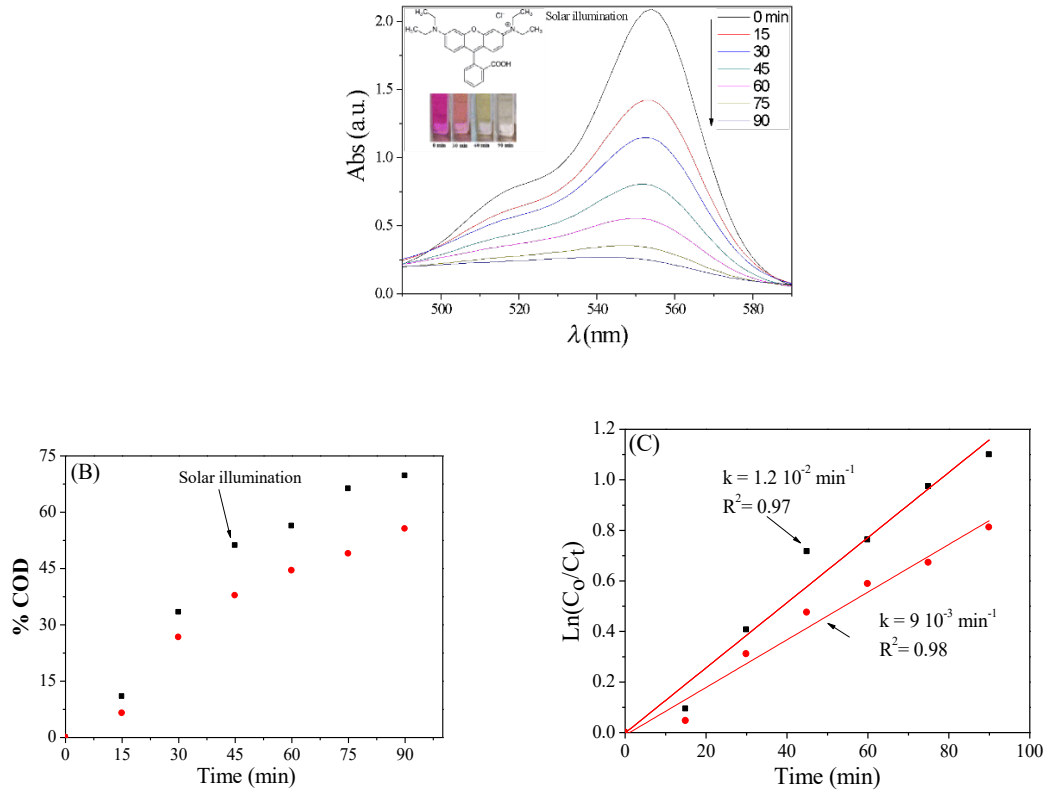

Figure IV-B-2 ; (A) UV-Visible spectra of Rh B removal over elimination time. (B) The COD kinetic analysis of Rh B mineralization by electro-catalysis (•), and electro-photocatalysis (▪) under solar light in Na_2SO_4 solution (3.5 g/L), [Rh B] = 20 mg/L, I = 150 mA ($CuFe_2O_4$ /Ti-Pt).

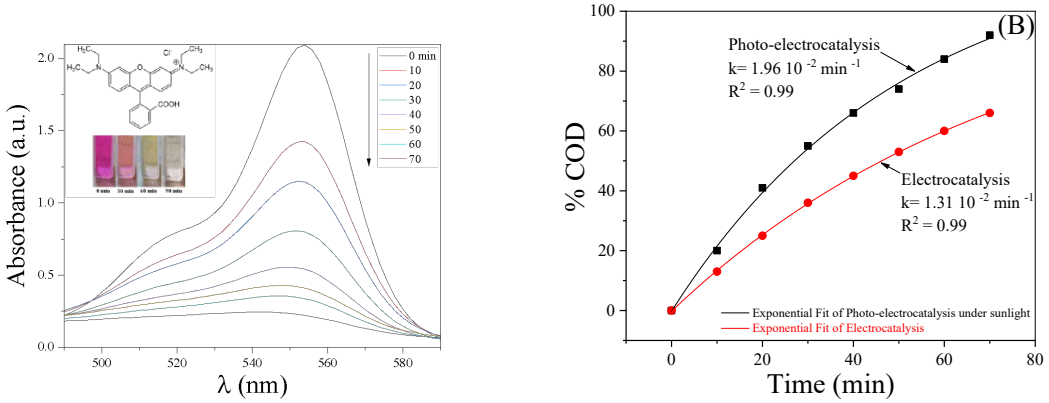

Figure IV-B-3. The COD kinetic analysis of Rh B degradation by electrocatalysis (•), and photo-electrocatalysis (▪) under solar light in NaCl solution (3.5 g/L), [Rh B] = 20 mg/L, I = 150 mA (Ba_2SnO_4 /Ti-Pt).

IV-C. Electrophotocatalysis of MO by $CuFe_2O_4$ under solar light

To monitor the elimination of methyl orange (MO) through electrophotocatalysis, we studied the effects of various factors, including new electrode materials ($CuFe_2O_4$ /Ti-Pt), current intensity, inter-electrode distance, electrolyte type and concentration, catalyst type and concentration, pollutant concentration, and oxygen bubbling. Our goal is to demonstrate the effectiveness of this process in degrading textile dyes while comparing its efficiency relative to the energy consumed. This will also facilitate subsequent modeling. We then aim to apply the optimal conditions to a real textile effluent from the (Textile-Blida plant).

IV-C.1.1. Effect of current density:

It is important to emphasise that an appropriate choice of current density in the electrochemical system can maintain current efficiency, effectively remove pollutants and minimize energy consumption **[36]**

The effect of current intensity on degradation kinetics was studied on the ($CuFe_2O_4$ /Ti-Pt) electrode pair for current intensities varying from 100, 300 and 500 mA, a reaction volume of 250ml, at concentrations of 10 mg/L Methylorange and 3.5 g/l Na_2SO_4 , natural pH of the solution (pH=7) and treatment time at 2 h.

The results obtained are shown in Figures (**IV.C.1, IV.C.2, IV.C.3**)

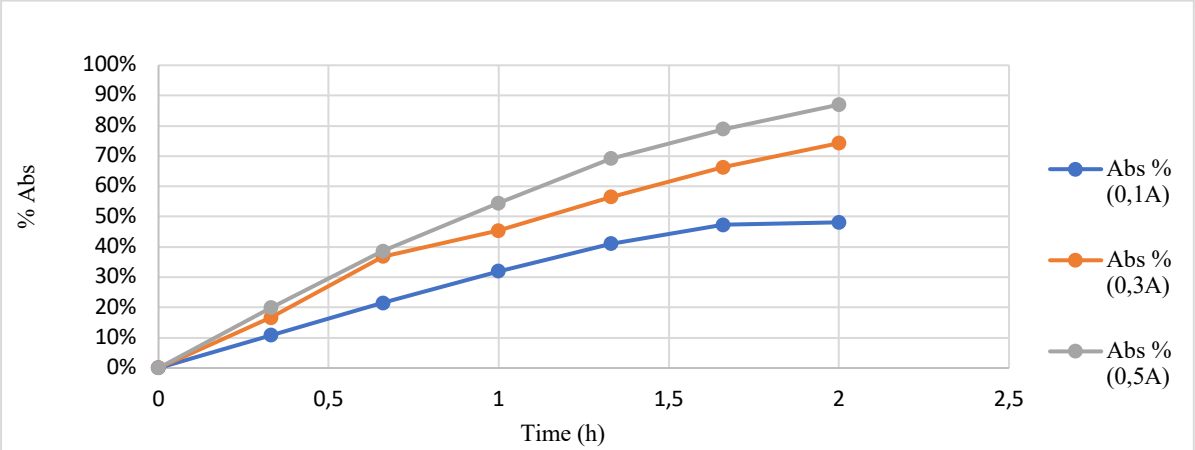

Figure IV-C-1. Effect of Current Intensity on degradationof Methyl Orange ([MO]= 10mg/L, [Na_2SO_4]= 3.5g/l, I=[0.1, 0.3, 0.5]A, pH 7, d=1 cm).

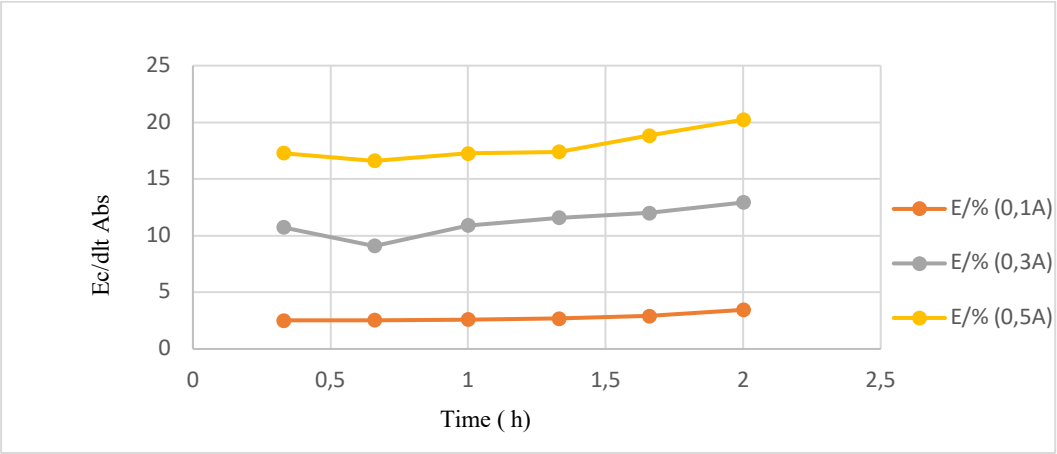

Figure IV-C-2. Effect of Current Intensity on energy consumption of Methyl Orange ([MO]= 10mg/L, [Na_2SO_4]= 3.5g/l, I=[0.1, 0.3, 0.5]A, pH 7, d=1 cm).

The results in Figure IV.C.1 and IV.C.2 show that for a current intensity equal to 0.3 A and a time t = 120 min, the rate of degradation is a maximum of 74% with a relatively low EC (12.92 Wh).

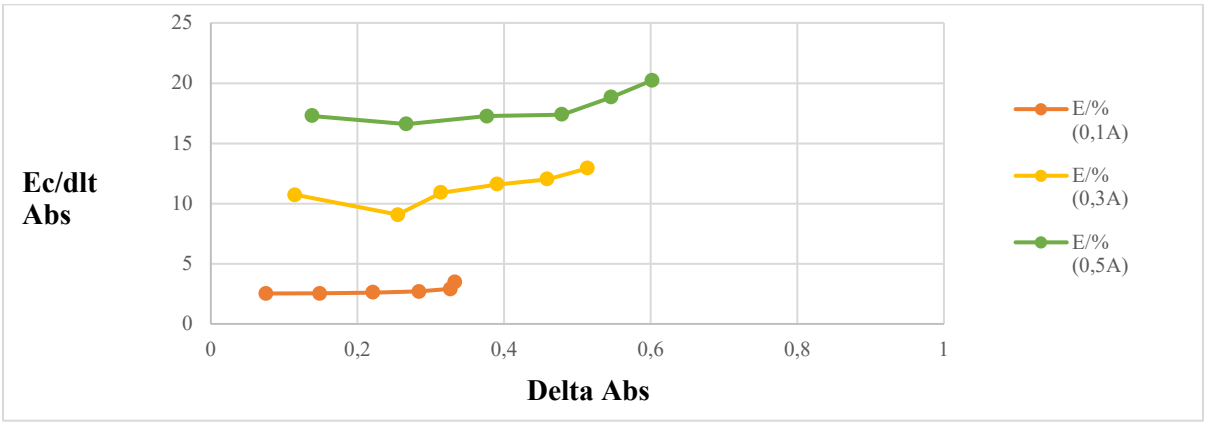

Figure IV-C-3. Effect of Current Intensity on the Energy–Absorbance Correlation of Methylorange ([MO]= 10 mg/L, [Na_2SO_4]= 3.5 g/l, I=0.3A, pH 7, d=1cm).

From the results recorded during this series of treatments, it can be seen that an increase in current intensity from 100 to 500 mA is followed by an increase in the energy consumed by the treatment (from 4.62 Wh to 195.55 Wh) and in the absorbance gradient (0.327 nm to 0.602 nm), the latter being proportional to the overproduction of essentially -OH radicals **[37]**. The best conditions correspond to the highest value of degradation yield and closely to the minimum energy consumed, as well as the time required to achieve this yield.

However, it appears that increasing the absorbance gradient from 300 mA to 500 mA leads to an insignificant increase in the 0.1 nm absorbance gradient for a fourfold increase in energy consumption (53.93 to 195.55). Also, as the current intensity increases, the Joule effect losses are greater. For this reason, 300 mA is considered to be the optimum value for the current intensity. The absorbance spectrum is shown in Figure IV.C.3.

IV-C.1.2. Effect of the electrolyte

The electrical conductivity of water is a factor that influences the quality of electrolytic treatment of the effluent to be treated since it facilitates the passage of electric current and ensures good transfer of ions through the solution (Nidheesh et al., 2012) **[38]**. In the present study, we examined 3 types of electrolytes with the same Na^+ cation, namely, NaCl, Na_2SO_4, $NaNO_3$ at concentrations of 3.5g/l, a reaction volume of 250ml, at concentrations of 10 mg/L Methylorange, previously optimised current intensity and inter-electrode distance, natural pH of the solution (pH 7) and treatment time of 2 h.

The results are shown in Figures (IV.C.4, IV.C.5, IV.C.6) :

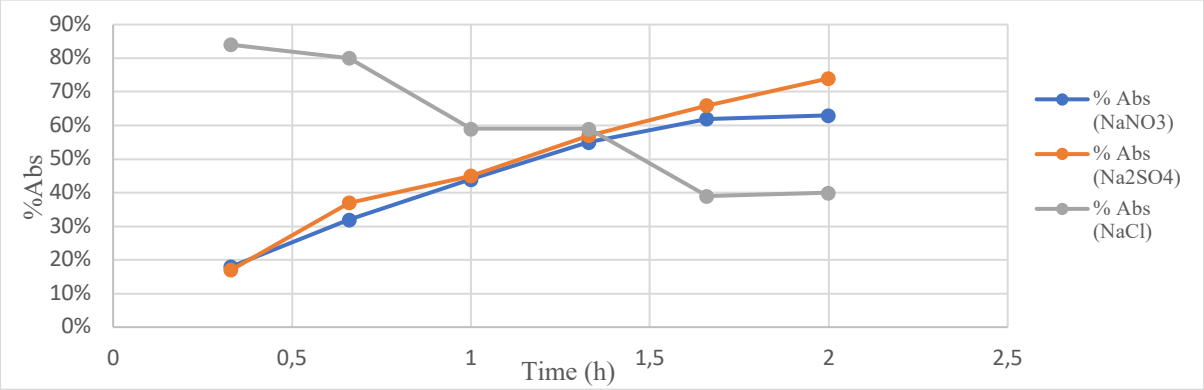

Figure IV-C-4. Effect of electrolyte on degradation of Methyl Orange ([MO]= 10 mg/L, [Na_2SO_4/$NaNO_3$/NaCl]=3.5 g/l, I=0.3A, pH=7, d=1 cm).

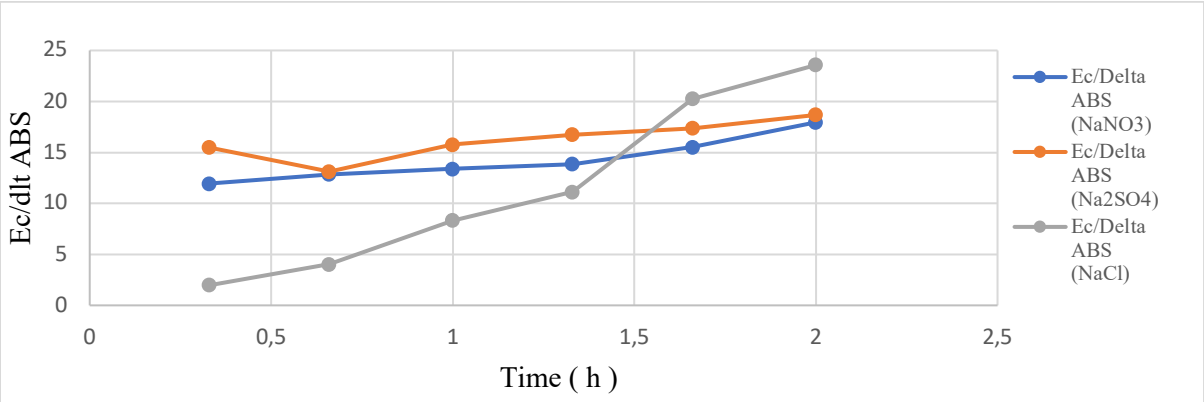

Figure IV-C-5. Effect of electrolyte on energy consumption of Methyl Orange ([MO]= 10 mg/L, [Na_2SO_4/$NaNO_3$/NaCl]=3,5 g/l, I=0.3A, pH=7, d=1 cm).

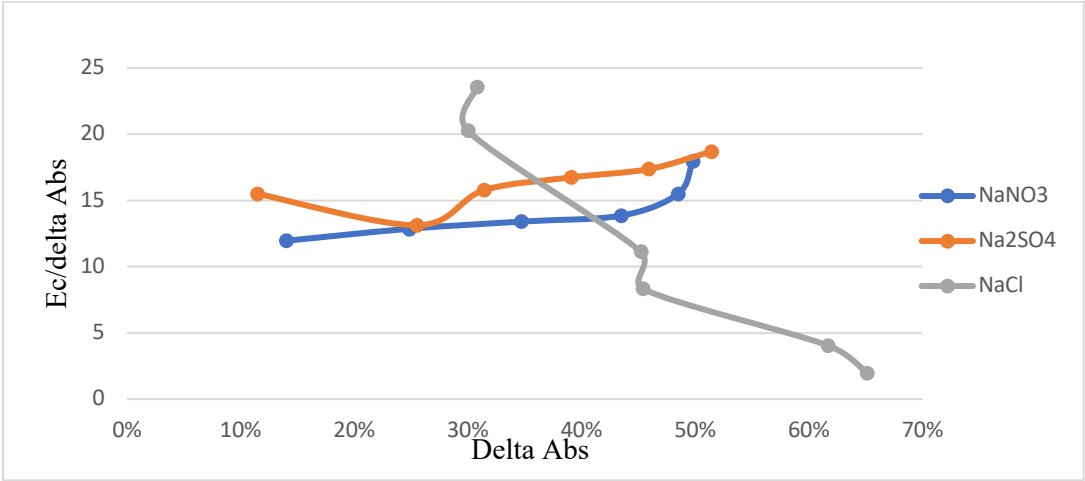

Figure IV-C-6. Effect of electrolyte on the Energy–Absorbance Correlation of Methylorange ([MO]= 10 mg/L, [Na_2SO_4/$NaNO_3$/NaCl]=3.5 g/l, I=0.3A, pH=7, d=1 cm).

It can be seen from Figures IV.C. (4,5,6) that :

1- For the NaCl electrolyte, there is total degradation of the methylorange at 20min of treatment (Figure IV.C.7) with formation of an oxidation by-product following the A(λ) spectrum at λ=293nm.

2- The Na_2SO_4 process consumes less energy than $NaNO_3$.

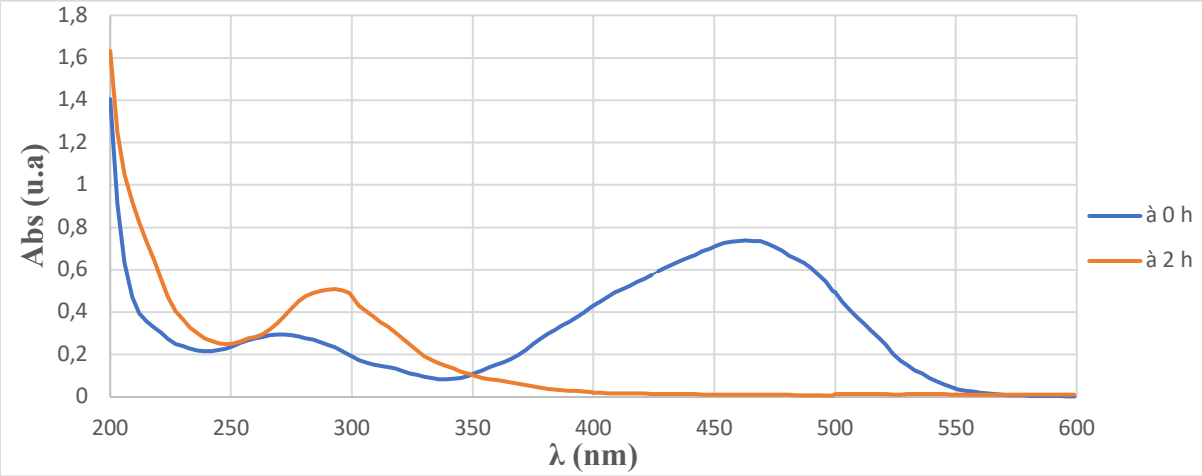

Figure IV-C-7. Absorbance spectrum of methyl orange degradation with NaCl as electrolyte ([MO]= 10 mg/L, [NaCl]= 3.5 g/l, I=0.3A, pH 7, d=1 cm).

From the results recorded during this series of treatments, we can see that for NaCl we have 100% degradation, but the formation of another product (Figure IV.C.7), which leads us to eliminate it from the choice of electrolyte. For the other two products, we can see that less energy is consumed with Na_2SO_4 than with $NaNO_3$.

Figures (IV.C.4, IV.C.6) show a greater efficiency of Na_2SO_4 compared with NaCl and

$NaNO_3$. This result is in agreement with those observed by Da Silva et al **[39]**, on the mineralisation of the antibiotic norfloxacin (NOR) by elctrocatalysis oxidation using a BDD electrode deposited on p-type Si single crystal (p-Si/BDD). With the use of Na_2SO_4, the increase in process efficiency could be explained by additional degradation of NOR by the $S_2O_8^{2-}$ species formed in solution. Indeed, SO_4^{2-} ions are easily oxidised at the anode to form persulphate ions, equation (IV.C.6), and due to their high reactivity, they could react with organic compounds and thus contribute to their degradation **[40]**. Furthermore, according to Chachou et al **[41]**, compared with other anions, the effectiveness of Na_2SO_4 is due to the high conductivity of the sulphate ion (SO_4^{2-}), which allows better charge transfer. Consequently, Na_2SO_4 was chosen as the optimum electrolyte for the rest of the experimental study

The optimum absorbance spectrum is shown in Figure IV.C.8:

$$2HSO_4^- \rightarrow S_2O_8^{2-} + 2H^+ + 2e^- \quad \text{(IV.C.1)}$$

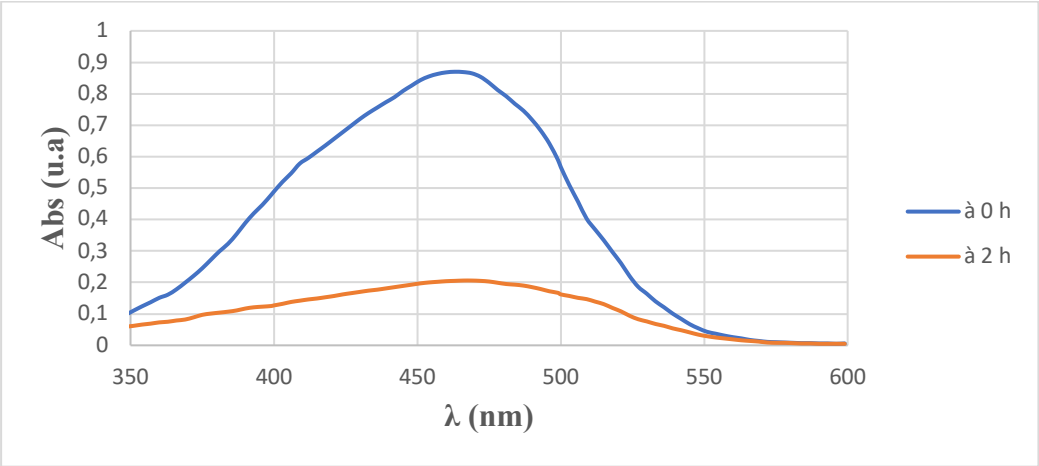

Figure IV-C-8. Absorbance spectrum of methyl orange degradation with Na_2SO_4 as electrolyte [MO]= 10 mg/L, [Na_2SO_4] =3.5 g/l, I=0.3A, pH 7, d=1 Cm

IV-C.2. Effect of electrolyte concentration

In electrochemical water treatment processes, studies on electrolyte concentrations are generally used to improve the conductivity of the solution and hence reduce energy consumption. In this context, our study is based on concentrations varying from 2 to 5g/l of our previously optimised electrolyte (Na_2SO_4), a reaction volume of 250ml, at concentrations of 10 mg/L of Methylorange, a current intensity of 0.3A and inter-electrode distance of 1cm, natural pH of the solution (pH 7) and a treatment time of 2 h.

The results obtained are shown in Figures (**IV.C.9**, **IV.C.10**, **IV.C.11**) :

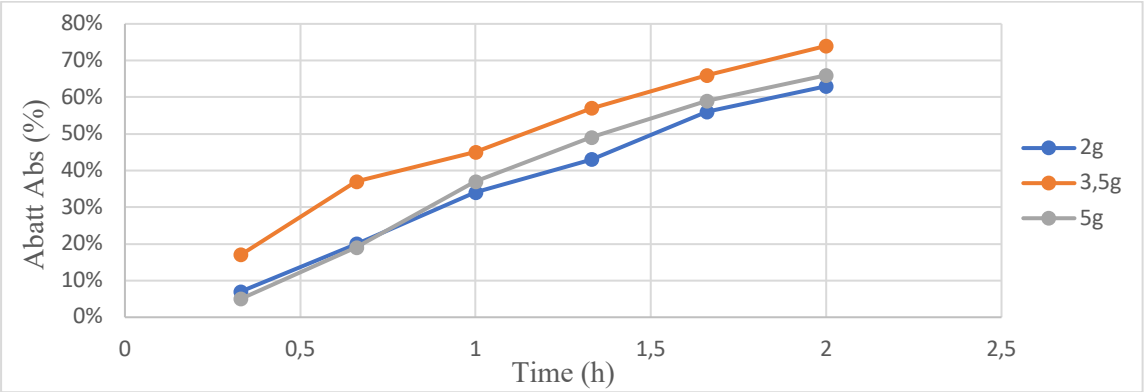

Figure IV-C-9. Effect of electrolyte concentration on energy consumption of Methylorange ([MO]=10mg/L, [Na_2SO_4] = (2, 3.5, 5) g/l, I=0.3A, pH 7, d=1 cm).

The results recorded in figures (IV.C.9, IV.C.10, IV.C.11) show that the electrochemical treatment using a concentration of 3.5 g/l of Na_2SO_4 has the best degradation rate of 74%, with a low energy of 15.49 Wh compared with the other concentrations.

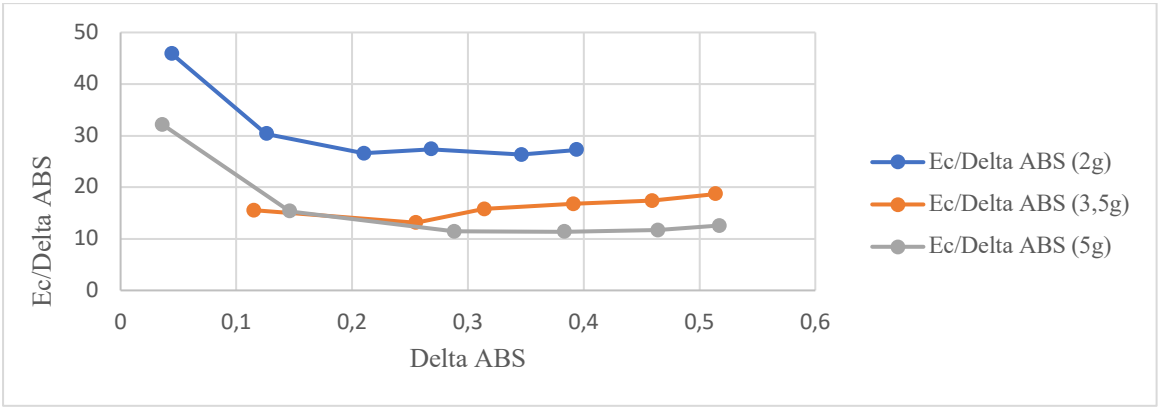

Figure IV-C-10. Effect of electrolyte concentration on the Energy–Absorbance Correlation of Methylorange ([MO]= 10 mg/L, [Na_2SO_4]= 3.5 g/l, I=0.3A, pH 7, d=1cm).

According to the results obtained, between 2 and 3.5 g/L, the EC decreases significantly from 45.9 to 15.49 Wh, with a significant increase in the degradation rate from 63% to 74%. On the other hand, for salt concentrations between 3.5 and 5 g/L, the decrease in EC is not very significant, from 18.67 to 12.53 Wh, but the degradation efficiency decreases. This can be explained by the decrease in the electrical resistance of the medium, which reduces the cell voltage and therefore the decrease in energy consumption. However, the increase in electrolyte concentration from 3.5 to 5 g/L, does not justify the additional cost of salt.

Therefore, for the remainder of the study, 3.5g/l Na_2SO_4 was chosen as the optimum electrolyte concentration (Figure IV.C.11)

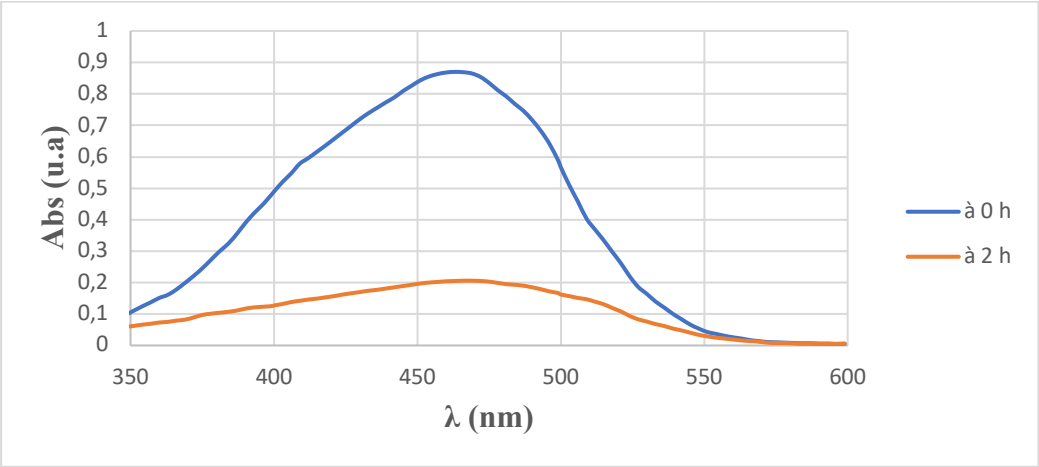

Figure IV-C-11. Absorbance spectrum of methyl orange degradation with (3.5) g/L Na_2SO_4, [MO]=10mg/L, [Na_2SO_4]= 3.5 g/l, I=0.3A, pH 7, d=1 cm).

IV-C.3. Effect of pH

Since the chemical structures of pollutants can be influenced by the pH of the solution, the latter can contribute to the effectiveness of electrochemical treatments **[42]**. Several researchers have studied the influence of solution pH on electrochemical processes. However, given the diversity of electrode materials studied and the different structures of organic pollutants, their results are varied and even contradictory, with some researchers stating that the process is more favourable in acidic environments **[43,44]**, while others **[45,46]** find that process efficiency is optimal in alkaline environments.

To study the effect of pH on the efficiency of methyl orange degradation, a series of experiments was carried out from pH 3 to pH 11. We worked with the parameters we had previously optimised, with 2 hours of electrolytic treatment, the pair of electrodes ($CuFe_2O_4$ /Ti-Pt), the current intensity at 300mA, the inter-electrode distance at 1cm, electrolyte Na_2SO_4 at 3.5 g/l, methylorange concentration 10 ppm. The desired pH was adjusted using H_2SO_4 or NaOH.

The results obtained are shown in Figures (IV.C.12, IV.C.13, IV.C.14):

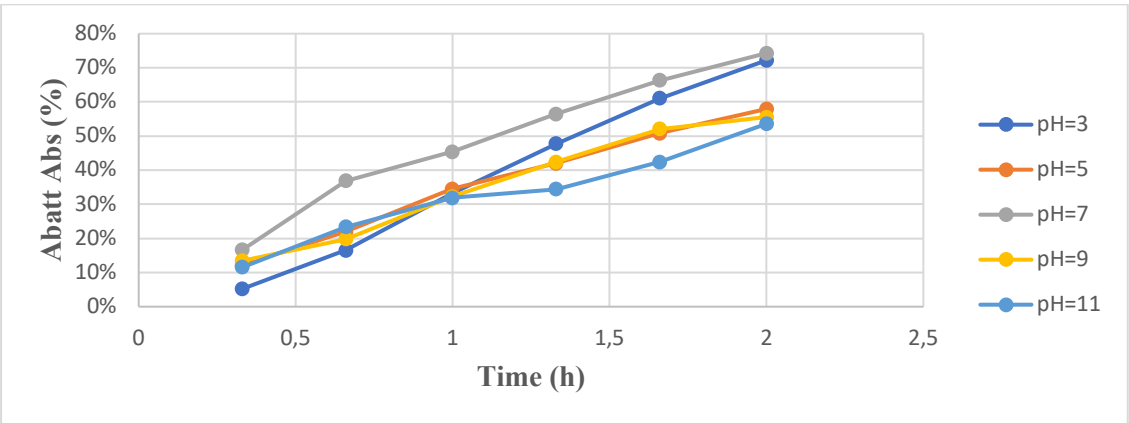

Figure IV-C-12. Effect of pH on degradation of Methyl Orange ([MO]= 10mg/L, [Na_2SO_4] = 3.5 g/l, I=0.3A, pH (3, 5, 7, 9,11), d=1 cm).

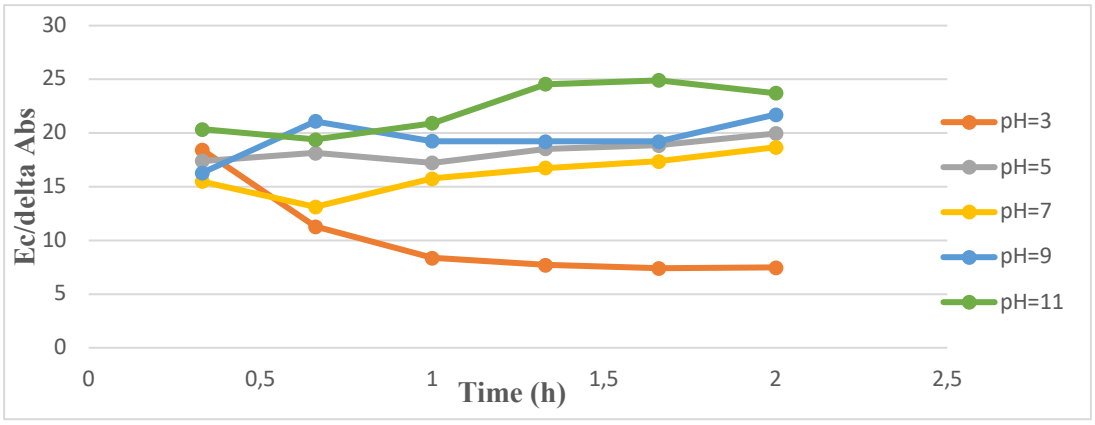

Figure IV-C-13. Effect of pH on energy consumption of Methylorange ([MO]= 10mg/L, [Na_2SO_4] = 3.5 g/l, I=0.3A, pH (3, 5, 7, 9,11), d=1 cm).

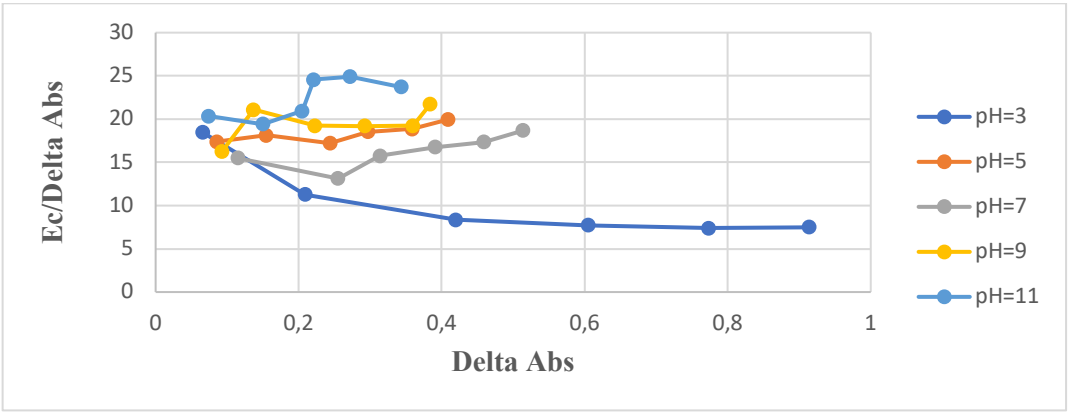

Figure IV-C-14. Effect of pH on the Energy–Absorbance Correlation of Methylorange ([MO]= 10mg/L, [Na_2SO_4] = 3.5 g/l, I=0.3A, pH (3, 5, 7, 9,11), d=1cm).

The results shown in figures (IV.C.12, IV.C.13, IV.C.14) show that:

-For the energy consumed by the process in relation to the absorbance reduction, when the pH of the solution is equal to 3 the energy is greatest at the beginning of the treatment, then it decreases with the advancement of time.

Figure IV.C.12 shows a better efficiencý at acid (3) and neutral (7) pH, with a degradation rate of 72% and 74% respectively, but a quantity degraded twice as great for pH=3.

At alkaline pH, the degradation rates are lower, which makes anodic oxidation of the methylorange unfavorable, resulting in significant energy losses (18.67 and 23.72 Wh).

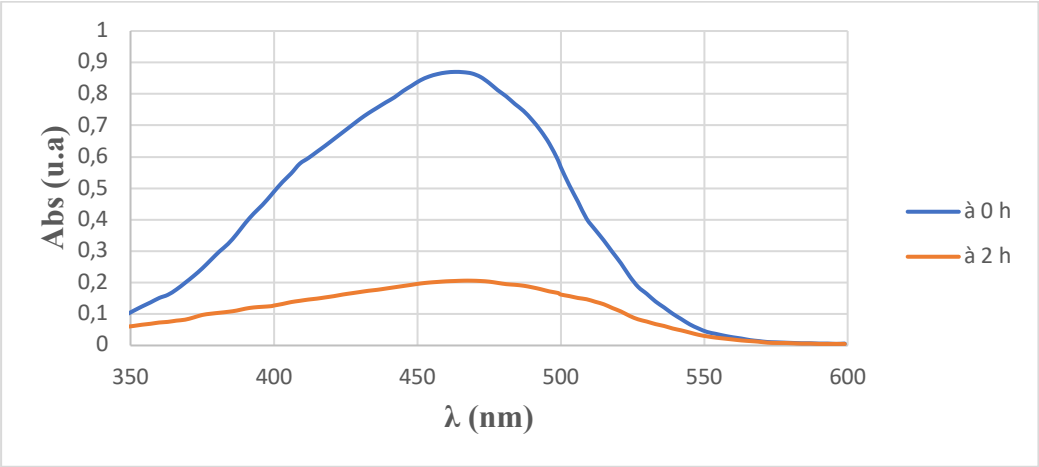

Figure IV-C-15. Absorbance spectrum of methyl orange degradation at pH =3 [MO]= 10mg/L, [Na_2SO_4]= 3.5 g/l, I=0.3A, d=1 cm).

IV-C.4. Effect of pollutant concentration

Since industrial wastewater generally involves different concentrations, it is important to study the effect of the initial dye concentration on the performance of the electrochemical oxidation process.

In this stage of the study, we will look at the influence of the pollutant concentration on the energy consumed by our treatment to achieve high abatement rates. The results obtained are presented in figures (IV.C.16, IV.C.17, IV.C.18).

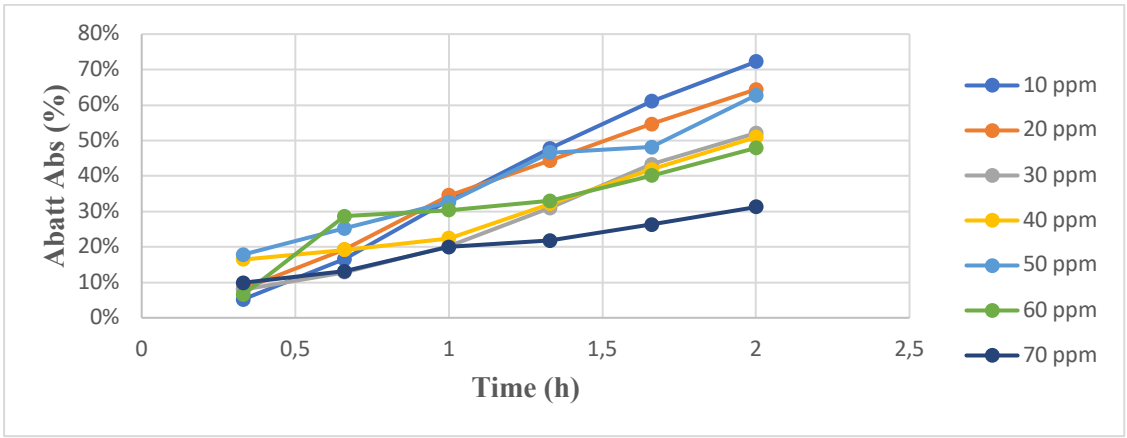

Figure IV-C-16. Effect of poluttant concentration on degradation of Methylorange ([MO]= (10, 20, 30, 40, 50, 60, 70) mg/L, [Na_2SO_4]=3.5g/l, I=300 mA, pH 3, d=1 cm).

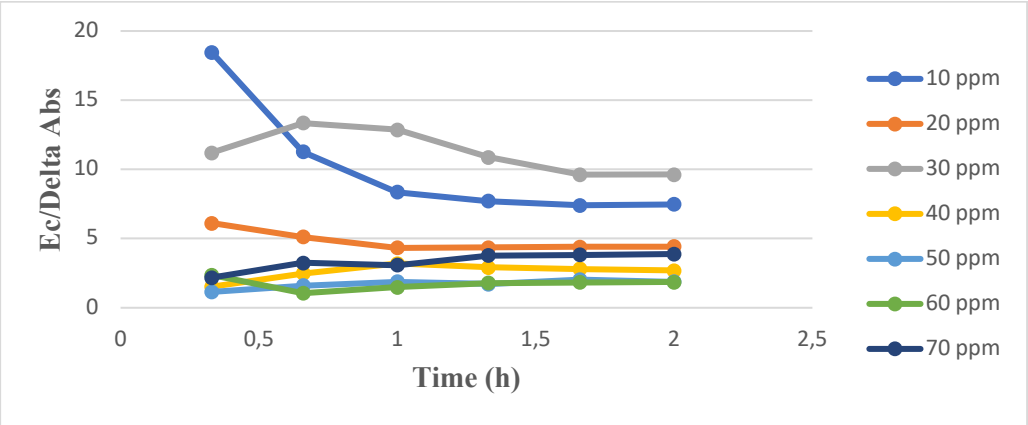

Figure IV-C-17. Effect of poluttant concentration on energy consumption of Methylorange ([MO]=(10, 20, 30, 40, 50, 60, 70) mg/L, [Na_2SO_4] =3.5g/l, I=300 mA, pH 3, d=1 cm

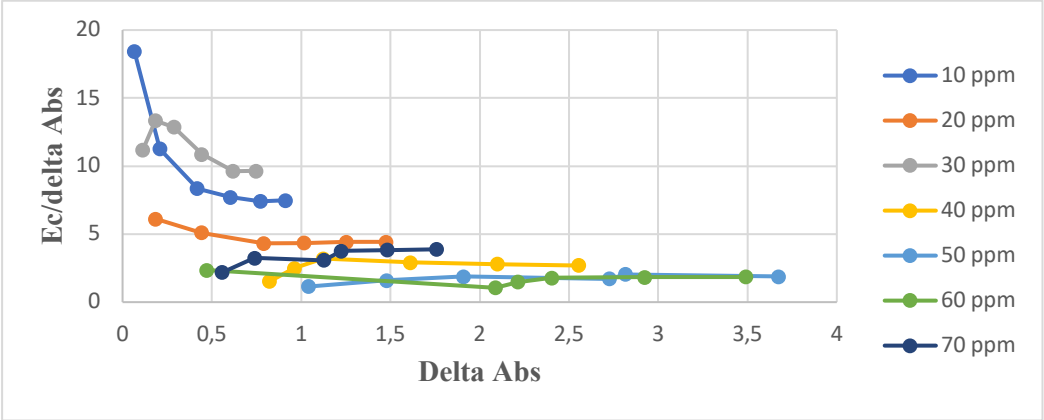

Figure IV-C-18 Effect of poluttant concentration on the Energy–Absorbance Correlation of Methylorange ([MO]=(10, 20, 30, 40, 50, 60, 70) mg/L, [Na_2SO_4]=3.5g/l, I=300 mA, pH 3, d=1 cm).

It can be seen from the results shown in figures (IV.C.16, IV.C.17, IV.C.18) that:

1- The energy consumed by the process in relation to delta abs decreases with increasing pollutant concentration up to 50ppm and 60ppm, then increases again at 70 ppm.

2- The best degradation efficiency is at 10 ppm 72%.

According to the literature, at low pollutant concentrations, the active sites required for electrolysis of the water at the anode remain free. The quantity of hydroxyl radicals produced in this case is sufficient to achieve remarkable oxidation of the pollutant **[47]**. However, in our study, high energies are consumed in low concentrations, whereas we achieved almost the same rate of degradation at 50 ppm with 7 times less energy.

Our treatment is therefore optimal at a methyl orange concentration of 50mg/l. (Figure IV.C.19).

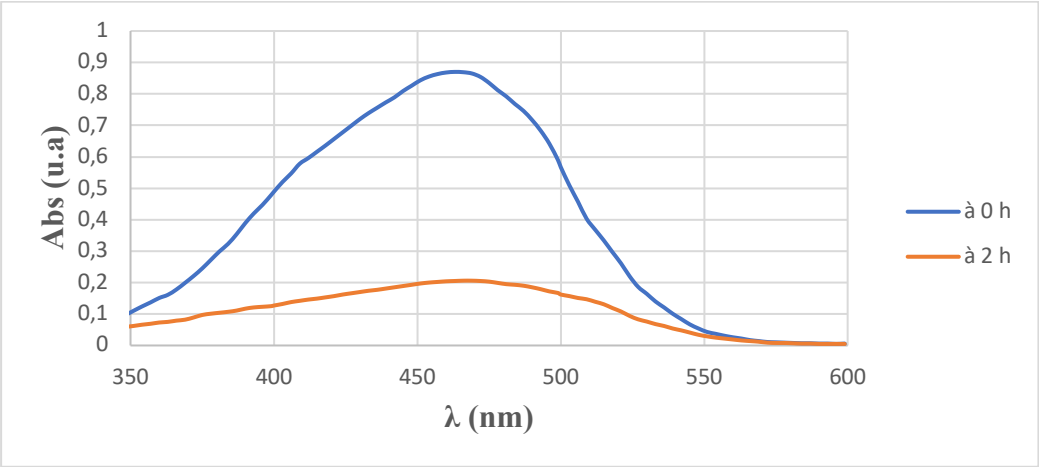

Figure IV-C-19. Absorbance spectrum of degradation at 50 ppm of methylorange [MO]= 50mg/L, [Na2SO4] = 3.5 g/l, I=0.3A, pH =3, d=1 cm).

IV-C.5. Effect of inter-electrode distance (d)

The spacing between the electrodes influences the voltage required to pass the current through the medium to be treated. A study by Feng et al **[48]** shows that the greater the distance between the electrodes, the greater the energy consumption. Modirshahla et al **[49]** and Kamaraj **[50]** have determined that the best pollutant elimination is achieved when the spacing between the electrodes is small. However, a small inter-electrode distance can greatly increase the current density and induce a short-circuit. These authors therefore prefer an electrode spacing of between 1 and 2 cm, despite an increase in ohmic resistance. To this end, we tested three inter-electrode distances: 1, 2 and 3 cm.

with a reaction volume of 250ml, at concentrations of 10 mg/L Methylorange and 3.5 g/l Na_2SO_4, a current already optimised at 300mA, at the natural pH of the solution (pH 3) and a treatment time of 2 h. The results obtained are shown in Figures (IV.C.20, IV.C.21,IV.C.22) :

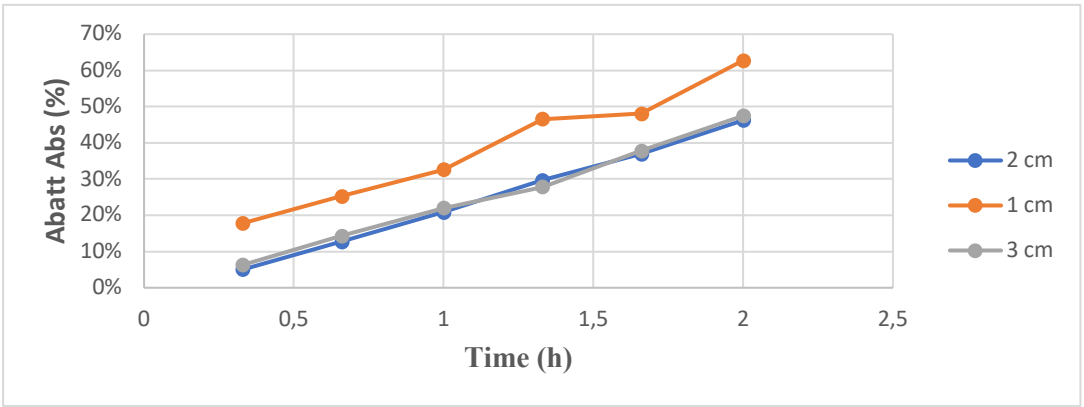

Figure IV-C-20 Effect of inter-electrode distance on degradation of Methylorange ([MO]= 50mg/L, [Na_2SO_4]= 3.5g/l, I=[0.1, 0.3, 0.5]A, pH=3, d=1 cm).

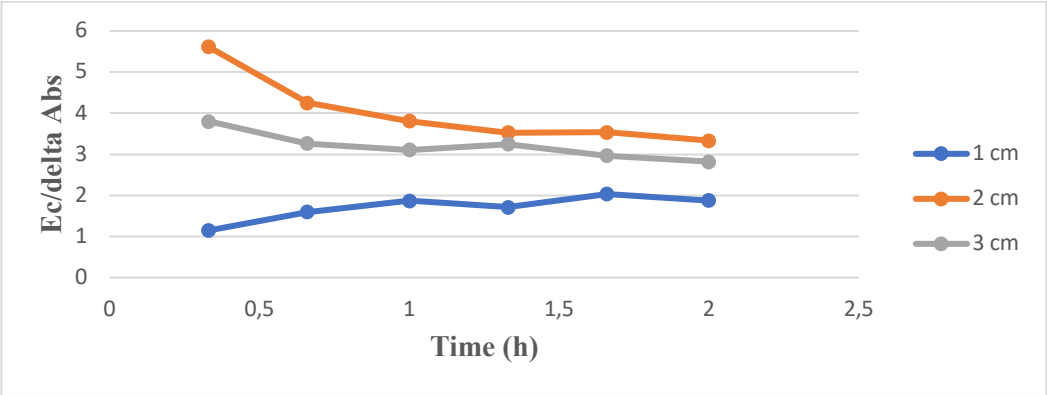

Figure IV-C-21. Effect of inter-electrode distance on energy consumption of Methylorange ([MO]= 50 mg/L, [Na_2SO_4] = 3.5 g/l, I=0.3A, pH 3, d =[1, 2, 3] cm).

We can see that the smaller the inter-electrode distance, the better the elimination of the pollutant. When this distance decreases, the resistance of the medium decreases, which results in an increase in energy yield, i.e. greater generation of radicals (-OH). When the inter-electrode distance is small, the particles and radicals have a greater chance of coming into contact (probability of pollutant-radical contact), and therefore greater efficiency in eliminating organic matter. However, it appears that going from 1 cm to 3 cm leads to a slight decrease in the absorbance gradient (≈ 0.1nm) for double the energy consumption. Also, the energy consumed increases as the inter-electrode distance increases. This increase can be explained by the same phenomena presented above, energy consumption being directly linked to the resistance of the medium, and therefore to the electrode potential. For this reason, 1 cm will be taken as the optimum inter-electrode distance (Figure IV.C.22) for the rest of the experiments.

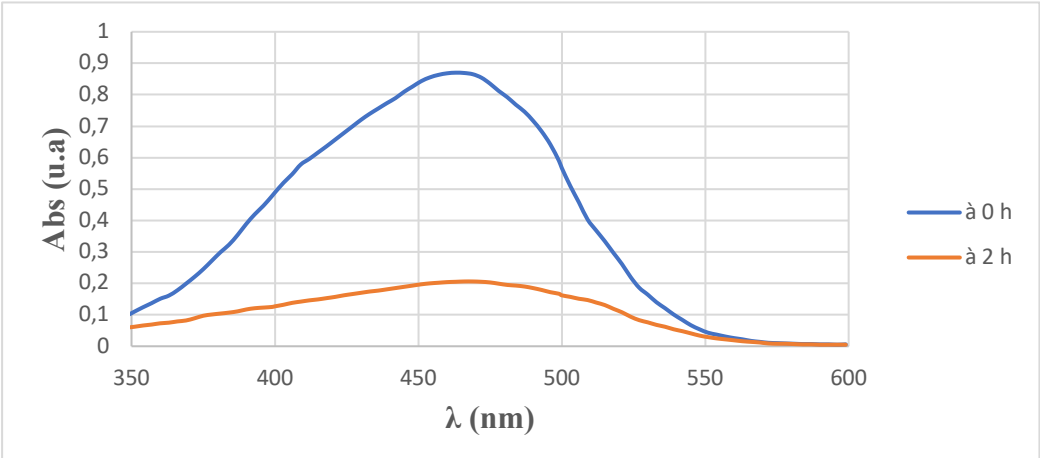

Figure IV-C-22. Absorbance spectrum at optimum inter-electrode distance([MO]= 50mg/L, [Na_2SO_4]= 3.5 g/l, I=0.3A, pH=3, d=1cm).

IV-C.6.Effect of oxygen bubbling

So far, we have been able to determine the best operating conditions for 2 hours of electrolytic treatment, with the electrode pair ($CuFe_2O_4$ /Ti-Pt), the current intensity 0.3A, the inter-electrode distance 1cm, pH=3, the methyl orange concentration 50 ppm and the electrolyte Na_2SO_4 at 3.5 g/l.

In this stage of the study, we will look at the influence of oxygen bubbling on the energy consumed by our treatment to achieve high removal rates.

O_2 bubbling is carried out using a pump used in aquariums, which allows air to be pumped at different flow rates. A low flow rate is used so as not to disturb the solution too much and to encourage radical-pollutant contact.

The results obtained are shown in Figures (IV.C.23, IV.C.24, IV.C.25):

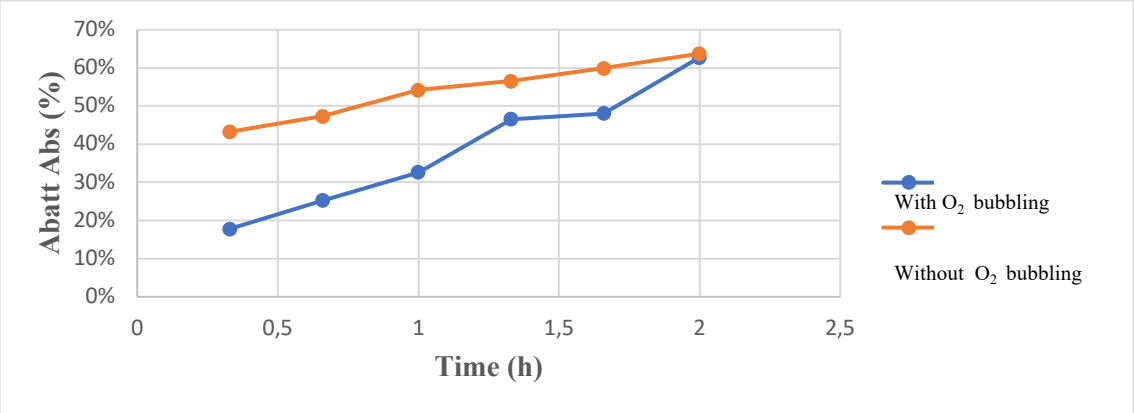

Figure IV-C-23. Effect of oxygen bubbling on degradation of Methylorange ([MO]= 50mg/L, [Na_2SO_4] =3.5g/l, I=0.3A, pH =3, d=1cm).

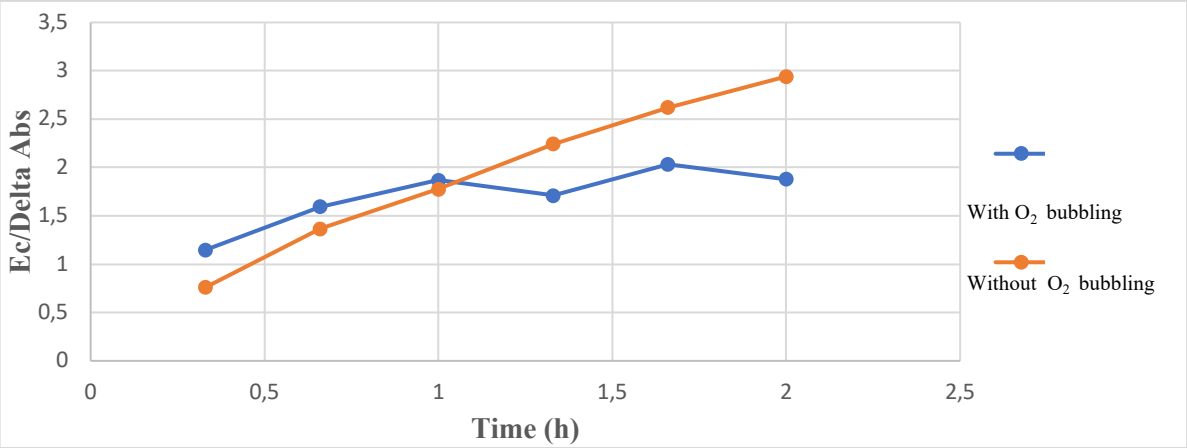

Figure IV-C-24. Effect of oxygen bubbling on energy consumption of Methylorange ([MO]= 50mg/L, [Na_2SO_4] =3.5g/l, I=0.3A, pH =3, d=1cm).

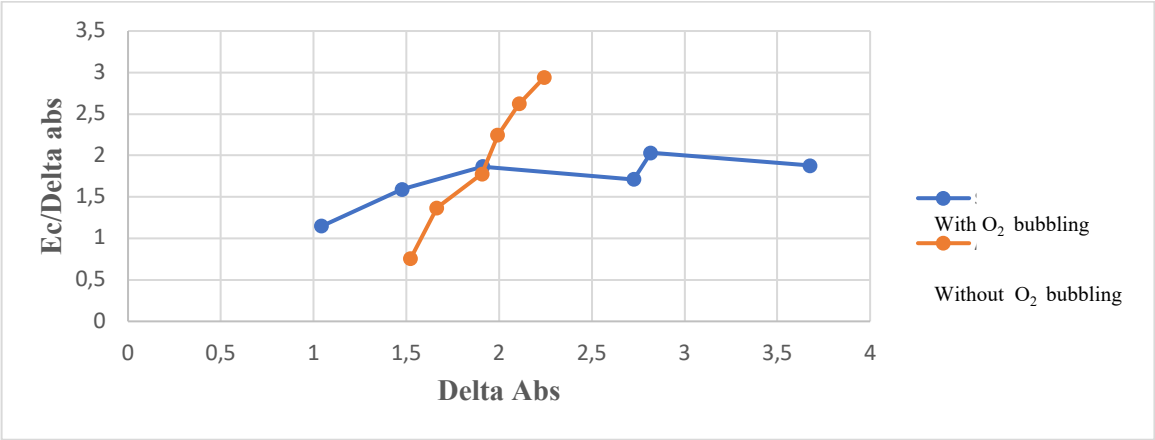

Figure IV-C-25. Effect of oxygen bubbling on the Energy–Absorbance Correlation of Methylorange ([MO]= 50mg/L, [Na_2SO_4] =3.5g/l, I=0.3A, pH =3, d=1cm).

The results recorded in figures (IV.C.23, IV.C.24, IV.C.25) show that:

From the results recorded, the same rate of degradation can be seen with and without oxygen bubbling, but the energy consumed increases with bubbling. This justifies the elimination of this effect.

The absorbance spectrum for optimum degradation of methyl orange is shown in figure (IV.C.26).

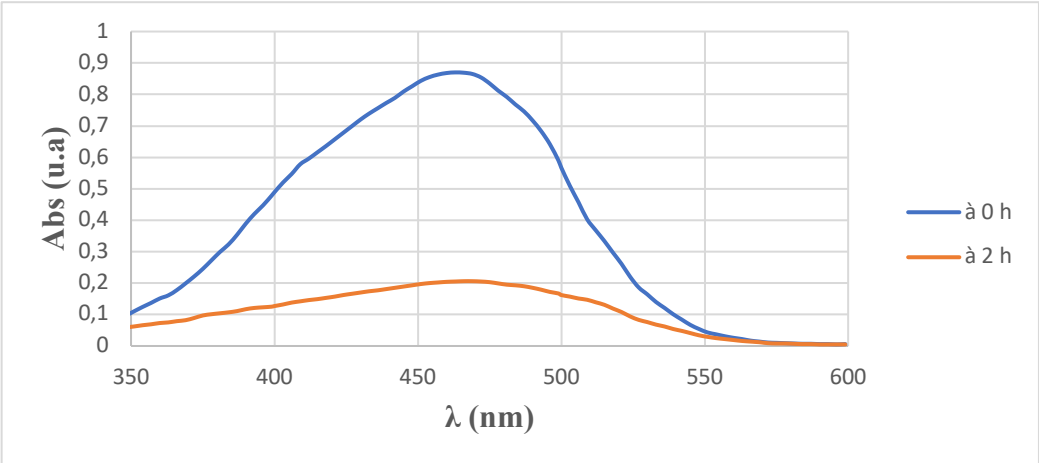

Figure IV-C-26. Absorbance spectrum of bubbling ([MO]= 50 mg/L, [Na_2SO_4] = 3.5 g/l, I=0.3A, pH=3, d= 1cm

IV-D. Modelization of Methyl Orange degradation and mineralisation parameters using a "Box-Behnken" experimental design

Experimental designs are used to optimise the number of experimental trials and develop a theoretical model. This organisation enables the maximum amount of information to be obtained from the minimum number of experiments. It also makes it possible to obtain the best possible accuracy in modelling the results. The experimental design method is based on strict mathematical rules **[51]**. Unlike other designs, the Box-Behnken design requires less experimentation while retaining good statistical properties **[52].**

One of the most important aspects of experimental design is the choice of study factors. These factors are chosen in such a way as to achieve the best elimination efficiency.

- As already mentioned, the yield increases as a function of the current intensity and the latter is proportional to the overproduction of essentially -OH radicals **[53]**.

-We have therefore chosen current intensity as the first factor, denoted (X_1).

- The second factor is attributed to the concentration of the electrolyte in order to minimise the energy dissipated in joule form by increasing the conductivity of the solution, the main objective here is to evaluate the best elimination efficiency as a function of the concentration of the salt used, this factor is noted (X_2).

- The third factor (X_3) was devoted to studying the effect of the nature of the electrolyte on the efficiency of the process used This factor is noted (X_2).

- The third factor (X_3) was used to study the effect of the nature of the electrolyte on the efficiency of the process used **[54]**. Table IV.D.1 lists the factors chosen and the field of study in which the experiment will be carried out.

Table IV-D-1. Factors and domain

Factors	Level -1	Level 0	Level +1
(X_1) Current intensity I(A)	0,1	0,3	0,5
(X_2) [Electrolyte] (g/l)	2	3,5	5
(X_3) Type of electrolyte	$NaNO_3$	Na_2SO_4	NaCl

All the other parameters influencing the reaction are kept constant during the experiments, including:

- an electrolysis time of 2 hours.
- an inter-electrode distance of 10 mm.
- a MO concentration of 50 mg/L.

The responses chosen for this experiment are shown in Table IV.D.2 :

Table IV-D-2. Presentation of responses

Responses	**Abbreviation**	**Units**
Degradation	Abs	%
Mineralization	COD	%
consumed energy	Ec	Wh

Table IV-D-3. Matrix of experiments and experimental results

Experiment (trial) N°	Current intensity (X_1)	[Electrolyte] (X_2)	Nature of electrolyte (X_3)	Abs (u. a. %)	COD (%)	Ec (kW.h/g)
1	0.1	2	2	29	54	0.300
2	0.5	2	2	14	44	1.070
3	0.1	5	2	58	45	0.030
4	0.5	5	2	45	63	0.273
5	0.1	3.5	1	72	55	0.031
6	0.5	3.5	1	65	57	0.483
7	0.1	3.5	3	54	20	0.076
8	0.5	3.5	3	23	26	0.649
9	0.3	2	1	60	35	0.252
10	0.3	5	1	84	5	2.208
11	0.3	2	3	20	5	2.292
12	0.3	5	3	23	21	0.280

13	0.3	3.5	2	74	64	0.119
14	0.3	3.5	2	73	55	0.129
15	0.3	3.5	2	73	65	0.116

IV-D.1.Model establishment

IV-D.1.1. Calculation of coefficients:

â = $(M^t\ M^{-1})\times\ M^t\ \times$ Y **(IV.D.1)** This gives:

$$\hat{a}\ (ABS)= (M^t M^{-1})\times M^t \times Y_1 = \begin{Bmatrix} a_0 \\ a_1 \\ a_2 \\ a_3 \\ a_{12} \\ a_{13} \\ a_{23} \\ a_{11} \\ a_{22} \\ a_{33} \end{Bmatrix} = \begin{Bmatrix} 73.3333 \\ -8.25 \\ 10.875 \\ -20.125 \\ 0.5 \\ -6.00001 \\ -5.25 \\ -15.041 \\ -21.791 \\ -4.791 \end{Bmatrix}$$

$$\hat{a}\ (COD)= (M^t M^{-1})\times M^t \times Y_2 = \begin{Bmatrix} a_0 \\ a_1 \\ a_2 \\ a_3 \\ a_{12} \\ a_{13} \\ a_{23} \\ a_{11} \\ a_{22} \\ a_{33} \end{Bmatrix} = \begin{Bmatrix} 61.333 \\ 2 \\ -0.499 \\ -10 \\ 7 \\ 0.999 \\ 11.5 \\ 6.583 \\ -16.416 \\ -28.416 \end{Bmatrix}$$

$$\hat{a}\ (ECCOD) = (M^t M^{-1})\times M^t \times Y_3 = \begin{Bmatrix} a_0 \\ a_1 \\ a_2 \\ a_3 \\ a_{12} \\ a_{13} \\ a_{23} \\ a_{11} \\ a_{22} \\ a_{33} \end{Bmatrix} = \begin{Bmatrix} 0.121 \\ 0.798 \\ -0.137 \\ 0.481 \\ -0.197 \\ -0.041 \\ 0.120 \\ -0.451 \\ 0.682 \\ 0.546 \end{Bmatrix}$$

These coefficients are used to establish the second-order predictive model. The representation of the main effects and interactions for the results obtained are shown in Figures IV.D.1 . To make these coefficients comparable, they are standardised and divided by their standard deviations. These figures allow us to see how the factors affect the responses.

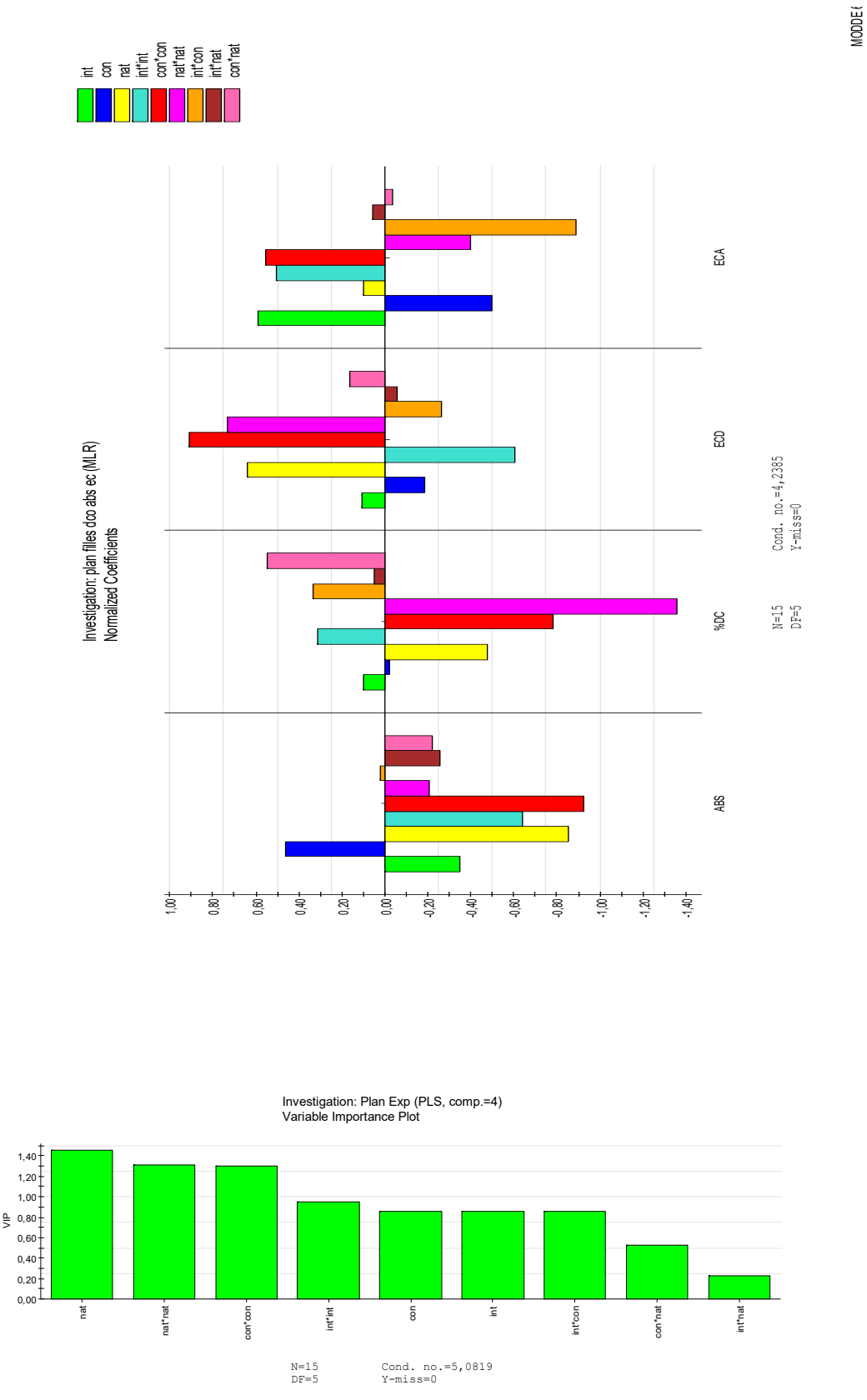

Figure IV-D-1. Effect of main factors and interactions.

Figure IV.D.2 shows the Box-Behnken plane on a cube for three factors.

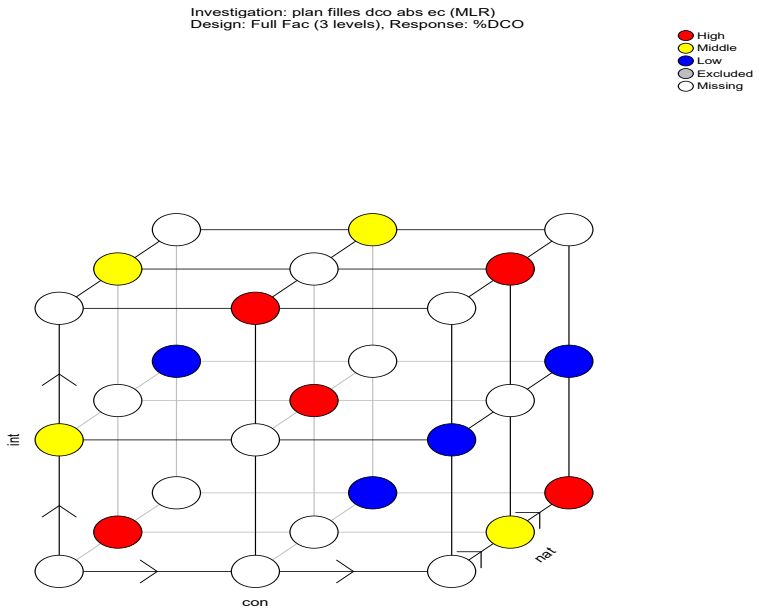

High performance

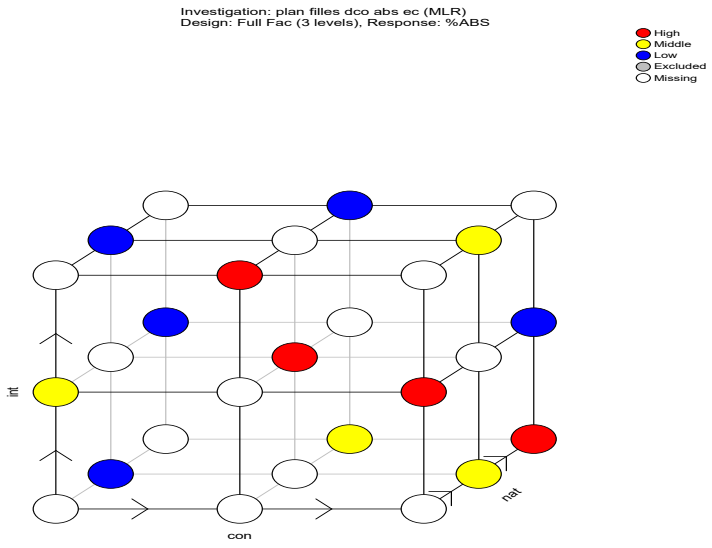

Middle performance

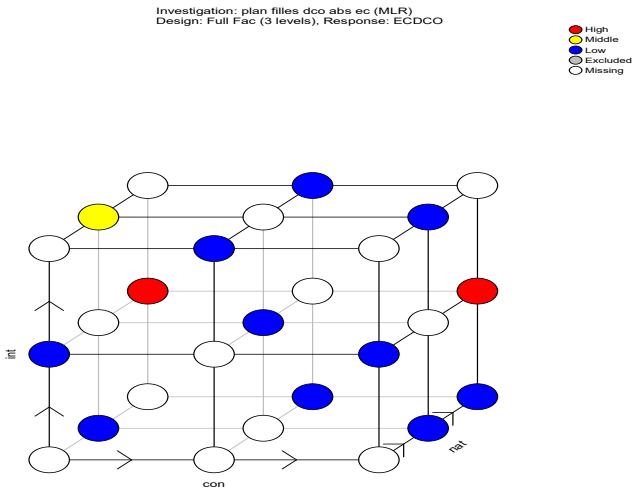

Low performance

Figure IV-D-2. Cube representing yields at different levels**.**

The best conditions correspond to the highest value of degradation and mineralisation efficiency and a minimum EC. The optimum operating conditions are listed in Table IV.D.4.

Table IV-D-4. Operating conditions and optimum results.

Current intensity (A)	**Na_2SO_4**	**Nature of the salt**	**Abs (%)**	**COD (%)**	**Ec (kwh/g O_2)**
0.3	3.5	2	74	64	0.119213
0.5	5	2	45	63	0.27394

Applying the model leads us to the following mathematical equations:

$$\mathbf{Y1}_{\mathbf{(Abs)}} = 73.3333 - 8.25\,x_1 + 10.275\,x_2 - 20.125\,x_3 + 0.5\,x_1 x_2 - 6.00001\,x_1 x_3 - 5.25\,x_2 x_3 - 15.0417\,x_1^2 - 21.791\,x_2^2 - 4.79167\,x_3^2 \quad \textbf{(IV.D.2)}$$

$$\mathbf{Y2}_{\mathbf{(COD)}} = 61.3333 + 2\,x_1 - 0.499995\,x_2 - 10\,x_3 + 7\,x_1 x_2 + 0.999998\,x_1 x_3 + 11.5\,x_2 x_3 + 6.58334\,x_1^2 - 16.4167\,x_2^2 - 28.4167\,x_3^2 \quad \textbf{(IV.D.3)}$$

$$\mathbf{Y3}_{\mathbf{(Ec)}} = 0.121333 + 0.0792749\,x_1 - 0.137625\,x_2 + 0.48175\,x_3 - 0.19775\,x_1 x_2 - 0.041\,x_1 x_3 + 0.1205\,x_2 x_3 - 0.451542\,x_1^2 + 0.682958\,x_2^2 + 0.546708\,x_3^2 \quad \textbf{(IV.D.4)}$$

IV-D.1.2. Simplification of the model

The standard deviation of the residuals allows us to calculate the standard deviations of each coefficient in the model. This will allow us to determine whether the values obtained for each coefficient are significant. The standard deviation of the residuals (σ) is calculated from relationship (IV.D.5) :

$$\sigma = \sqrt{V\ (\text{residuals})} \qquad \textbf{(IV.D.5)}$$

The variance of the residuals is defined by the relationship (IV.D.6) :

$$V(\text{residuals}) = \frac{\text{The sum of squared residuals}}{\text{n}-\text{p}} \qquad \textbf{(IV.D.6)}$$

The residual is the difference between the measured response and the predicted response.

n: number of trials (n= 15).

p: number of coefficients (p= 10).

$V_{Abs}\ (residuals) = \frac{372.473}{15-10}$ $\quad V_{Abs}\ (residuals) = 74.494$

$V_{COD}\ (residuals) = \frac{482.368}{15-10}$ $\quad V_{COD}\ (residuals) = 96.473$

$V_{ECCOD}\ (residuals) = \frac{1.90}{15-10}$ $\quad V_{ECCOD}\ (residuals) = 0.381$

The variance of each of the coefficients of the model considered is given by the formula IV.D.7:

$$Diag\ V\ (\hat{a}) = \sigma^2\ \text{Diag}\ (M\ {}^{t}M)^{-1} \qquad \textbf{(IV.D.7)}$$

Taking the square root of the relationship, we obtain the standard deviations of the coefficients. Table IV.D.5 shows the standard deviations corresponding to each coefficient in the model:

Table IV-D-5. Values of the coefficients and their standard deviations .

Coefficients	**Abs**		**COD**		**Ec**	
	Values	Standard deviations	Values	Standard deviations	Values	Standard deviations
a_0 = constant	73.333	4.895	61.333	5.601	0.121	0.355
a_1= I	-8.25	2.997	2	3.430	0.079	0.217
a_2 = C	10.875	2.997	-0.499	3.430	-0.137	0.217
a_3 = N	-20.125	2.997	-10	3.430	0.481	0.217
a_{12} = I*C	0.5	4.239	7	4.851	-0.197	0.307
a_{13} = I*N	-6.000	4.239	0.999	4.851	-0.041	0.307
a_{23} = C*N	-5.25	4.239	11.5	4.851	0.1205	0.307
a_{11} = I*I	-15.041	4.412	6.583	5.049	-0.451	0.320
a_{22} = C*C	-21.791	4.412	-16.416	5.049	0.682	0.320

a_{33} = N*N	-4.791	4.412	-28.416	5.0492	0.546	0.320

From the results in Table IV.D.5, we can see that some of the values of the standard deviations of the model coefficients are high compared with the eigenvalues of the coefficients. This means that these factors do not have a strong influence on the model studied.

This means that, of the factors studied, the three factors (current intensitý (X_1), electrolyte concentration (X_2) and the nature of the electrolyte (X_3) influence mineralisation and energy consumed (EC) and that the factor (X_3), is a determining factor for them, only the nature of the electrolyte (X_3) and the concentration of the electrolyte (X_2) exert a significant influence on degradation.

IV-D.2.Validation test of the regression equation

- Calculation of the coefficient of determination, prediction and reproducibility

The coefficient of determination, prediction and reproducibility are calculated using **MODDE 6.0** software, and their values are shown in **Table IV.D.6**. To estimate the validity of the model, we calculate the coefficient of determination R2, which indicates the extent to which the model explains the observed values. The closer it is to 1, the better the model fits. It is given by the relation:

$$R^2 = \frac{\sum_{i=0}^{N}(y\mathrm{i} - \mathrm{Y_{mean}})^2}{\sum_{i=0}^{N}(\mathrm{Y\,i} - \mathrm{Y_{mean}})^2} \qquad \textbf{(IV.D.11)}$$

After simplifying the model, it is necessary to make a correction for the systematic error ($R_{corrected}$). The smaller the number of degrees of freedom (F = N - L), the larger the correction coefficient. The correction formula is:

$$R^2_{corrected} = R^2 - (1 - R^2)\frac{\mathrm{L}-1}{\mathrm{N}-\mathrm{L}} \qquad \textbf{(IV.D.12)}$$

With:

Y_i:The measured response.

y_i : The model's predicted response.

Y_{mean} : The average of all the responses Y_i measured.

N: The number of experiments.

L: The number of significant coefficients.

The prediction coefficient (Q^2): Indicates predictive power: above 0.7, the model has good predictive power. Reproducibility is the variation in responses under the same conditions compared with the total variation in responses.

Table IV-D-6. Statistical analysis of results.

Adjustment study	**Degradation**	**Mineralization**	**Consumed energy**
Coefficient of determination R^2	0.952123	0.921245	0.75828
R^2 adjusted	0.865943	0.779486	0.323185
Coefficient of prediction Q^2	0.626697	0.507275	0.236757
Reproducibility	0.9994	0.930666	0.999918

The results show that the model has an average predictive power for mineralization and energy consumed compared to degradation. We can say that the model is adequate.

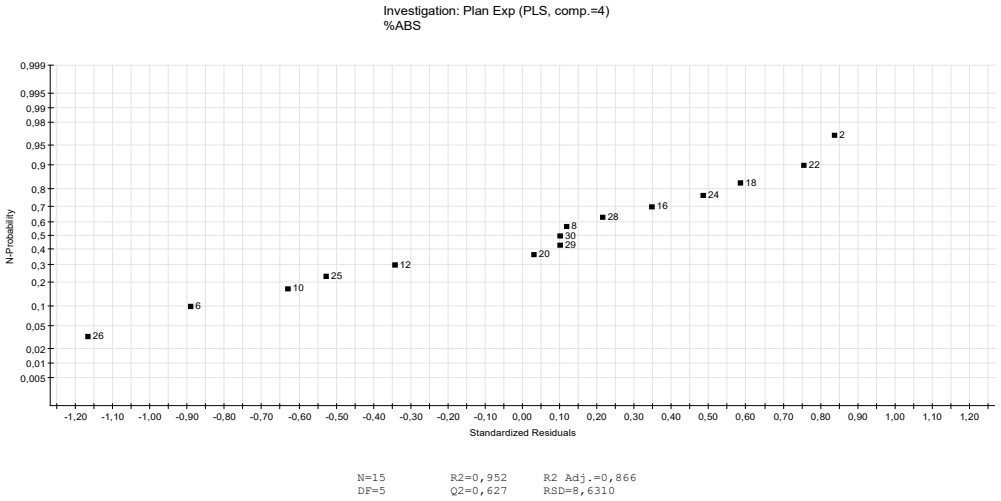

Figure IV-D-3. Measured and predicted responses.

The residual results for the measured and predicted responses are shown in Figure IV.D.4. We can see that the responses follow a normal, linear distribution, which further justifies our deduction.

- The overall results, illustrated by the iso-response curves presented in Appendix A.II, are consistent with those obtained through experimental optimization (IV-C). They confirm the effectiveness of the optimal operating conditions selected for the electrophotocatalysis of methyl orange, ensuring good degradation and mineralization rates with controlled energy consumption.

IV-E. Application of the electrophotocatalysis process to a real discharge

The final part of this study involved applying the optimised conditions determined previously to a discharge from a textile industry located in Blida -Larebea. And testing the toxicity of the water after treatment

IV-E.1. Electrophotocatalysis to a real discharge

Table IV-E-1. Characteristics of the actual discharge before and after treatment

	Initial	**Final**	**Performance**	**Algerian standards [55]**
COD (mg of O_2/l)	90.2	50.6	44%	300
Turbidity (NTU)	31.900	2.320	93%	5

pH	8.850	3.450	61%	6.5-8.5
BOD_5 (mg of O_2/l)	40	25	34.5%	200
SM (g /l)	0.065	0.025	61%	0.035

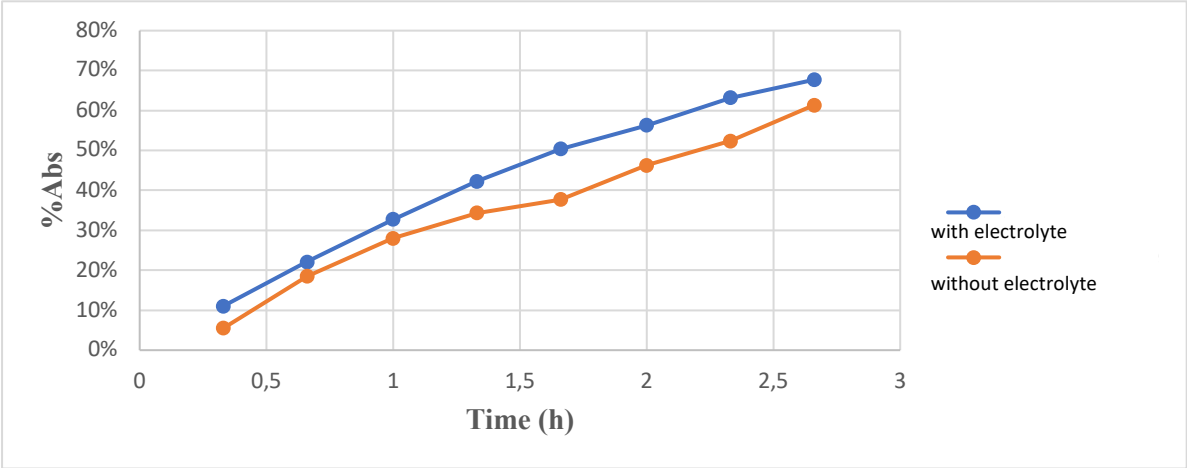

Figure IV-E-1. Effect of electrolyte on degradation of actual discharge.

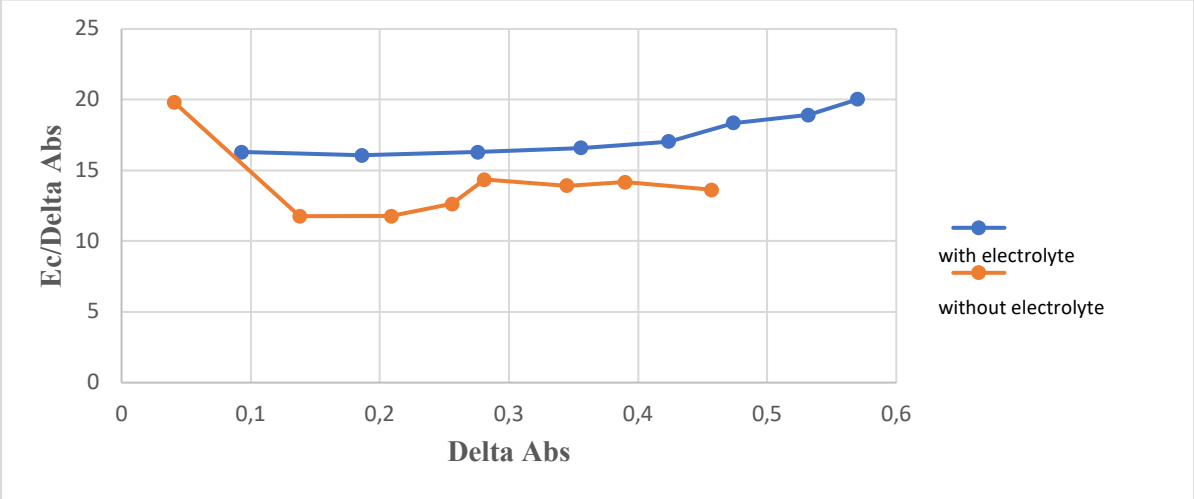

Figure IV-E-2. Effect of electrolyte on energy consumption of actual discharge.

The EC and COD values obtained show that the electrochemical treatment process was effective, and the conditions taken (0.3 A, pH 3 and 3.5 g/l Na_2SO_4, under solar light) effectively degraded the treated effluent.

There was an increase in efficiency in comparison with methyl orange, with a value of 68% versus 63% for MO.

We also found that energy consumption per delta Abs increased considerably over time. As a result, EC = 6,22 Wh per unit of absorbance can be considered the optimum energy for treatment with a high absorbance gradient.

Figure IV-E-3. Measurement of suspended matters (filter before and after).

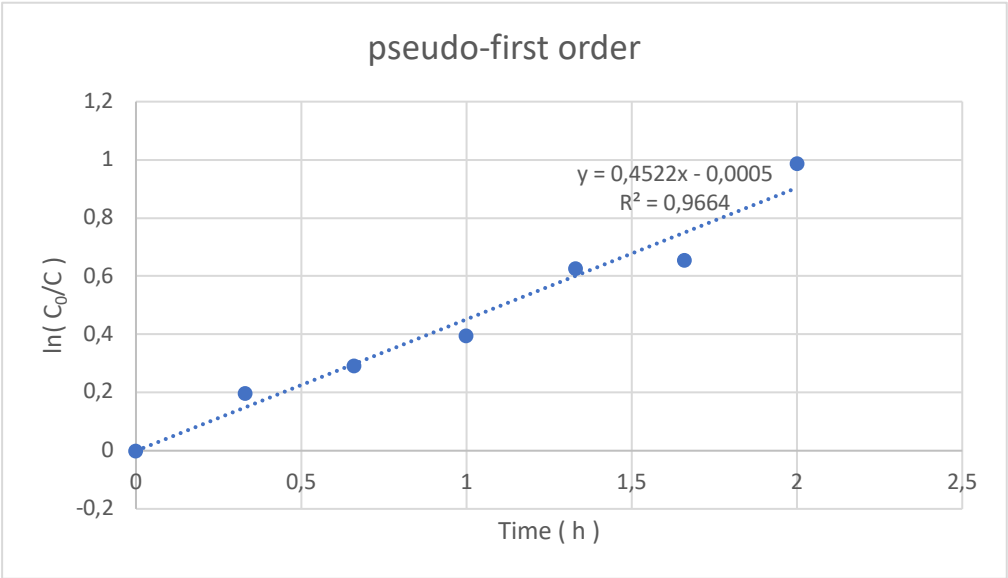

Figure IV-E-4. Degradation kinetics of the actual discharge.

The results of analyses carried out on the discharge before and after electrolysis show that virtually all the parameters measured are well below Algerian standards **[55]**. In addition, the electrophotocatalysis process is effective for eliminating industrial waste loaded with recalcitrant colouring substances and suspended solids. The degradation kinetics Ln (C_0 /C) as a function of time is pseudo-first order, with a kinetic constant of the order of 0.45 min^{-1} and a correlation coefficient of 0.97.

IV-E.2. Wheat seedling growth test

To carry out this experiment we collected all the germinated grains and measured the length of the coleoptiles after four days of growth.

According to the literature, wheat favours pH 6 to 6.5, and as the pH of the treated water was pH 3, this was adjusted to 6.5 before the test.

The results obtained are shown in Table IV.E.2 :

Table IV-E-2. Average length of coleoptiles in wheat seedlings after four days of growth.

Water	**Length of wheat leaves**	**Wheat appearance after 4 days**
Tap water	7.5 cm	
Distilled water	2 cm	
Water before treatment	4 cm	
Water after treatment	6 cm	

From Table IV.E.2, we can see that there is a significant difference in growth, given that the length of the coleoptiles of the wheat seedlings after four days of implantation is greater in the batches (tap water and after treatment) with mean lengths of 7.5 and 6 cm respectively. This shows the non-toxicity of our treated water.

IV-E.3. Microbiological tests

These biotests are carried out on three types of bacteria: Escherichia coli ATCC 25922, Pseudomonas 27853 and Staphe aureus ATCC 25923, which are used to assess antibacterial activity **[56]**.

These bacteria are cultured separately in Petri dishes containing a solid medium (Mueller-Hinton agar). Each dish contains paper discs impregnated with either distilled water, treated waste or untreated waste. If bacterial growth is inhibition of bacterial growth, a white halo (zone of inhibition) will be observed around the paper disc. The greater the inhibition, the larger the diameter of this zone.

After 48 hours of incubation in an oven thermostated at 37°C, the plates were examined. The results are shown in Table IV.E.3 below:

Table IV-E-3. **:** Growth of bacteria after incubation.

Bacterial growth	Bacteria references
	Pseudomonas 278530
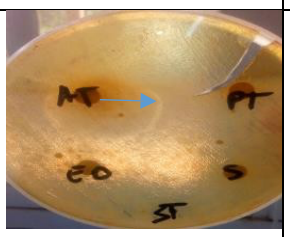	Staph aureus ATCC 25923 1cm
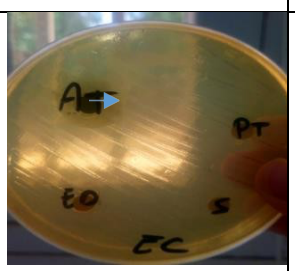	Escherichia coli ATCC 25922 0.8cm

After 24 hours, bacterial resistance was observed in all the kneaded dishes. However, after 48 hours of incubation, we observed a white halo (zone of inhibition), and in the dishes containing Escherichia coli and Staphylococcus aureus, a white halo around the disc.

Table IV.E.3 shows that the discharge before treatment strongly inhibited the growth of two bacteria, Escherichia coli and staphylococcus aureus. The zone of inhibition of staph was greater than that of E. coli, while Pseudomonas developed resistance, and E. coli was more resistant than staph to the toxicity of the effluent. However, as with the control, no zone of growth inhibition was observed for the treated effluent. This means that the treated effluent does not contain any toxic substances that could inhibit growth. Once again, this result demonstrates the effectiveness of the electrophotocatalysis process for treating industrial textile waste.

IV.References chap 4

[1] L. Sun, R. Shao, L. Tang, Z. Chen, Synthesis of $ZnFe_2O_4$/ZnO nanocomposites immobilized on graphene with enhanced photocatalytic activity under solar light irradiation, Journal of Alloys and Compounds. 564 (2013) 55–62. https://doi.org/10.1016/j.jallcom.2013.02.147.

[2] U. Kumar, K. Ankur, D. Yadav, S. Upadhyay, Synthesis and characterization of Ruddlesden-Popper system $(Ba_{1-x}Sr_x)_2SnO_4$, Materials Characterization. 162 (2020) 110198. https://doi.org/10.1016/j.matchar.2020.110198.

[3] Omeiri S, Allalou N, Rekhila G, et al (2013) Preparation and characterization of nano structured Ba_2SnO_4 as a novel photocatalyst material for the chromate reduction. Applied Nanoscience 4:959–966. https://doi.org/10.1007/s13204-013-0276-z

[4] Sahmi A, Bensadok K, Trari M (2024) Electrochemical properties of $CoFe_2O_4$ prepared by sol–gel route. Sono-photocatalysis degradation of Rhodamine B by solar light. Reaction Kinetics, Mechanisms and Catalysis : https://doi.org/10.1007/s11144-024-02608-y

[5] Sahmi A, Bensadok K, Trari M (2024) Efficient oxidation by sono-photo-electrocatalysis of rhodamine B using $MgFe_2O_4$ as photoanode. Journal of Solid State Electrochemistry. https://doi.org/10.1007/s10008-024-05852-3

[6] I.E. Animitsa, E.N. Dogodaeva, N. Tarasova, O.A. Kosareva, A. Neiman, Oxygen-ion and proton transport in $Ba_4Na_2W_2O_{11}$, Solid State Ionics. 185 (2011) 1–5. https://doi.org/10.1016/j.ssi.2010.12.013.

[7] H.T. Dang, T.M.T. Nguyen, T.T. Nguyen, S.Q. Thi, H.T. Tran, H.Q. Tran, T.K. Le, Magnetic $CuFe_2O_4$ Prepared by Polymeric Precursor Method as a Reusable Heterogeneous Fenton-like Catalyst for the Efficient Removal of Methylene Blue, Chemical Engineering Communications.

203 (2016) 1260–1268. https://doi.org/10.1080/00986445.2016.1174858.

[8] R. Peymanfar, F. Azadi, Preparation and identification of bare and capped $CuFe_2O_4$ nanoparticles using organic template and investigation of the size, magnetism, and polarization on their microwave characteristics, Nano-Structures & Nano-Objects. 17 (2019) 112–122. https://doi.org/10.1016/j.nanoso.2019.01.001.

[9] A. Soufi, H. Hajjaoui, R. Elmoubarki, M. Abdennouri, S. Qourzal, N. Barka, Heterogeneous Fenton-like degradation of tartrazine using $CuFe_2O_4$ nanoparticles synthesized by sol-gel combustion, Applied Surface Science Advances. 9 (2022) 100251–100251. https://doi.org/10.1016/j.apsadv.2022.100251.

[10] Omeiri S, Rekhila G, Trari M, Bessekhouad Y (2015) Physical and photoelectrochemical characterizations of $Ba_2SnO_{4-\delta}$ elaborated by chemical route. Journal of Solid State Electrochemistry 19:1651–1658. https://doi.org/10.1007/s10008-015-2786-y

[11] Upadhyay S (2013) High temperature impedance spectroscopy of barium stannate, $BaSnO_3$. Bulletin of Materials Science 36:1019–1036. https://doi.org/10.1007/s12034-013-0578-5

[12] Kumar U, Upadhyay S (2019) Structural, Optical and Electrical Properties of Ruddlesden Popper Oxide Ba_2SnO_4. Journal of Electronic Materials 48:5279–5293. https://doi.org/10.1007/s11664-019-07336-x

[13] M.K. Srivastava, U. Kumar, Structural and optical properties of α-Fe_2O_3 nanoparticles realized by simple thermal decomposition route, Physica Scripta. 96 (2020) 015804. https://doi.org/10.1088/1402-4896/abc281.

[14] I. Ibrahim, I.O. Ali, T.M. Salama, A.A. Bahgat, M.M. Mohamed, Synthesis of magnetically recyclable spinel ferrite (MFe_2O_4, M = Zn, Co, Mn) nanocrystals engineered by sol gel-hydrothermal technology: High catalytic performances for nitroarenes reduction, Applied Catalysis B: Environmental. 181 (2016) 389–402. https://doi.org/10.1016/j.apcatb.2015.08.005.

[15] K. Rouibah, F.Z. Akika, C. Rouibah, H.R. Boudermine, S. Douafer, S. Boukerche, G. Boukerche, M. Benamira, Solar photocatalytic degradation of Methyl green on $CuFe_2O_4$/α Fe2O3 heterojunction, Inorganic Chemistry Communications. 148 (2023) 110361. https://doi.org/10.1016/j.inoche.2022.110361.

[16] R. Rajini, A.C. Ferdinand, Effects of annealing on the structural, morphological and magnetic properties of $CuFe_2O_4$ Ferrite Nanoparticles synthesized by chemical precipitation, Chemical Data Collections. 44 (2023) 100985–100985. https://doi.org/10.1016/j.cdc.2022.100985.

[17] Lahmar H, Kebir M, Nasrallah N, Trari M (2012) Photocatalytic reduction of Cr(VI) on the new hetero-system $CuCr_2O_4$/ZnO. Journal of Molecular Catalysis A-chemical 353-354:74–79. https://doi.org/10.1016/j.molcata.2011.10.026

[18] Mekatel H, Amokrane S, Bellal B, et al (2012) Photocatalytic reduction of Cr(VI) on nanosized Fe_2O_3 supported on natural Algerian clay: Characteristics, kinetic and thermodynamic study. Chemical Engineering Journal 200-202:611–618. https://doi.org/10.1016/j.cej.2012.06.121

[19] A. Sankar, K. Paramasivaganesh, M. Parthibavarman, K. Meganathan, ZIF-8 derived $CuFe_2O_4$ nanoparticles: Evolution of composition and microstructures, and their electrochemical

performances as anode for lithium-ion batteries, Inorganic Chemistry Communications. 140 (2022) 109424–109424. https://doi.org/10.1016/j.inoche.2022.109424.

[20] A.M. Fahim, R.E. Abou-Zeid, A. Kiey, S. Dacrory, Development of semiconductive foams based on cellulose- benzenesulfonate/$CuFe_2O_4$- nanoparticles and theoretical studies with DFT/ B3PW91/LANDZ2 basis set, Journal of Molecular Structure. 1247 (2022) 131390–131390. https://doi.org/10.1016/j.molstruc.2021.131390.

[21] K. Baruah, A. Kant, P. Gaijon, S. Ghosh, M.K. Singh, Synthesis of Cu@$CuFe_2O_4$ nanocomposite and its application as an efficient catalyst for the production of oxygen, Applied Surface Science Advances. 6 (2021) 100130–100130. https://doi.org/10.1016/j.apsadv.2021.100130.

[23] Haynes WM (2014) CRC Handbook of Chemistry and Physics, 95th Edition. Taylor & Francis Ltd

[24] A.Sahmi,Degradation and mineralization of a phenolic organic molecule by the electrophotocatalysis technique , PhD thesis in science, USTHB Algeries,(2018) .

[25] Brillas E, Garcia-Segura S, Skoumal M, Arias C (2010) Electrochemical incineration of diclofenac in neutral aqueous medium by anodic oxidation using Pt and boron-doped diamond anodes. Chemosphere 79:605–612. https://doi.org/10.1016/j.chemosphere.2010.03.004

[26] V. Yadav, R. Bhatnagar, U. Kumar, Enhancement in the Electrocatalytic and Optoelectronic Performance of Cost-Effective Counter Electrode VO_2 for Dye-Sensitized Solar Cell (DSSC), Advances in Condensed Matter Physics. 2024 (2024) 1–13. https://doi.org/10.1155/2024/6613380.

[27] Sahmi A, Omeiri S, Bensadok K, Trari M (2019) Electrochemical properties of the scheelite $BaWO_4$ prepared by co-precipitation: Application to electro-photocatalysis of ibuprofen degradation. Materials Science in Semiconductor Processing 91:108–114. https://doi.org/10.1016/j.mssp.2018.11.017

[28] N. Boutal, G. Rekhila, K. Taïbi, M. Trari, Relaxor ferroelectric and photo-electrochemical properties of lead-free $Ba_{1-x}Eu_{2x/3}(Ti_{0.75}Zr_{0.25})O_3$ ceramics. Application to chromate reduction, Solar Energy. 99 (2014) 291–298. https://doi.org/10.1016/j.solener.2013.11.019.

[29] Hua W, Kang Y (2023) Synergistic degradation of Orange G in water via water surface plasma assisted with β-Bi_2O_3/$CaFe_2O_4$. 40:1122–1132. https://doi.org/10.1007/s11814-022-1278-x

[30] Sahmi A, Laib R, Omeiri S, et al (2019) Photoelectrochemical properties of Ba_2TiO_4 prepared by nitrate route. Application to electro-photocatalysis of phenobarbital mineralization by solar light. Journal of Photochemistry and Photobiology A: Chemistry 372:29–34. https://doi.org/10.1016/j.jphotochem.2018.12.003

[31] W. Hua, Y. Kang, Synergistic degradation of Orange G in water via water surface plasma assisted with β-Bi_2O_3/$CaFe_2O_4$, Environmental Engineering. 40 (2023) 1122–1132. https://doi.org/10.1007/s11814-022-1278-x.

[32] A. Sahmi, R. Laib, S. Omeiri, K. Bensadok, M. Trari, Photoelectrochemical properties of Ba_2TiO_4 prepared by nitrate route. Application to electro-photocatalysis of phenobarbital mineralization by solar light, Journal of Photochemistry and Photobiology A: Chemistry. 372 (2019) 29–34. https://doi.org/10.1016/j.jphotochem.2018.12.003.

[33] F.M.M. Paschoal, M.A. Anderson, M.V.B. Zanoni, The photoelectrocatalytic oxidative treatment of textile wastewater containing disperse dyes, Desalination. 249 (2009) 1350–1355. https://doi.org/10.1016/j.desal.2009.06.024.

[34] A. Sahmi, R. Laib, S. Omeiri, K. Bensadok, M. Trari, Photoelectrochemical properties of the perovskite $BaSnO_3$ synthetized by chemical route. Application to electro-photocatalytic mineralization of ibuprofen, Journal of Photochemistry and Photobiology A: Chemistry. 364 (2018) 443–448. https://doi.org/10.1016/j.jphotochem.2018.06.034.

[35] Paschoal FMM, Anderson MA, Zanoni MVB (2009) The photoelectrocatalytic oxidative treatment of textile wastewater containing disperse dyes. Desalination 249:1350–1355. https://doi.org/10.1016/j.desal.2009.06.024

[36] C. García-Gómez, P. Drogui, F. Zaviska, B. Seyhi, P. Gortáres-Moroyoqui, G. Buelna, C. Neira-Sáenz, M. Estrada-alvarado, R.G. Ulloa-Mercado, Experimental design methodology applied to electrochemical oxidation of carbamazepine using Ti/PbO2 and Ti/BDD electrodes,,J. Electroanal. Chem., 732 (2014), pp. 1-10

[37] Wang Q, Lembley AT J., Agric. Food Chem. modeling evaluation of carbaryl degradation in a continuously stirred tank reactor by anodic fenton treatment, (2002),50:2331-2337

[38] Nidheesh P & Gandhimathi R (Trends in electro-Fenton process for water and wastewater treatment): an overview. Desalination 299:1-15, (2012)

[39] S.W. da Silva, E.M.O. Navarro, M.A.S. Rodrigues, A.M. Bernardes, V. Pérez-Herranz

Using p-Si/BDD anode for the electrochemical oxidation of norfloxacin, J. Electroanal. Chem., 832 (2019), pp. 112-120

[40]CA Martínez-Huitle, MA Rodrigo, I. Sirés, O. Scialdone, Procédés *et réacteurs* électrochimiques simples et couplés pour la réduction des polluants organiques de l'eau : *une revue critique***,** Chem. Rev, 115 (2015), p. 13362 – 13407.

[41] Chachou L, Gueraini Y, Bouhalouane Y, Poncin S, LiK HZ, Bensadok K Environmental Technology, (2015), 36:1924-1932.

[42] H. Särkkä, A. Bhatnagar, M. Sillanpää, Recent developments of electro-oxidation in water treatment-a review, J. Electroanal. Chem., 754 (October) (2015), pp. 46-56

[43] A. Ansari, D. Nematollahi, Convergent paired electrocatalytic degradation of p-dinitrobenzene by Ti/SnO2-Sb/β-PbO2 anode. A new insight into the electrochemical degradation mechanism,Appl. Catal. B, 261 (2020), p. 118226,

[44] J. Zhao , C. Zhu , J. Lu , C. Hu , S. Peng , T. Chen,Dégradation électrocatalytique du bisphénol A avec électrode modifiée Co 3 O 4 /β-PbO 2 /Ti, Electrochim. Acta ,118 (2014) , p. 169 – 175.

[45] Brillas E, Sires I, Arias C, Pere Luis Cabot PL, Centellas F, Rodriguez RM, Jose Garrido JA, Electrochemical Degradation of Paracetamol from Water by Catalytic Action of Fe^{2+}, Cu^{2+}, and UVA Light on Electrogenerated Hydrogen Peroxide, (2005) Chemosphere, 58:399-406.

[46] Chiang LC, Chang JE, Wen TC,_Indirect oxidation effect in electrochemical oxidation treatment of landfill leachate, (1995) Journal of Environmental Science and Health, 30:753-771.

[47] M.Millet, L'oxygène et les radicaux libres (2e partie), (1992), Bios 23:45-50.

[48] Feng Qi-yan, LI Xiang-dong, Cheng Yu-jie, Meng Lei, Meng Qing-jun._Removal of Humic Acid from Groundwater by Electrocoagulation ,(J China Univ Mining & Technology) , 17, 513 – 515, (2007).

[49] Modirshahla, N,Behnajady,M.A.,Kooshaiian, S.(Dyes and Pigments, 74, 249- 257, Investigation of the effect of sol–gel synthesis variables on structural and photocatalytic properties of TiO2 nanoparticles,(2007).

[50] Kamaraj, R., Vasudevan, S.. (Chemical Engineering Research and Design), 03.021,(2014)

[51] Livre de Goupy, 2010.

[52] Myers RH, Montgomery DC (2002), 2nd Edition, John Wiley and Sons, New York, NY, USA, 798 p.

[53] Wang Q, Lembley AT J, Agric. Food Chem._Oxidation of Carbaryl in Aqueous Solution by Membrane Anodic Fenton Treatment , (2002) ,50:2331-2337 .

[54] Doré M (1989) Chimie des oxydants et traitement des eaux. Tec. Doc. Lavoisier, Paris,France.

[55] Official Journal of the Algerian Republic n° 26, April 23, 2006

[56] X Li , T Chen , Y Qiu , Z Zhu , H Zhang , D Yin ;Magnetic dual Z-scheme $gC_3N_4/BiVO_4/CuFe_2O_4$ heterojunction as an efficient visible-light-driven peroxymonosulfate activator for levofloxacin degradation ; Chemical Engineering Journal; 15 January 2023

General conclusion

General conclusion

The electrophotocatalysis is a promising, clean and free technique for decontaminating polluted water. The use of solar energy (an inexhaustible source of energy), together with non-toxic catalytic substances, make this process sustainable and attractive both ecologically and economically. This technique can be considered a green process. To this end, we have synthesised two semiconducting materials crystallising in the spinel and perovskite structures; $CuFe_2O_4$ and Ba_2SnO_4 by the sol-gel and chemical synthesis methods and studied their physico-chemical, optical and photo-electrochemical properties.

The main results are :

- The DRX spectra of $CuFe_2O_4$ and Ba_2SnO_4 are indexed in a tetragonal symmetry (SG: I41/amd N° 141) and (SG: I4/mmm), which is in good agreement with the two ASTM data sheets.
- The SEM images of $CuFe_2O_4$ shows a compact structure with a rough surface and medium porosity, and the EDX spectra confirm the purity of the oxide. While the SEM micrograph of Ba_2SnO_4 indicates a compact structure with a rough surface and a small porosity. Assuming spherical and non-porous crystallites.
- The FT-IR spectrum of $CuFe_2O_4$ shows water adsorption on the surface, indicated by bands at 3650 cm^{-1} and 1675 cm^{-1}, and reveals Cu-O and Fe-O bonds in the octahedral and tetrahedral sites of the spinel. When The FT-IR spectrum of Ba_2SnO_4 primarily shows peaks for Sn–O vibrations in SnO_6 octahedra and Ba–O bonds, with additional weak peaks attributed to adsorbed carbonates, O–H groups, and water, likely due to the increased reactivity from the small particle size.

- Diffuse reflectance results showed that the $CuFe_2O_4$ and Ba_2SnO_4 oxides have a gap energy of 1.72 and 3.18 eV respectively, allowing good absorption in the UV range.
- The potential of the flat band, and the type of conduction characteristic of the catalyst, was determined from the intensity-potential curves and confirmed by the Mott-Schottky curves. The results of these characterisations enabled us to position the conduction and valence bands in relation to the vacuum and then to draw the energy diagram.
- An experimental setup was developed. The kinetic study of the electrocatalysis and electrophotocatalysis of RhB with $CuFe_2O_4$ and Ba_2SnO_4 demonstrated the catalytic activity of these materials in degrading and eliminating a recalcitrant organic compound, proving the effectiveness of our process. We concluded that the results obtained with electrophotocatalysis are even better.

- Optimisation of orange methyl elimination using a three-factor Box-Behnken experimental design. The various factors taken into account are : Current intensity, electrolyte concentration, electrolyte type. All the data generated was used to define optimum conditions for maximum degradation with minimum treatment cost. The results of the optimisation confirm that the model is significant, with actual values very close to those predicted, and an R^2 correlation coefficient very close to 1.
- The 2-hours treatment of real textile effluent (from the Blida textile plant) by electro-photo-catalysis under solar irradiation resulted in the elimination of 68,93, 34.5, and 44 % degradation, of BOD_5, TSS and COD respectively, corresponding to final values below the discharge standards. This reflects the performance of the processś with regard to emerging textile pollutants.
- Verification of our process by the microbial test was further proof of the process's effectiveness, as the growth of the three types of bacteria used (Escherichia coli and Pseudomonas and Staphylococcus aureus) was not inhibited after treatment by electro-photo-catalysis.
- The electro-photocatalysis process can therefore be applied on an industrial scale for the treatment of persistent organic pollutants. From our study we can deduce that 24 kwh is the energy required to produce 1 m^3 of ultra-pure water for pharmaceutical or electronic use

Appendix

Appendix A1. Experimental design methodology

A1.1 Postulated mathematical model

mathematical model generally used with the Box-Behnken design is a second-order model with second-order interactions [1]:

$$y = a_0 + a_1x_1 + a_2x_2 + a_3x_3 + a_{12}x_1x_2 + a_{13}x_1x_3 + a_{23}x_2x_3 + a_{11}x_{12} + a_{22}x_{22} + a_{33}x_{32} + e \quad (A1)$$

With

yi response i; $\mathbf{x_1}$, $\mathbf{x_2}$and $\mathbf{x_3}$, represent the levels (+1, 0 or -1) of trials for factors 1, 2 and 3 respectively; $\mathbf{a_1}$, $\mathbf{a_2}$and $\mathbf{a_3}$represent the effects of factors 1, 2 and 3 respectively; $\mathbf{a_{12}}$, $\mathbf{a_{13}}$and $\mathbf{a_{23}}$represent the interaction between factors 1 and 2, 1 and 3, and 2 and 3 respectively; $\mathbf{a_{11}}$, $\mathbf{a_{22}}$and $\mathbf{a_{33}}$are quadratic coefficients.

This model has 10 coefficients. A minimum of 10 equations is therefore required to estimate them. The classical Box-Behnken design for three factors has 15 experimental points, each giving one equation. This leaves 5 equations, or 5 degrees freedom, to calculate the residual.

A1.2 Calculation matrix

It's a (15,10) matrix, since there are 15 experiments and 10 coefficients. This matrix is constructed from the experimental design and the postulated model.

$$M = \begin{pmatrix} +1 & -1 & -1 & 0 & +1 & 0 & 0 & +1 & +1 & 0 \\ +1 & +1 & -1 & 0 & -1 & 0 & 0 & +1 & +1 & 0 \\ +1 & -1 & +1 & 0 & -1 & 0 & 0 & +1 & +1 & 0 \\ +1 & +1 & +1 & 0 & +1 & 0 & 0 & +1 & +1 & 0 \\ +1 & -1 & 0 & -1 & 0 & +1 & 0 & +1 & 0 & +1 \\ +1 & -1 & 0 & +1 & 0 & -1 & 0 & +1 & 0 & +1 \\ +1 & +1 & 0 & -1 & 0 & -1 & 0 & +1 & 0 & +1 \\ +1 & +1 & 0 & +1 & 0 & +1 & 0 & +1 & 0 & +1 \\ +1 & 0 & -1 & -1 & 0 & 0 & +1 & 0 & +1 & +1 \\ +1 & 0 & +1 & -1 & 0 & 0 & -1 & 0 & +1 & +1 \\ +1 & 0 & -1 & +1 & 0 & 0 & -1 & 0 & +1 & +1 \\ +1 & 0 & +1 & +1 & 0 & 0 & +1 & 0 & +1 & +1 \\ +1 & 0 & 0 & 0 & 0 & 0 & 0 & 0 & 0 & 0 \\ +1 & 0 & 0 & 0 & 0 & 0 & 0 & 0 & 0 & 0 \\ +1 & 0 & 0 & 0 & 0 & 0 & 0 & 0 & 0 & 0 \end{pmatrix}$$

A1.3 Information matrix

The information matrix is calculated from the calculation matrix, a (10,10) matrix.

$M^t M =$

15	0	0	0	0	0	0	8	8	8
0	8	0	0	0	0	0	0	0	0
0	0	8	0	0	0	0	0	0	0
0	0	0	8	0	0	0	0	0	0
0	0	0	0	4	0	0	0	0	0
0	0	0	0	0	4	0	0	0	0
0	0	0	0	0	0	4	0	0	0
8	0	0	0	0	0	0	8	4	4
8	0	0	0	0	0	0	4	8	4
8	0	0	0	0	0	0	4	4	8

A1.4. Dispersion matrix

The dispersion matrix is the inverse of the information matrix, and is also a (10,10) matrix:

$(M^t M)^{-1} =$

0,333	0	0	0	0	0	0	-0,167	-0,167	-0,167
0	0,125	0	0	0	0	0	0	0	0
0	0	0,125	0	0	0	0	0	0	0
0	0	0	0,125	0	0	0	0	0	0
0	0	0	0	0,250	0	0	0	0	0
0	0	0	0	0	0,250	0	0	0	0
0	0	0	0	0	0	0,250	0	0	0
-0,167	0	0	0	0	0	0	0,271	0,021	0,021
-0,167	0	0	0	0	0	0	0,021	0,271	0,021
-0,167	0	0	0	0	0	0	0,021	0,021	0,271

A1.5. Modeling

Our aim is to optimize the parameters under consideration (Abs (%), COD (%) and EC (kWh/g O_2). In other words, maximizing degradation and mineralization efficiency, while reducing energy consumption. Based on our experimental results (Table IV-D-3), we could wrote the response matrices :

Appendix A2. Interpretation of results

The aim is to achieve good degradation and mineralization performance minimum energy consumption. We look for the region of the study area where these conditions are met. As the study domain is three-dimensional, we make cross-sections to better see the details of the iso-response surfaces. To do this, we examined each parameter separately.

A2.1. Degradation

X 1 = constant (-1,0 and +1)

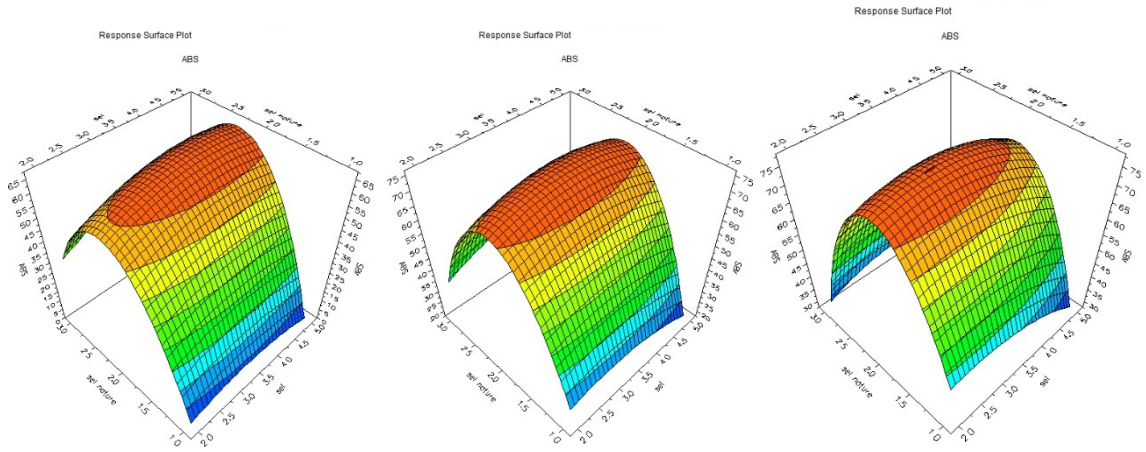

Figure A1. Iso-response curves for degradation in the X_1plane= constant (-1, 0 and +1)

From the figures above, we can see that :

Degradation efficiency is high whatever current intensity.

For x_1= -1, degradation efficiency reaches 65%, with Na_2SO_4electrolyte concentration of 2.5 to 5 g/l.

For x_1= 0, the degradation yield reaches 70% $_{(x3=2=Na2SO4)}$ all $x_2$levels, with good turndown of 75% at the $x_2$factor center ($_{() x2=(.5g/l))}$.

At x_1= +1, degradation efficiency reaches 75%, in the Na_2SO_4electrolyte concentration range from 2.5 to 4.5 g/l.

We can clearly see that degradation efficiency is highest (78%) in the region closest to 0.3 A, and from 3.3 to 3.7 g/l Na_2SO_4.

X 2 = constant (-1,0 and +1)

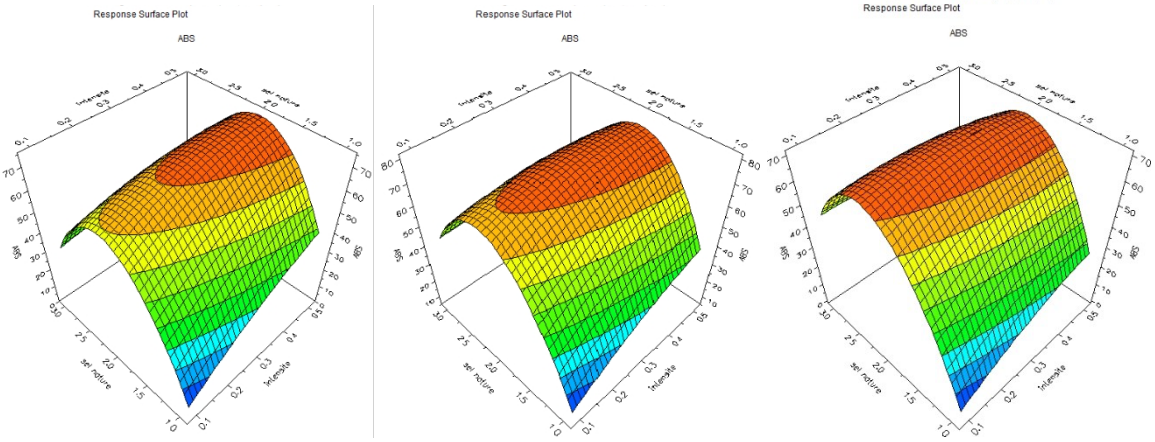

Figure A2. Iso-response curves for degradation on the X_2plane= constant (-1, 0 and +1)

From figures A2, we can see that :

The degradation efficiency remains high whatever current intensity for Na_2SO_4electrolyte.

For x_2= -1, the degradation efficiency reaches 70% for a current intensity between 0.29 and 0.5 A, with the Na_2SO_4electrolyte.

For x_2=$_0$, the degradation efficiency reaches 78% for a current intensity between 0.2 and 0.5A, at the center of the $x_3$domain.

For x_2= +1, the degradation efficiency reaches 65% for any current intensity between 0.2 and 0.5 A, with x_3= 2.

X 3 = constant (-1,0 and +1)

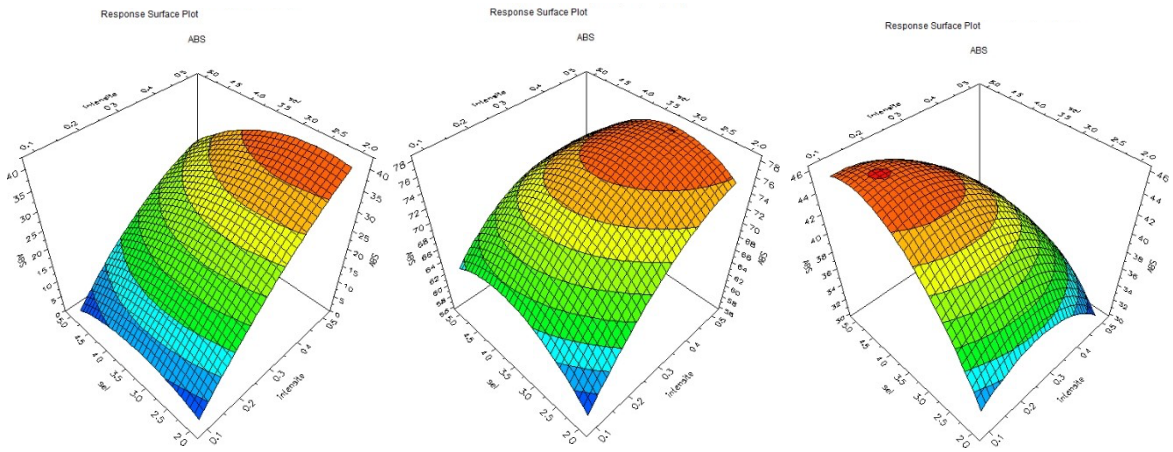

Figure A3. Iso-response curves for degradation on the X_3plane= constant (-1, 0 and +1)

From figures A3, we can see that the degradation efficiency becomes less important (< 45%) for both levels $x_3 = \pm 1$ whatever the current intensity and their solution concentration.

For $x_3 = -1$, the degradation efficiency reaches 35% for a current intensity of between 0.4 and 0.5 A, with a $NaNO_3$concentration varying from 2 to 3.7 g/L.

For $x_3 = 0$, the degradation efficiency reaches 76% for a current intensity of between 0.35 and 0.5 A, and for any Na_2SO_4salt concentration ranging from 2.3 to 5 g/L.

For $x_3 = +1$, the degradation efficiency reaches 44% for a current intensity of between 0.1 and 0.3 A, with a NaCl concentration varying from 3.75 to 5 g/L. And that the maximum located in the center (4.3 g/L) with an abatement of only 46 %.

A2.2. Mineralization

In the case of X 1 = constant (-1, 0 and +1)

Beginning with cuts parallel to the planes X_1= constant, i.e. current intensity, we choose values of -1, 0 and +1 for this constant. We obtain the iso-response curves shown in Figure A5.

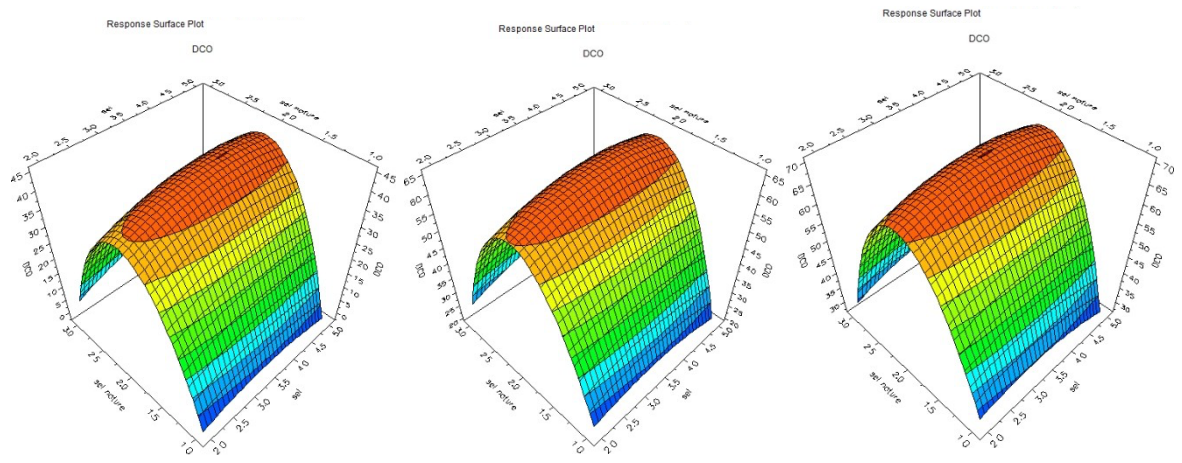

Figure A4. Iso-response curves for mineralization on the X 1 plane= constant (-1, 0 and +1)

The iso-response surfaces shown Figure A4 demonstrate that, for both levels of factor X_1= (0, +1), with the Na_2SO_4electrolyte, mineralization efficiency increases. On the other hand, for a current intensity at level (0) and a concentration close to level (+1), a maximum mineralization of 70.2% can be achieved. However, the most interesting result is the demonstration of the existence of an optimum current intensity, where mineralization is maximal.

X 2 = constant (-1, 0 and +1)

An analysis of iso-response surfaces on the X_2= constant (-1, 0 and +1) plane gives us a better visualization of this optimal current region, the results of which are shown in figure A5.

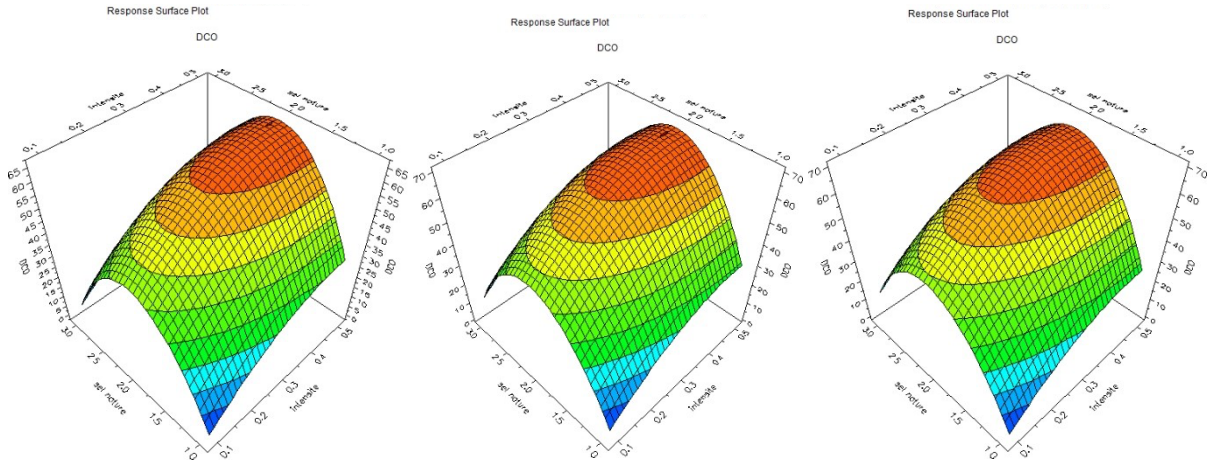

Figure A5. Iso-response for mineralization on the X 2 plane= constant (-1, 0 and +1)

We can clearly see the existence of an optimal current intensity region where mineralization is maximal. Reaction at a current intensity close to 0.4 A, and an electrolyte concentration of between 3.5 and 5 g/L at the center of x_3, would result in 70% mineralization.

In the case of X 3 = constant (-1, 0 and +1)

The representation of iso-response surfaces on the X_3plane is shown figure A6.

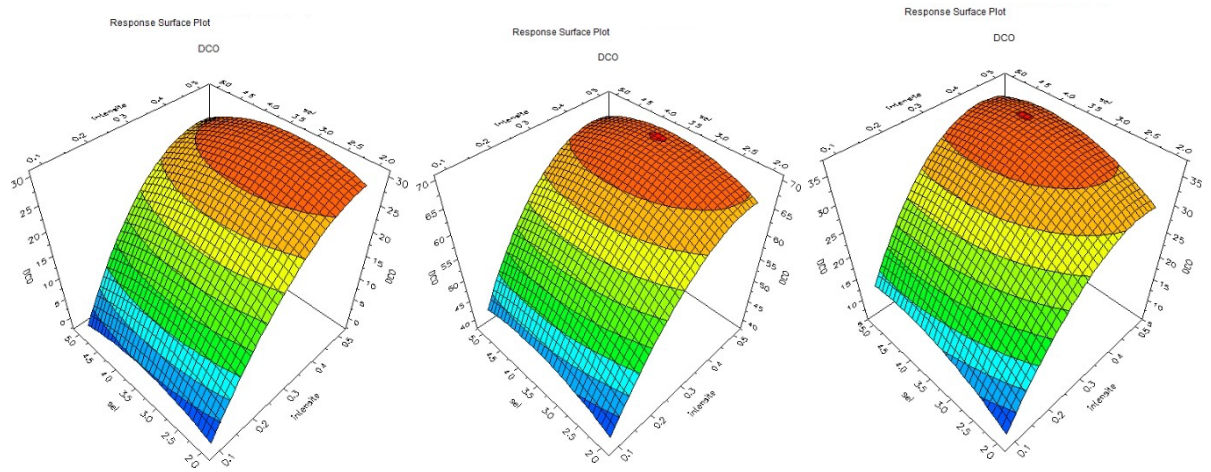

Figure A6. Iso-response curves for mineralization on the X_3plane= constant (-1, 0 and +1)

For the level (X 3 = -1), we can obtain a mineralization of 30% if the current intensity is between 0.38 and 0.5 A, with X2 varying from 2 to 4.5 g/L. From an economic point of view, it's in our interest to choose a current intensity of 0.38 A. This is the value at which the energy consumed is lowest.

For the level (X_3= 0), we can obtain 70% mineralization if the current intensity is between 0.4 and 0.5 A, with X2 varying from 2.5 to 4.5 g/L.

For the level (X_3= +1), we can obtain 35% mineralization if the current intensity is between 0.35 and 0.5 A, with X2 varying from 2.75 to 5 g/L.

In conclusion, under the optimum conditions determined. For a current intensity equal to 0.45 A, and an electrolyte concentration (X_3= 0) of 3.5 g/L, mineralization reaches around 71.2%.

A2.3. Energy consumption

In the case of X_1= constant (-1,0 and +1)

The iso-response curves for consumed energy are represented in the same way as those for degradation and mineralization. Figure A7 shows the iso-response curves for consumed energy on the X_1=constant plane (- 1, 0 and +1).

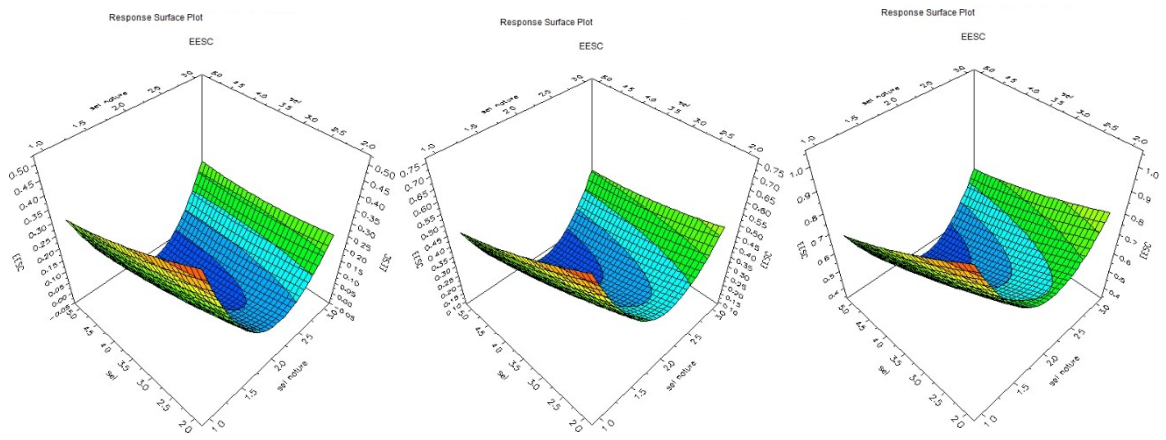

Figure A7. Iso-response curves energy consumed on the X 1 plane= constant (-1, 0 and +1)

The iso-response surfaces on the X_1= constant plane confirm what we have already commented on (for high current intensities, the energy consumed is significant). If we go from level -1 to level +1, the CE increases from 0.25 to 0.5 kWh/g O_2, with any NaCl electrolyte concentration. And for $NaNO_3$electrolyte, it increases from 0.3 to 0.8 kWh/g O_2.

For the zero level (X_1= 0), this CE value (0.05 kWh/g O_2removed) is observed at X_3= 0 and X_2between 3.75 and 5 g/L, while for the levels (X_1= -1), (X_1= +1), 0.075, and 0.5 kWh/g $O_2$are observed respectively. However, most interesting result is the demonstration of the existence of an optimum current intensity, where the energy consumed is minimal.

X 2 = constant (-1, 0 and +1)

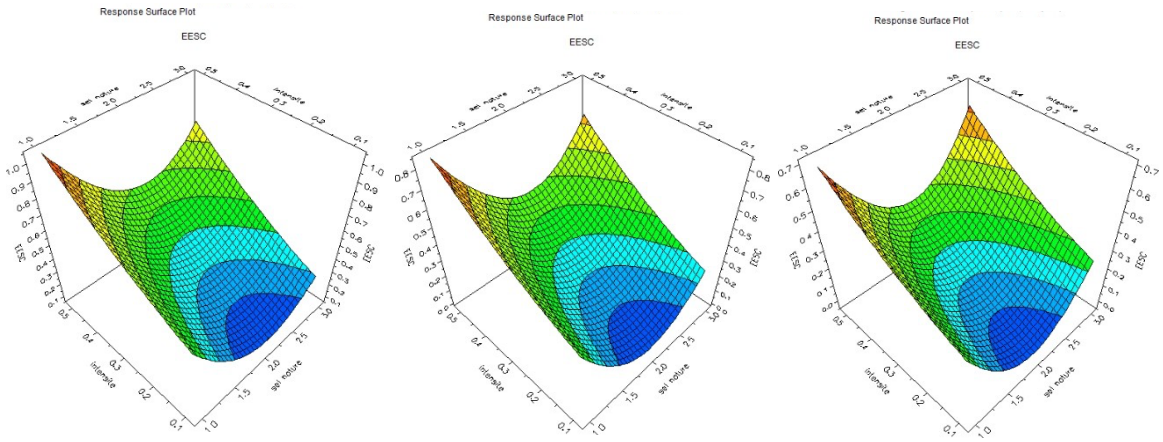

Figure A8. Iso-response curves energy consumed on the X_2plane= constant (-1, 0 and +1)

Figure A8 shows that for iso-response surfaces represented on the X_2= constant plane, the CE increases with increasing current intensity, and is minimal at X_2= -1. This energy reaches 0.05 kWh/g O_2over a range of current intensities (from 0.1 to 0.2 A) within the three limits of the study domain (X_2= - 1, 0, +1). However, the most interesting result is the existence of a better electrolyte, where the energy consumed is minimal.

X 3 = constant (-1,0 and +1)

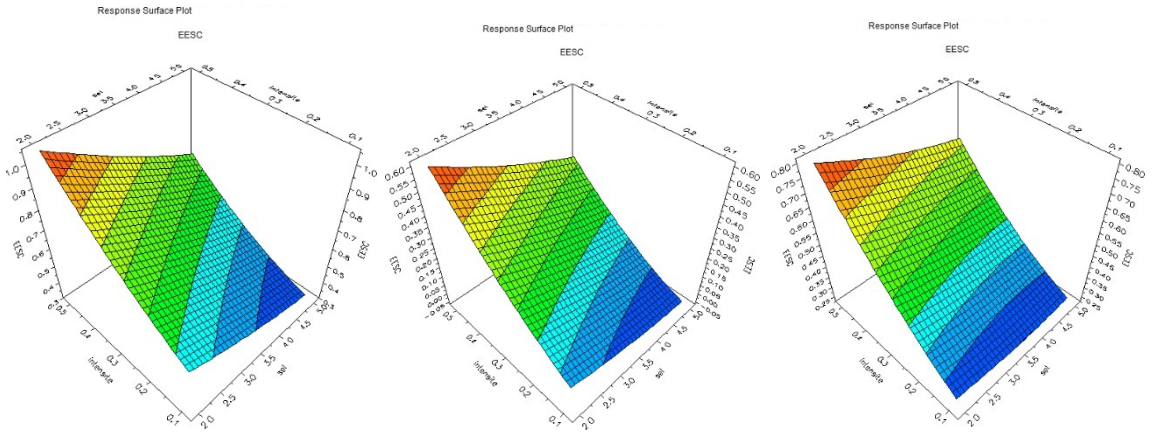

Figure A9. Iso-response curves energy consumption for X 3= constant (-1, 0 and +1)

We can clearly see the existence of an optimum region of electrolyte type and concentration, where the energy consumed is minimal. According to the results shown in Figure A9, for an electrolyte concentration at the lower end of the study range (X_3= -1), at a current of between 0.1 and 0.2 A and a salt concentration of between 4 and 5 g/L, the EC is ~ 0.45 kWh/g O_2removed, whereas for an electrolyte concentration Na_2SO_4 of between 3 and 5 g/L, the EC is
0.06 kWh/g O_2removed, the difference is obvious.

On the other hand, for the higher concentration level (X_3= +1), the CE is minimal and is worth 0.3 kWh/g O_2removed in a NaCl concentration range between 2 and 5 g/L.

In conclusion, whatever the level of the X_1factor, the energy consumed is disproportionate to the electrolyte concentration, and the maximum electrolyte concentration is the optimum concentration.

References

[1] Goupy, J. (1999) Design of experiments for response surfaces, Technique et Ingénierie, Génie industriels series.